MMP MODELING AND OPTIMIZATION OF PHOTONIC CRYSTALS, OPTICAL DEVICES, AND NANOSTRUCTURES

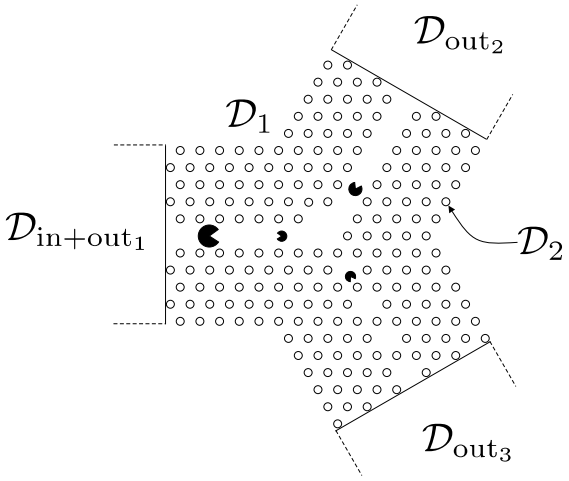

Esteban Moreno Soriano

DISS. ETH No. 14553

DISS. ETH No. 14553

MMP MODELING AND OPTIMIZATION OF PHOTONIC CRYSTALS, OPTICAL DEVICES, AND NANOSTRUCTURES

A dissertation submitted to the
SWISS FEDERAL INSTITUTE OF TECHNOLOGY
ZURICH

for the degree of
Doctor of Natural Sciences

presented by
ESTEBAN MORENO SORIANO
Lic. CC. Físicas, Universidad Complutense de Madrid
Born April 21, 1969
in Alicante (Spain)

accepted on the recommendation of
Prof. Dr. R. Vahldieck, examiner
Prof. Dr. Ch. Hafner, Dr. R. E. Kunz,
and Dr. F. J. García Vidal, coexaminers

2002

Acknowledgements

I would like to acknowledge several persons who helped me during the development of the work presented here. I warmly thank Christian Hafner (my Doktorvater) and Daniel Erni for their scientific (and not scientific) support. Christian unveiled to me the ancient secrets of the MMP method, and Daniel helped me whenever possible (and he was extraordinarily patient when I sometimes forgot to come to our weekly meeting). Thanks are also given to Rino Kunz for all his suggestions, to Francisco José García Vidal for his efforts as coexaminer, and to Rüdiger Vahldieck, head of the Field Theory Group at the IFH in the ETH. There exist "a few" other things besides electromagnetic fields, and therefore I thank Michael Paulus not only for interesting discussions but for his valuable and committed help. I would also like to thank the colleagues and friends I have met here at the Institute. I am especially indebted to those who have been closer to me: Franck Robin, with whom I have spent many beautiful days in the Alps, Andrea Orzati, who taught me how to cook brownies properly (wie beim Italianer), and Thomas Brauner (mein Kapitän). During the last three and a half years, my family could not always be very close to me in space, but they did so in other mysterious dimensions: I thank all of them, from the youngest to the eldest. Last (but first!) I thank the person who dragged me to Switzerland.

Zürich, 8/3/02

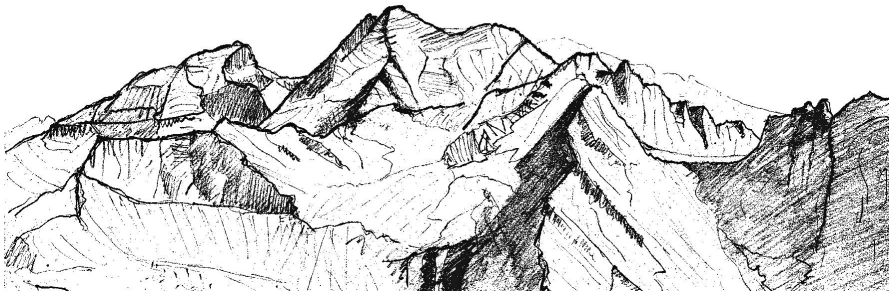

Chammliberg, Schärhorn und Chli Ruchen vom Hoch Fulen gesehen.

Contents

Acknowledgements iii

Abstract vii

Zusammenfassung ix

1 Introduction 1
- 1.1 Modeling and optimization of photonic crystals, optical devices, and nanostructures 1
- 1.2 Outline of the present work 2

2 The Multiple Multipole method 5
- 2.1 Introduction 5
- 2.2 Main concepts in two-dimensional MMP 6
  - 2.2.1 General setting 6
  - 2.2.2 Constitutive relations and domains 6
  - 2.2.3 Basis functions 6
  - 2.2.4 Boundary conditions 9
  - 2.2.5 Generalized Point Matching 10
  - 2.2.6 Error measure 11
  - 2.2.7 Further remarks 11

3 Automatic multipole setting for cylindrical structures 13
- 3.1 Introduction 13
- 3.2 Automatic multipole setting for two-dimensional problems 14
- 3.3 Computation of surface plasmons 20
  - 3.3.1 Cylinders with irregular cross section 23
  - 3.3.2 Circular cylinder near an interface 24
  - 3.3.3 Periodic grating 27
- 3.4 Waveguides and photonic crystals 29

4 Computation of eigenvalue problems 31
- 4.1 Introduction 31
- 4.2 Solution of non-linear eigenvalue problems with MMP 32
  - 4.2.1 Foundation of the method 32
  - 4.2.2 Implementation of the method in MMP 35
  - 4.2.3 Numerical issues 35
- 4.3 Band structures of metallic photonic crystals 37
  - 4.3.1 Square lattice of circular cross section cylinders 42

4.3.2 Triangular lattice of triangular cross section cylinders 47
4.4 Defects in photonic crystals 48
4.4.1 Point defect in square lattice 51
4.4.2 Line defects in square lattice 52
4.5 Propagation constants of guided modes 55

5 Modeling of photonic crystal waveguide discontinuities 59
5.1 Introduction 59
5.2 Methods for the simulation of photonic crystal waveguide discontinuities 60
5.3 Impedance matching at waveguide terminations 63
5.3.1 General principle 63
5.3.2 Computational details and assessment of the method 66
5.4 Applications 68
5.4.1 Coupling to radiative modes 68
5.4.2 Filtering T-junction 72

6 Modeling and optimization of non-periodic gratings 79
6.1 Introduction 79
6.2 Modeling of non-periodic gratings 80
6.2.1 Near field scattered by one single waveguide perturbation 80
6.2.2 Near-to-far field transformation 84
6.2.3 Far field scattered by a non-periodic grating 87
6.3 Evolutionary optimization of non-periodic gratings 91

7 Summary, conclusions, and outlook 95
7.1 Automatic Multipole Setting and surface plasmons computations 95
7.2 Computation of eigenvalue problems and photonic crystal band structures 96
7.3 Photonic crystal waveguide discontinuities 96
7.4 Modeling and optimization of non-periodic gratings 97

Bibliography 99

Abstract

The design of integrated optical devices requires accurate analysis methods in order to simulate the behavior of the electromagnetic fields in the structures under consideration. In this dissertation several numerical techniques based on the Multiple Multipole (MMP) method are presented, with an emphasis on the modeling and optimization of photonic crystals, non-periodic gratings, and metallic nanostructures.

An Automatic Multipole Setting (AMS) procedure for the two-dimensional MMP method is presented. Taking into account the global geometry of the simulated system, this AMS technique generates a distribution of multipole expansions to simulate the scattered electromagnetic fields. The technique is applied to the computation of surface modes in metallic nanostructures, metallic photonic crystals, and discontinuities in dielectric slab waveguides.

A method for the resolution of eigenvalue problems is developed, and it is applied to the computation of photonic crystal band structures and guided modes in cylindrical waveguides. A multipolar source is introduced, which excites a superposition of the modal fields. When the source frequency is tuned towards the eigenvalue frequency, the corresponding modal field resonates increasing its amplitude enormously. In this way, the eigenvalues can be found by looking for these resonances as a function of the frequency. This method can handle materials with arbitrary (frequency dependent) permittivity. Examples of band structures and modal fields of various metallic photonic crystals are presented.

The problem of the accurate characterization of photonic crystal waveguide discontinuities is addressed. To reduce the size of the simulation domain –avoiding simultaneously spurious reflections at the crystal boundaries– the field at the input and output waveguides is matched to the guided modal fields of the corresponding infinitely long waveguides. Due to the perfect impedance matching, undesired reflections do not occur and the transmission and reflection coefficients of the discontinuity can be determined. The approach is demonstrated for several photonic crystal waveguide discontinuities.

Finally, a technique for computing the far field light distribution produced in the scattering of a slab waveguide mode by a finite non-periodic grating is presented. It relies on an MMP near-field computation in conjunction with a near-to-far field transformation and a multiple scattering calculation. The method allows a fast computation of the diffracted fields and for this reason it is an appropriate forward solver for optimizations in huge search spaces. The high degree of freedom available for a non-periodic grating can be appropriately explored when such a fast forward solver is linked to an evolutionary algorithm. Using this strategy a non-periodic grating output coupler is designed.

Zusammenfassung

Der Entwurf von hochintegrierten photonischen Bauelementen verlangt zunehmend nach *präzisen Analysemethoden*, mit deren Hilfe das Verhalten des elektromagnetischen Feldes in solchen Strukturen möglichst realitätsnah simuliert werden kann. In der vorliegenden Dissertation werden verschiedene numerische Ansätze vorgestellt, die alle auf der MMP-Methode (multiple multipole method) beruhen, wobei sich die Untersuchung vor allem auf die Modellierung und Optimierung von Photonenkristallen, von nichtperiodischen Wellenleitergittern und metallischen Nanostrukturen konzentriert.

Als Erstes befasst sich die Arbeit mit der Entwicklung einer *automatisierten Polsetzungsroutine* (AMS, automatic multipole setting) für die zweidimensionale Variante von MMP. Die AMS-Routine geht dabei von einer rein geometrischen Repräsentation der Problemstellung aus und erzeugt, unter Berücksichtigung der vorgegebenen Gebietsgrenzen, eine geeignete räumliche Verteilung der Multipolentwicklungen. Diese effiziente Polsetzungstechnik berücksichtigt somit nur Apriori-Wissen, welches aus der konkreten Gestalt der Streuobjekte abgeleitet werden kann. Die Zuverlässigkeit der resultierenden Feldsimulationen wird anhand von drei anspruchsvollen Testfällen evaluiert: Die Berechnung von Oberflächenwellen in metallischen Nanostrukturen, die Simulation von Diskontinuitäten in dielektrischen Filmwellenleitern und das Problem der Eigenwertberechnung in metallischen Photonenkristallen.

Ein weiterer Schwerpunkt bilden die *Untersuchungen zur Eigenwertberechnung* komplexer optischer Randwertprobleme. Unter diesem Gesichtspunkt stehen vor allem die Bandstrukturrechnung von Photonenkristallen und die Analyse geführter Modi in zylindrischen Wellenleiterstrukturen zur Diskussion. Im Gegensatz zu früheren Implementierungen der Eigenwertsuche in MMP wird hier ein neuer Ansatz vorgeschlagen, der bewusst einen (singulären) Multipol in das Feldgebiet einbringt, was die Anregung aller zu erwartenden Eigenlösungen garantieren soll. Bei sorgfältigem Durchstimmen der Anregungsfrequenz, kann jede dieser Eigenlösungen in Resonanz gebracht werden, was sich wiederum durch eine dramatische Zunahme der zugehörigen Modenfeldamplituden bemerkbar macht. Die Eigenwertsuche gestaltet sich daher relativ einfach, indem man geeignete Projektionen dieser Amplituden definiert und nach deren Extrema im Frequenzraum sucht. Im Gegensatz zu alternativen Bandstrukturrechnungen erlaubt dieser Ansatz auch die Behandlung von hoch dispersiven Medien. Mit der Analyse metallischer Photonenkristalle und dem Hinweis auf die resultierenden Plasmonresonanzen konnte dies in überzeugender Weise gezeigt werden.

Die *Charakterisierung von Wellenleiterdiskontinuitäten in Photonenkristallen* gehört zu einem weiteren Schwerpunkt dieser Arbeit. Die enge Lichtführung,

die auf den Mechanismen der Defektwellenleitung in Photonenkristallstrukturen beruht, erweist sich vor allem im Hinblick auf alternative Bauformen von Bauelementen für hochintegrierte optische Schaltungen als äusserst attraktiv. Bedingt durch die rasch ansteigende Komplexität solcher Strukturen wurde nach Wegen gesucht, um den Simulationsraum der resultierenden Problemstellung möglichst klein zu halten. Dies gelingt nur mit Hilfe einer rechenökonomisch sinnvollen Unterteilung, indem man die Diskontinuitäten der Schaltungstopologie von den regulären Defektwellenleitern separiert betrachtet. Die Modi der regulären Defektwellenleiter ergeben sich wiederum aus der vorhergehenden Eigenwertberechnung bezüglich einer unendlich langen Wellenleiterstruktur. Dank dieser Massnahme kann die eigentliche Diskontinuität nun als Mehrtor aufgefasst werden, dessen Ein- und Ausgangstore durch das Ansetzen der berechneten Eigenlösungen reflexionsfrei abgeschlossen sind und dadurch erstmals eine verzerrungsfreie Berechnung der entsprechenden Transmissions- und Reflexionsspektren erlaubt. Die verzerrungsfreie Charakterisierung von Wellenleiterdiskontinuitäten in Photonenkristallen wurde anhand verschiedener Wellenleitertopologien validiert.

Der letzte Teil der vorliegenden Arbeit befasst sich mit der *effizienten Berechnung von Fernfeldern*, welche durch Streuprozesse an Filmwellenleiterdiskontinuitäten –wie z.B. einer nichtperiodisch angeordneten Wellenleiterstörung endlicher Länge– entstehen können. Das Nahfeld der einzelnen Wellenleiterstörung wird dabei vorgängig mit MMP berechnet und über eine Nahfeld-Fernfeld-Transformation durch den geeigneten Multipol ersetzt, dessen Amplitude wiederum über ein einfaches Streuamplitudenkalkül mit der geführten Mode des Filmwellenleiters verknüpft ist. Damit lassen sich Fernfelder von komplexen irregulären Wellenleiterstörungen auf äusserst effiziente Weise berechnen. Die Leistungsfähigkeit des vorgeschlagenen Vorwärtslösers wurde anhand der Optimierung des Abstrahlverhaltens von nichtperiodischen Wellenleitergitterstrukturen demonstriert. Die zahlreichen Freiheitsgrade, welche charakteristisch für eine derart irreguläre Struktur sind, definieren umgekehrt einen enormen Suchraum, der nur noch mit Hilfe heuristischer Suchverfahren wie z.B. evolutionären Algorithmen bearbeitet werden kann. Die Tauglichkeit des Verfahrens wurde mit dem erfolgreichen Entwurf eines nichtperiodischen Gitterkopplers unter Beweis gestellt.

Übersetzung: Daniel Erni

1
Introduction

1.1 Modeling and optimization of photonic crystals, optical devices, and nanostructures

During the last decades the size of electronic integrated circuits has been reduced in an exponential way [1]. If this tendency is to be held, major advances in lithography have to be achieved in the short run [2]. Eventually, as feature sizes shrink, a fundamental limit will be reached when the thinness of silicon oxide does not longer guarantee an adequate isolation of conducting regions [3]. These predictions –together with the higher speed and capacity of optical signals– have triggered the interest in integrated optics.

In the optical regime, following the pattern of integrated electronics, there has been recently an increasing trend towards device miniaturization. Apart from the obvious advantages of small systems, this tendency is mainly motivated by the desire of obtaining higher speeds in the processing of the optical signal [4]. Miniaturization requires a more dense integration in the optical chip. In order to increase the functionality per surface unit of chip, several strategies can be followed, such as shrinking the size of every single component, designing multifunctional elements, and reducing the length of the interconnections between the various components in the chip.

The development of smaller and/or multifunctional components poses –besides the technological difficulties– computation and design challenges. For instance, the consideration of novel non-periodic structures may allow one to design devices with a better performance, but this requires more sophisticated analysis tools. Although there exist some numerical tools for this purpose, further work is needed in order to make them more reliable, accurate, and robust. Once these simulation methods for the computation of the optical field are available, the structures must be optimized in order to satisfy given design specifications. For this reason, it is necessary to investigate a whole set of techniques bridging the gap between the modeling methods which simulate the behavior of the electromagnetic field and the optimization algorithms needed to meet the optical device's design specifications.

Compared to the design of the components on the chip, the problem of the interconnection between them seems apparently to be easier. Nevertheless, in the framework of dense optical integration, this is not a solved issue: to obtain a complex optical circuit on the chip, waveguide bends with small curvature radius have to be designed. This is not trivial because –using the language of geometrical

optics– the total internal reflection condition should be kept. The use of resonant cavities at the waveguide corners [5], and the increase of the dielectric contrast can reduce the losses at the corners, but it is difficult to suppress them completely. In fact, the size of the typical integrated optical components –containing bends, junctions, couplers, etc.– is in the order of mm or cm rather than μm due to the constraints imposed by the minimum radius of curvature of the interconnecting waveguides [4, 6].

In this framework, one of the most promising alternatives is the photonic crystal concept [7, 8]. The underlying periodic structure of a photonic crystal gives rise to the appearance of frequency ranges (*photonic band gaps*) for which the optical field cannot propagate inside the crystal. This modification of the density of states of the optical field due to the periodicity of the crystal has many applications, e.g., it can serve as a platform for integrated optics [9]. The disruption of the crystal periodicity (with the associated field localization) allows one to design various essential optical elements of very small size. Some of them have been already fabricated, for instance resonant microcavities [10], lasers [11], and couplers [12]. Currently, there is also a large effort in the study of other required components, such as all-optical switches [13]. The interconnection problem seems to be milder within the photonic crystal perspective: line defects behave as waveguides and, since the photons cannot escape through the crystal, waveguide corners with a radius of curvature in the order of one wavelength and without losses can be designed. Structures have been shown where the transmission around the corner is almost 100% [14].

As mentioned above, the design and optimization of the required components, necessitates methods for the computation of the interaction of the electromagnetic fields with the considered structures. Up to now the most widely used computational methods for the analysis of photonic crystals are the Plane Wave Expansion method (for the computation of band structures [15]) and the Finite Difference Time Domain (FDTD) method (for the modeling of complex defect structures [16]). Some photonic perfect crystal types (most remarkably metallic photonic crystals) present a quite complex field behavior, with large field enhancement and localization. Additionally, it has been observed that the behavior of the optical devices depends critically on the position, size or material constants of some parts of the structures. Therefore, very accurate analysis tools are needed for the accurate characterization of the investigated systems. In connection with this point the Multiple Multipole (MMP) method [17] is very promising (as it will be shown in this dissertation). The purpose of this work is to develop a set of computational techniques based on the MMP method in order to model and optimize photonic crystals and other kinds of optical devices and nanostructures. The work presented in this thesis is outlined briefly in the following section.

1.2 Outline of the present work

The organization of the dissertation is sketched here. After chapter 2, where the fundamentals of the Multiple Multipole method are summarized, the main research topics addressed in this work are presented in the four following chapters.

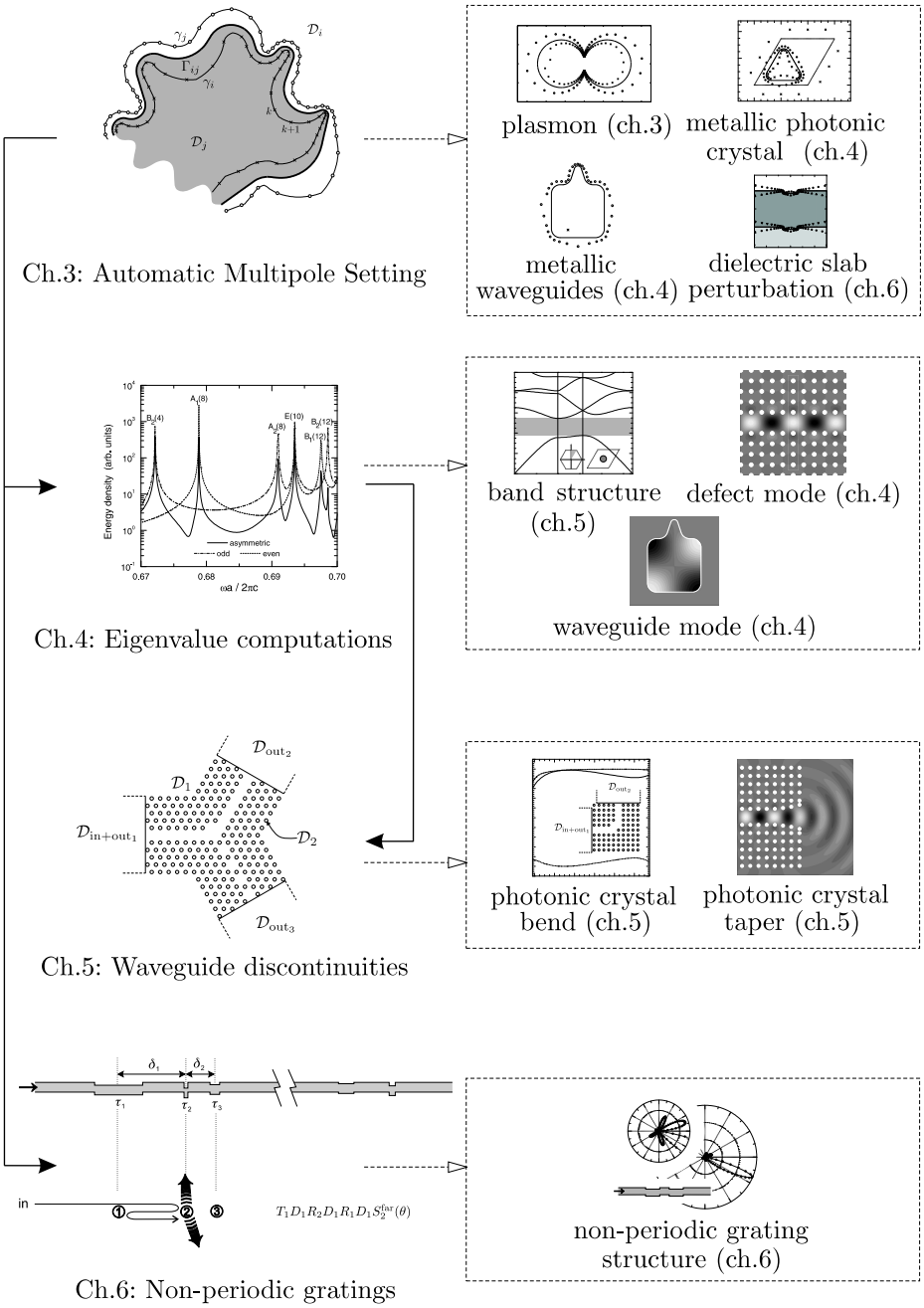

Fig. 1.1 Schematic overview of the dissertation. Left: main investigated topics, right: some of the shown applications.

This is shown graphically in Fig. 1.1, which displays on the left side the four main subjects, and on the right side some of the applications of the corresponding developed methods. The MMP modeling can be considerably simplified with the help of an **automatic multipole setting** procedure. This technique is developed in chapter 3 and it is employed for the modeling of several structures in later chapters. An **eigenvalue computation** method is proposed in chapter 4. It will be a prerequisite for the applications shown later: on the one hand it enables the calculation of photonic crystal band structures, and on the other hand it is indispensable for the analysis of guided modes. The determined guided modal fields of waveguides with continuous or discrete translational symmetry are necessary for the modeling of waveguide discontinuities, which is the subject of the next two chapters. In chapter 5 **photonic crystal waveguide discontinuities** are discussed, whereas in chapter 6, complex **non-periodic discontinuities in dielectric slab waveguides** are modeled and optimized. Finally, in chapter 7, a summary is presented, conclusions are drawn, and possible future research orientations are sketched.

2

The Multiple Multipole method

2.1 Introduction

At the beginning of the 1980s, the Multiple Multipole method (MMP) was developed in the Swiss Federal Institute of Technology by Hafner [18] and coworkers. The MMP method has its roots in Mie theory, Circular Harmonic Analysis, and Point Matching. Other groups have been working in related techniques, and all these methods –including MMP– are known as Generalized Multipole Techniques (GMT) [19, 20].

The MMP method [17, 21, 22] is a well-established numerical technique for performing electrodynamic field calculations. However, extensions to other fields –e.g., acoustics [23]– have been presented. The method is claimed to be *semi-analytical* because the computed approximations to the solution satisfy the Maxwell differential equations exactly (i.e., analytically), whereas the algebraic boundary conditions are only approximately fulfilled.

MMP is closer to analytical techniques than the domain methods –such as finite elements and finite differences– and this makes it very appropriate for studies where a high accuracy is needed. Since it is a boundary method, only the interfaces between the various materials involved have to be discretized, resulting in a lower numerical effort (especially in two-dimensional problems). Nevertheless, for the same reason, it is not well suited for systems where inhomogeneous materials are present. A main difference with other methods, and one of the strong points of MMP, is the high flexibility available for the modeling of electrodynamic problems. As it will be explained later, the basis functions employed to model the fields can be chosen with a large degree of freedom. This allows one to incorporate in the basis functions set any physical information known a priori about the solution. Thus, very accurate approximate solutions can be determined with a minimal computational effort. On the other hand, this same flexibility results in a more demanding modeling than with other known methods where the basis functions are not accessible to the user. A last major interesting feature of the MMP method is its ability of delivering a measure of the accuracy of the computed solutions. Thanks to this error estimation it is possible to avoid time-consuming convergence tests. Furthermore, since this error measure is local, the accuracy of the solution can be improved by targeting at those regions where the error is highest.

The method has been applied to various areas of electromagnetics [24]. In the field of computational optics, investigations of waveguides [25], gratings [26], and near-field microscopy [27] have been conducted among others.

The goal of this chapter is to present the essential ideas behind the MMP method. No attempt of completeness is desired, but only facilitating the reading of the following chapters. For a more detailed description see Refs. [17, 21, 22]. Since all structures investigated in this dissertation have *cylindrical* geometry [i.e., they are invariant under translations along a given axis (the Z axis)], the presentation of the MMP method will be limited here to the two-dimensional (2D) case. However, it is worth noting that this technique is not restricted to 2D problems.

2.2 Main concepts in two-dimensional MMP

2.2.1 General setting

MMP is a frequency domain technique, i.e., we are interested in solutions for which the time dependence is given by a factor $e^{-i\omega t}$, where ω is the angular frequency and t is the time. Since the structures considered in this dissertation are invariant along the Z axis, it is sufficient considering fields with a z-dependence given by the factor $e^{ik_z z}$, where k_z and z are the propagation constant and coordinate along the Z axis, respectively. Therefore, a generic scalar or vector field $\hat{\mathcal{F}}$ has the following form:

$$\hat{\mathcal{F}}(x, y, z, t) = \mathcal{F}(\mathbf{r}) e^{i(k_z z - \omega t)}, \tag{2.1}$$

where $\mathbf{r} = (x, y)$ denotes the position in the XY plane. From now on, the factor $e^{i(k_z z - \omega t)}$ will be omitted and only the fields $\mathcal{F}(\mathbf{r})$ will be considered.

2.2.2 Constitutive relations and domains

The MMP method was developed for systems with isotropic, linear, and piecewise homogeneous materials, but generalizations to anisotropic [28] and chiral [29] materials have been presented.

The 2D region where the fields are to be computed is partitioned in domains $\mathcal{D}_i$ inside which the permittivity $\varepsilon^{\mathcal{D}_i}$ and permeability $\mu^{\mathcal{D}_i}$ are $\mathbf{r}$-independent (Fig. 2.1). To allow for dispersive materials, the parameters $\varepsilon^{\mathcal{D}_i}$ and $\mu^{\mathcal{D}_i}$ are, in general, complex and ω-dependent. As it will be explained in the following subsection, the partition is defined not only to separate the regions with different ε and μ, but mainly in order to prescribe different expansions for the fields in the different domains $\mathcal{D}_i$ (see also subsection 2.2.7).

2.2.3 Basis functions

For 2D problems, the knowledge of the longitudinal components of the electric and magnetic fields $\Phi^{\mathcal{D}_i}(\mathbf{r}) = \{E_z^{\mathcal{D}_i}(\mathbf{r}), H_z^{\mathcal{D}_i}(\mathbf{r})\}$, is sufficient to derive the transverse electric $\mathbf{E}_{\mathrm{T}}^{\mathcal{D}_i}(\mathbf{r})$ and magnetic $\mathbf{H}_{\mathrm{T}}^{\mathcal{D}_i}(\mathbf{r})$ fields in $\mathcal{D}_i$ [30]:

$$\mathbf{E}_{\mathrm{T}}^{\mathcal{D}_i}(\mathbf{r}) = \frac{i}{(k_{\mathrm{T}}^{\mathcal{D}_i})^2}\left[k_z \nabla_{\mathrm{T}} E_z^{\mathcal{D}_i}(\mathbf{r}) - \omega\mu^{\mathcal{D}_i}(\mathbf{e}_z \times \nabla_{\mathrm{T}}) H_z^{\mathcal{D}_i}(\mathbf{r})\right] \tag{2.2}$$

$$\mathbf{H}_{\mathrm{T}}^{\mathcal{D}_i}(\mathbf{r}) = \frac{i}{(k_{\mathrm{T}}^{\mathcal{D}_i})^2}\left[k_z \nabla_{\mathrm{T}} H_z^{\mathcal{D}_i}(\mathbf{r}) + \omega\varepsilon^{\mathcal{D}_i}(\mathbf{e}_z \times \nabla_{\mathrm{T}}) E_z^{\mathcal{D}_i}(\mathbf{r})\right], \tag{2.3}$$

where ∇_{T} denotes the gradient in the XY plane, $\mathbf{e}_z$ is a unit vector along the Z axis, and $k_{\mathrm{T}}^{\mathcal{D}_i}$ is the transverse wave number: $\varepsilon^{\mathcal{D}_i}\mu^{\mathcal{D}_i}\omega^2 = (k^{\mathcal{D}_i})^2 = (k_{\mathrm{T}}^{\mathcal{D}_i})^2 + k_z^2$. When both elements of $\Phi^{\mathcal{D}_i}(\mathbf{r})$ satisfy the 2D Helmholtz equation in $\mathcal{D}_i$,

$$[\Delta_{\mathrm{T}} + (k_{\mathrm{T}}^{\mathcal{D}_i})^2]\Phi^{\mathcal{D}_i}(\mathbf{r}) = 0, \tag{2.4}$$

then, the fields (2.2) and (2.3) fulfill the differential Maxwell equations in $\mathcal{D}_i$. For E (resp. H) polarization only $E_z^{\mathcal{D}_i}(\mathbf{r})$ [resp. $H_z^{\mathcal{D}_i}(\mathbf{r})$] is required.

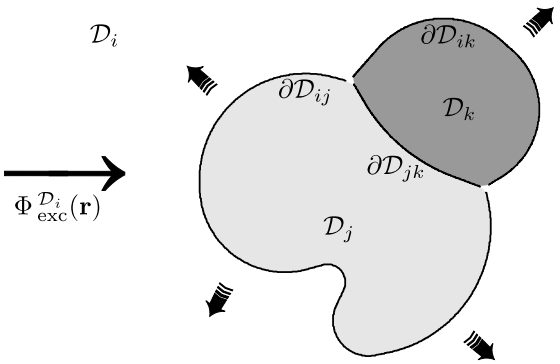

Fig. 2.1 Domains ($\mathcal{D}_i$, $\mathcal{D}_j$, and $\mathcal{D}_k$) and boundaries ($\partial\mathcal{D}_{ij}$, $\partial\mathcal{D}_{ik}$, and $\partial\mathcal{D}_{jk}$). The excitation [$\Phi_{\mathrm{exc}}^{\mathcal{D}_i}(\mathbf{r})$] and scattered fields (thick arrows) are schematically depicted as well. For clarity, the scattered fields inside domains $\mathcal{D}_j$ and $\mathcal{D}_k$ are not shown.

Within MMP, both elements of the couple $\Phi^{\mathcal{D}_i}(\mathbf{r})$ are expanded in $\mathcal{D}_i$ as a linear superposition of $N^{\mathcal{D}_i}$ known *analytical* solutions $\varphi_l^{\mathcal{D}_i}(\mathbf{r})$ of the 2D Helmholtz equation in the corresponding domain:

$$\begin{aligned}\Phi_{\mathrm{approx}}^{\mathcal{D}_i}(\mathbf{r}) &= \Phi_{\mathrm{exc}}^{\mathcal{D}_i}(\mathbf{r}) + \Phi_{\mathrm{sca,\,approx}}^{\mathcal{D}_i}(\mathbf{r}) \\ &= \Phi_{\mathrm{exc}}^{\mathcal{D}_i}(\mathbf{r}) + \sum_{l=1}^{N^{\mathcal{D}_i}} f_l^{\mathcal{D}_i}\varphi_l^{\mathcal{D}_i}(\mathbf{r}),\end{aligned} \tag{2.5}$$

where $\Phi_{\mathrm{approx}}^{\mathcal{D}_i}(\mathbf{r})$ denotes the approximation to the actual field, the terms $\Phi_{\mathrm{exc}}^{\mathcal{D}_i}(\mathbf{r})$, $\Phi_{\mathrm{sca,\,approx}}^{\mathcal{D}_i}(\mathbf{r})$ represent the exciting and approximated scattered fields, respectively, and $f_l^{\mathcal{D}_i}$ are unknown coefficients to be determined. With a series expansion like Eq. (2.5), the Maxwell differential equations are satisfied in every $\mathcal{D}_i$, thus, the only remaining conditions to be fulfilled are the boundary conditions at $\partial\mathcal{D}_{ij}$ and –for open domains– at infinity (see subsection 2.2.4). As said before, in the standard implementation $\Phi^{\mathcal{D}_i}(\mathbf{r})$ is $\{E_z^{\mathcal{D}_i}(\mathbf{r}), H_z^{\mathcal{D}_i}(\mathbf{r})\}$; however, in

general, $\Phi^{\mathcal{D}_i}(\mathbf{r})$ denotes generic potential fields that satisfy the 2D Helmholtz equation and from which $\mathbf{E}^{\mathcal{D}_i}(\mathbf{r})$ and $\mathbf{H}^{\mathcal{D}_i}(\mathbf{r})$ can be extracted by means of a linear operator.

It was mentioned above that the basis functions $\varphi_l^{\mathcal{D}_i}(\mathbf{r})$ are absolutely arbitrary as far as they are analytical solutions of the 2D Helmholtz equation. Nevertheless, as the name of the method suggests, the multipolar functions are the most frequently used basis functions. A scalar 2D multipolar function with origin in the point $\mathbf{r}_{\mathrm{O}_l}$ is given by

$$\varphi_l^{\mathcal{D}_i}(r_l, \phi_l) = H_{n_l}^{(1)}(k_{\mathrm{T}}^{\mathcal{D}_i} r_l) \cdot \begin{cases} \cos(n_l \phi_l) \\ \sin(n_l \phi_l) \end{cases}, \tag{2.6}$$

where $H_{n_l}^{(1)}(\cdot)$ is the Hankel function of first kind and order n_l, and (r_l, ϕ_l) are polar coordinates with origin in $\mathbf{r}_{\mathrm{O}_l}$.

Usually, several "clusters" of multipolar functions are employed to expand the fields. Each cluster is a set of multipolar functions, all of them located at the same point and including several multipolar orders. The term *multipole expansion* of order n refers to such a cluster with orders n_l ranging from zero up to n [a *Bessel expansion* is the same but replacing the Hankel functions with Bessel functions $J_{n_l}(\cdot)$].

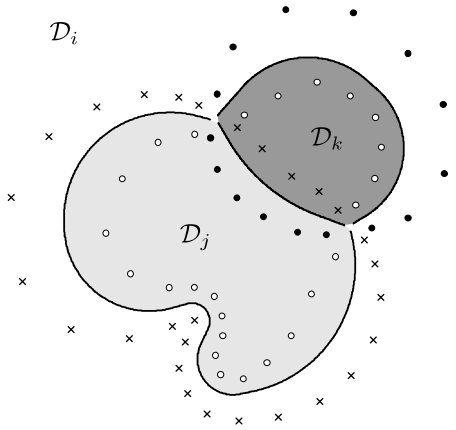

Fig. 2.2 Multipole expansions distribution. The ∘'s, ×'s, and •'s denote the origins of multipole expansions modeling the fields in domains $\mathcal{D}_i$, $\mathcal{D}_j$, and $\mathcal{D}_k$, respectively.

Vekua theory [31] guarantees that for a multiply connected finite domain $\mathcal{D}_i$ one Bessel expansion and additionally one multipole expansion in each hole of $\mathcal{D}_i$ is a complete basis (for an infinite domain the Bessel expansion is not required). Nevertheless, when the interfaces $\partial\mathcal{D}_{ij}$ of the domains (Fig. 2.1) deviate from the circular shape, several multipole expansions located at different positions achieve a much better convergence of the expansion in Eq. (2.5). Since a multipolar function is singular in its origin, the multipole expansions are placed outside $\mathcal{D}_i$ to expand fields that are regular in $\mathcal{D}_i$ (Fig. 2.2). The appropriate positioning of the multipole expansions will be described in detail later.

2.2.4 Boundary conditions

As mentioned, using an expansion like Eq. (2.5), the Maxwell differential equations are analytically satisfied in every domain. To determine the unknown coefficients $f_l^{\mathcal{D}_i}$, the following *weighted* boundary conditions are imposed on a set of collocation points (or *matching* points) $\mathbf{r}_k$, $k = 1, \ldots, N_{\text{col}}$ along the interfaces $\partial\mathcal{D}_{ij}$ (Fig. 2.3):

$$\left.\begin{aligned} w_{\mathrm{E}_\parallel}(\mathbf{r}_k)[\mathbf{E}_\parallel^{\mathcal{D}_i}(\mathbf{r}_k) - \mathbf{E}_\parallel^{\mathcal{D}_j}(\mathbf{r}_k)] &= \mathbf{0} \\ w_{\mathrm{E}_\perp}(\mathbf{r}_k)[\varepsilon^{\mathcal{D}_i} E_\perp^{\mathcal{D}_i}(\mathbf{r}_k) - \varepsilon^{\mathcal{D}_j} E_\perp^{\mathcal{D}_j}(\mathbf{r}_k)] &= 0 \\ w_{\mathrm{H}_\parallel}(\mathbf{r}_k)[\mathbf{H}_\parallel^{\mathcal{D}_i}(\mathbf{r}_k) - \mathbf{H}_\parallel^{\mathcal{D}_j}(\mathbf{r}_k)] &= \mathbf{0} \\ w_{\mathrm{H}_\perp}(\mathbf{r}_k)[\mu^{\mathcal{D}_i} H_\perp^{\mathcal{D}_i}(\mathbf{r}_k) - \mu^{\mathcal{D}_j} H_\perp^{\mathcal{D}_j}(\mathbf{r}_k)] &= 0 \end{aligned}\right\}, \tag{2.7}$$

where $\parallel$ and $\perp$ stand for parallel and perpendicular to the interface, respectively, and $w_{..}(\mathbf{r}_k)$ are appropriately selected weighting factors defined in the following subsection.

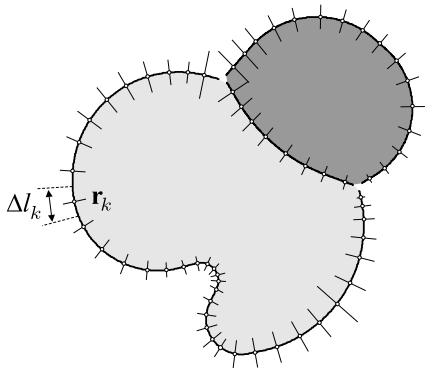

Fig. 2.3 Collocation points $\mathbf{r}_k$ ($\circ$'s). The segments perpendicular to the boundary at each collocation point represent the mismatching of the fields at that point.

It is known that the tangential and normal boundary conditions are not all independent [32]. To be more precise: if (*i*) The boundary conditions for the tangential components of the fields are satisfied exactly everywhere on the boundary $\partial\mathcal{D}_{ij}$, and (*ii*) The Maxwell equations are fulfilled in $\mathcal{D}_i$ and $\mathcal{D}_j$, then the boundary conditions for the normal components of the fields are satisfied automatically. Nevertheless, when dealing with approximate solutions which do not fulfill (*i*) exactly, it is better to employ all boundary conditions to guarantee that all components of the field satisfy the boundary conditions with a similar accuracy. Therefore the system of Eq. (2.7) comprises $6N_{\text{col}}$ equations in general or $5N_{\text{col}}$ for E or H polarization.

The functions in Eq. (2.6) satisfy the Sommerfeld radiation conditions [33] and therefore no special care is needed with this issue if they are used to represent the scattered field in open domains.

2.2.5 Generalized Point Matching

System (2.7) together with expansion (2.5) leads to a matrix equation of the type

$$\sum_{\beta} A_{\alpha\beta} F_{\beta} = G_{\alpha}, \tag{2.8}$$

where $A_{\alpha\beta}$ is a rectangular matrix, the vector F_{β} includes the unknowns $f_{l}^{\mathcal{D}_i}$ and the vector G_{α} stems from the excitation. The technique works with more equations than unknowns leading to an *overdetermined* system. Equation (2.8) is solved in the least squares sense, i.e., the residual $R = \|AF - G\|_2$ is minimized ($\|\cdot\|_2$ denotes the usual vector norm). The standard procedure used by MMP to solve Eq. (2.8) is the Givens algorithm based on plane rotations [34].

The residual R to be minimized is the sum of local residuals at the collocation points:

$$\begin{aligned} R = \sum_{k=1}^{N_{\mathrm{col}}} \Big\{ & |w_{\mathrm{E}_\parallel}(\mathbf{r}_k)|^2 \, [\mathbf{E}_\parallel^{\mathcal{D}_i}(\mathbf{r}_k) - \mathbf{E}_\parallel^{\mathcal{D}_j}(\mathbf{r}_k)] \cdot [\mathbf{E}_\parallel^{\mathcal{D}_i}(\mathbf{r}_k) - \mathbf{E}_\parallel^{\mathcal{D}_j}(\mathbf{r}_k)]^* \\ & + |w_{\mathrm{E}_\perp}(\mathbf{r}_k)|^2 \, |\varepsilon^{\mathcal{D}_i} E_\perp^{\mathcal{D}_i}(\mathbf{r}_k) - \varepsilon^{\mathcal{D}_j} E_\perp^{\mathcal{D}_j}(\mathbf{r}_k)|^2 \\ & + |w_{\mathrm{H}_\parallel}(\mathbf{r}_k)|^2 \, [\mathbf{H}_\parallel^{\mathcal{D}_i}(\mathbf{r}_k) - \mathbf{H}_\parallel^{\mathcal{D}_j}(\mathbf{r}_k)] \cdot [\mathbf{H}_\parallel^{\mathcal{D}_i}(\mathbf{r}_k) - \mathbf{H}_\parallel^{\mathcal{D}_j}(\mathbf{r}_k)]^* \\ & + |w_{\mathrm{H}_\perp}(\mathbf{r}_k)|^2 \, |\mu^{\mathcal{D}_i} H_\perp^{\mathcal{D}_i}(\mathbf{r}_k) - \mu^{\mathcal{D}_j} H_\perp^{\mathcal{D}_j}(\mathbf{r}_k)|^2 \Big\}, \end{aligned} \tag{2.9}$$

where the star * denotes complex conjugate. The weights $w_{\cdot\cdot}(\mathbf{r}_k)$ in Eq. (2.9) are defined in the following way:

$$w_{\mathrm{E}_\parallel}(\mathbf{r}_k) = (\Delta l_k)^{\frac{1}{2}} \; ; \; w_{\mathrm{E}_\perp}(\mathbf{r}_k) = \Big(\frac{1}{\varepsilon^{\mathcal{D}_i}\varepsilon^{\mathcal{D}_j}}\Big)^{\frac{1}{2}} (\Delta l_k)^{\frac{1}{2}} \tag{2.10}$$

$$w_{\mathrm{H}_\parallel}(\mathbf{r}_k) = \Big(\frac{\mu^{\mathcal{D}_i}\mu^{\mathcal{D}_j}}{\varepsilon^{\mathcal{D}_i}\varepsilon^{\mathcal{D}_j}}\Big)^{\frac{1}{4}} (\Delta l_k)^{\frac{1}{2}} \; ; \; w_{\mathrm{H}_\perp}(\mathbf{r}_k) = \Big(\frac{1}{\varepsilon^{\mathcal{D}_i}\varepsilon^{\mathcal{D}_j}\mu^{\mathcal{D}_i}\mu^{\mathcal{D}_j}}\Big)^{\frac{1}{4}} (\Delta l_k)^{\frac{1}{2}}. \tag{2.11}$$

Every weight consists of two factors: a factor depending on the parameters ε and μ, and a geometrical factor. The first factor is required for dimensional consistency [with it, all terms in the sum of Eq. (2.9) obtain the dimensions of square electric field times length]. Moreover, without it the various terms in this sum may be of very different orders of magnitude, thus, a given non-weighted boundary condition in Eq. (2.7) could have much less influence than the others in the residual calculation. The second factor is related to the geometrical distribution of collocation points along the interface. The boundary $\partial\mathcal{D}_{ij}$ is partitioned in segments of length Δl_k and the collocation point $\mathbf{r}_k$ is set at the middle of the k-th segment (Fig. 2.3). With these geometrical factors, Eq. (2.9) is equivalent to the *integral of the residual* along the boundary evaluated numerically. Since Δl_k are not necessarily equal, this weighting ensures an appropriate balance of the influence of the various collocation points in the sum of Eq. (2.9). Eventually,

the weights can be affected by a third factor. This "user defined" factor may be employed, e.g., to enforce the boundary conditions in given collocation points more strongly than in others.

The extension of the simple collocation method described in this subsection is known as Generalized Point Matching.

2.2.6 Error measure

Since the matrix Eq. (2.8) is overdetermined, in general the approximate solution cannot satisfy exactly the weighted boundary conditions at the collocation points. As mentioned, they are fulfilled in the least squares sense. The overdetermination of the system has three important consequences: (*i*) The exact positioning of the collocation points is not critical. (*ii*) The local residuals along $\partial\mathcal{D}_{ij}$ are more balanced. Without overdetermination the local residuals in the matching points would be zero, but they would be unknown (and possibly large) between the matching points. (*iii*) The fields *mismatchings* at the collocation points can be computed. The fields mismatchings at the k-th collocation point are the k-th terms in the sum (2.9) but with weights $w_{\cdot\cdot}(\mathbf{r}_k) = 1$. Thus, the mismatchings represent the inaccuracy in the fulfillment of the non-weighted boundary conditions in $\mathbf{r}_k$. This is the error measure mentioned in section 2.1.

While solving a problem with MMP, the unknown coefficients $f_l^{\mathcal{D}_i}$ are determined, and then the fields mismatching (absolute or relative to the values of the fields in the collocation points) are plotted along the interfaces $\partial\mathcal{D}_{ij}$ (Fig. 2.3). This allows one to redefine the basis functions $\varphi_l^{\mathcal{D}_i}(\mathbf{r})$ for a next and more accurate computation. In this way the solution can be *locally* improved in those regions where the error is largest.

2.2.7 Further remarks

From the previous subsections it is clear that three essential tasks have to be accomplished in order to set up a MMP model: the selection of interfaces $\partial\mathcal{D}_{ij}$, basis functions $\varphi_l^{\mathcal{D}_i}(\mathbf{r})$, and collocation points $\mathbf{r}_k$. In this subsection some remarks are said about these three points. The additional topic of *connections* is also introduced.

Boundaries

The choice of the interfaces that define the domains is often straightforward: they are just the interfaces of the modeled objects. Occasionally *fictitious boundaries* (across which the material parameters ε and μ do not change) are introduced in order to underpin a characteristic partitioning of the underlying problem, e.g., for convergence purposes [35]. Examples of fictitious boundaries will be shown throughout this dissertation.

Basis functions

Modeling an electrodynamic problem with multipolar sources is physically intuitive: the radiation falling upon an interface $\partial\mathcal{D}_{ij}$ between two different media experiences a scattering process in which energy is re-radiated towards both media. If the multipolar sources are set right at the boundary, convergence prob-

lems arise, and therefore the sources are shifted outside the domain towards which they radiate. For instance, the radiation towards domain $\mathcal{D}_i$ (Fig. 2.2) is modeled by a set of multipolar sources inside adjacent domains $\mathcal{D}_j$ and $\mathcal{D}_k$ (they are often located close to the interface). The idea resembles the classic method of images with multipolar functions acting as "images" of the incident fields. For complex problems, where many multipolar functions have to be employed, the choice of the origins of the multipole expansions is a difficult task. In chapter 3 a procedure for the Automatic Multipole Setting will be presented.

Collocation points

Once $\partial\mathcal{D}_{ij}$ and $\varphi_l^{\mathcal{D}_i}(\mathbf{r})$ have been chosen, the selection of the collocation points $\mathbf{r}_k$ is done taking into account the following considerations. The collocation points distribution induces a discretization of the boundaries. A multipolar function evaluated along the boundaries is an oscillating function. For the construction of the matrix Eq. (2.8) only the values of this function at the collocation points play a role. Therefore, the discretization of the boundaries should be fine enough to appropriately sample this oscillating function, namely, the collocation points are chosen in a way that guarantees a sufficiently fine sampling of the highest multipolar orders of every multipole expansion [36, 37]. Thus, there is an important relationship between the locations of the multipolar sources and the positions of the collocation points.

Connections

A connection is a linear superposition of basis functions with given (i.e., *fixed*) coefficients $a_l^{\mathcal{D}_i}$, $b_m^{\mathcal{D}_j}$:

$$\Phi(\mathbf{r}) = \sum_l a_l^{\mathcal{D}_i} \varphi_l^{\mathcal{D}_i}(\mathbf{r}) + \sum_m b_m^{\mathcal{D}_j} \varphi_m^{\mathcal{D}_j}(\mathbf{r}). \tag{2.12}$$

This function can be used as basis function for the modeling of a certain problem. In that case, it is handled as a "package". This means that only the global amplitude of the function is determined, while the "internal" amplitudes $a_l^{\mathcal{D}_i}$, $b_m^{\mathcal{D}_j}$ remain fixed.

The usefulness of connections can be best appreciated with an example. Let us consider that a certain electrodynamic problem has been solved with MMP, i.e., the coefficients $a_l^{\mathcal{D}_i}$, $b_m^{\mathcal{D}_j}$ have been determined. The obtained solution can be later used as a part of the modeling of a new system. For instance, the new problem can be a perturbation of the original one. It is reasonable to model the perturbed problem with a set of basis functions which contains the solution of the unperturbed one (i.e., the connection) and additional basis functions that model the deviations from the unperturbed fields. There are many other applications of the connection concept. Some of them will be shown later in this dissertation.

3

Automatic multipole setting for cylindrical structures

3.1 Introduction

The MMP method belongs to a group of techniques which are collectively known as Generalized Multipole Techniques (GMT) [19]. The GMT expand the fields as a linear superposition of basis functions. A peculiarity of the GMT is the high degree of freedom in the selection of those functions, in particular the multipolar functions. This feature allows one to achieve a very high accuracy but it makes the modeling more difficult. More specifically, the positioning of the multipolar functions origins is not an easy task and, for this reason, it has been attempted to develop procedures to locate the multipoles (or *auxiliary sources*) in a systematic way. For instance, some semi-heuristic rules were presented for the MMP method [38], the Method of Auxiliary Sources [39], the Multifilament Current model [40, 41], and for a particular kind of the MMP method that employs only 2D-monopoles [42]. Based on this type of rules several algorithms for the automatic positioning of the auxiliary sources were proposed: Leuchtmann [43, 44] presented strategies for 2D electrostatics, Regli [45] and Tudziers [46] produced methods for 3D electrodynamics, and Hafner [47] outlined a semiautomatic procedure for 2D electrodynamics. Lacking an established name, this kind of algorithms will be called *Automatic Multipole Setting* (AMS) techniques. None of the mentioned algorithms is at the same time fast, robust, and suited for complex geometries. In this chapter, a very fast AMS procedure especially devised for 2D electrodynamics and suitable for quite general geometries is presented. This algorithm simplifies enormously the MMP modeling of systems with complex boundaries.

The AMS procedure is applied to the computation of surface plasmons in metallic particles. The strong resonant fields occurring in this type of configuration require a very accurate computational technique. The investigated geometries include isolated irregular cylinders, cylinders on top of a substrate and periodic gratings.

In section 3.2 the proposed AMS technique is presented. Several applications of this AMS technique regarding surface plasmons are shown in section 3.3.

3.2 Automatic multipole setting for two-dimensional problems

The selection of the basis functions is considered to be the most difficult task in the MMP method. A completely automatic selection of the basis functions is neither possible nor desired by skilled modelers. In fact, the possibility of choosing arbitrary basis functions is one of the fundamentals of the GMT, and reflects the user's knowledge of the problem's underlying physics. Nevertheless, multipole expansions are employed in the modeling of any given problem and their properties can be exploited to define a suitable multipole arrangement with a certain degree of automation.

The choice of the position, number, and multipolar order of the sources depends on the complexity of the problem, where an important role is played by the exciting electromagnetic field, the geometry of the interfaces and the material constants ε, μ. This choice of the multipolar sources has to be made in such a way that the boundary conditions for the fields at both sides of the interface can be accurately satisfied. This means that the radial and angular dependencies of the chosen multipolar functions have to be able to capture all the complexity of the actual field.

The use of multiple multipole expansions with different origins gives a high flexibility and helps to model complex fields. However, this flexibility has to be handled with caution. When multipole expansions of infinite order are considered, the addition theorem allows one to show that expansions with different origins are not independent [48]. Since MMP employs expansions of finite order, two multipoles displaced with respect to each other are not strictly dependent. However, when two multipole expansions are located close to each other in comparison with the distance to the boundary where the boundary conditions are imposed, the expansions become dependent from a numerical point of view. When imposing the boundary conditions to such a series expansion, ill-conditioned matrix equations may be generated which produce useless results if they are not properly managed [17, 34]. The mathematical properties of the multipolar functions help to mitigate this inconvenience: these functions decay rapidly with distance from the source origin and, therefore, multipole expansions distant from each other are effectively independent. On the other hand, multipole expansions that are close to each other may cause numerical problems.

The technique presented in this section determines the positions of the multipole expansions in such a way that numerical dependencies are avoided. This procedure finds a compromise between sparse multipole distributions where multipoles are numerically independent but not accurate enough and dense multipole distributions which permit high accuracy at the cost of ill-conditioned matrices.

The principles on which a new AMS procedure valid for cylindrical structures (2D electrodynamics) is based, are now described. A motivation of the kind of information that is used as input for the method is presented first. As mentioned above, the location of the multipole expansions should in principle depend on: (*i*) the exciting field $\Phi_{\mathrm{exc}}^{\mathcal{D}_i}(\mathbf{r})$ [for the sake of simplicity in this description, we consider that the exciting field $\Phi_{\mathrm{exc}}(\mathbf{r})$ is acting only in one domain $\mathcal{D}_i$], (*ii*) the geometry of the domains (which in the 2D case is given by the interface curve

$\Gamma_{ij} \equiv \partial\mathcal{D}_{ij}$), and (*iii*) their material properties $\varepsilon^{\mathcal{D}_i}$, $\mu^{\mathcal{D}_i}$, $\varepsilon^{\mathcal{D}_j}$, $\mu^{\mathcal{D}_j}$. Some authors [49, 50] working with GMT do indeed use the information about $\Phi^{\mathcal{D}_i}_{\text{exc}}(\mathbf{r})$ to find the position of the sources. They compute the analytical continuation of the exciting field in the domain $\mathcal{D}_j$ (the so called *non-physical* domain). This analytical continuation has singularities inside $\mathcal{D}_j$, which are the optimal locations for the auxiliary sources. In practical situations, with an irregular interface Γ_{ij} and arbitrary excitation, finding the singularities would require a large computational effort in itself. Therefore, here only the geometry of the boundary Γ_{ij} (together with the wavelengths $\lambda^{\mathcal{D}_i}$, $\lambda^{\mathcal{D}_j}$ of the fields in $\mathcal{D}_i$ and $\mathcal{D}_j$) is used as input information for the proposed AMS method. Experience has shown that these are usually the most relevant factors. By using only this input information a very fast AMS algorithm has been developed. Another motivation for this decision is that this AMS technique has been designed to be applied in structural optimization of integrated optical devices. For these optimizations many field computations have to be performed while changing only the geometry of the device.

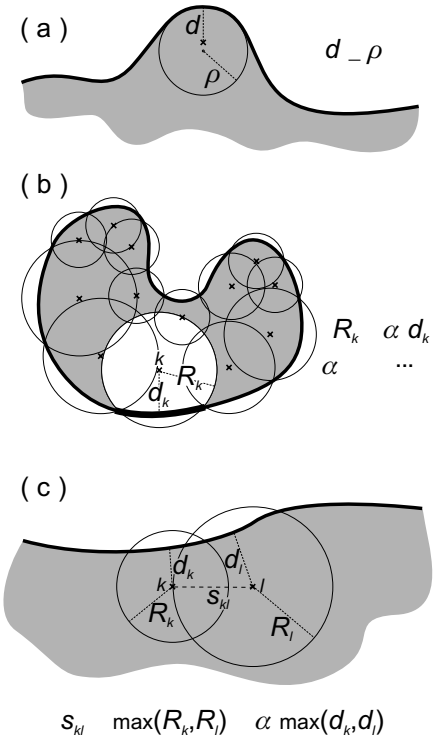

Fig. 3.1 Rules for positioning the multipoles (×'s). For an explanation of the rules see section 3.2. (a) Rule 1 (ρ is the local radius of curvature and d is the minimum distance multipole-boundary), (b) Rule 2; the area of maximum influence of multipole k is shown as well (non shaded circle of radius R_k), (c) Rule 3.

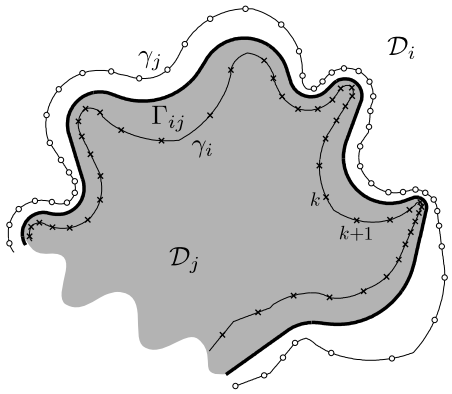

Fig. 3.2 Automatic Multipole Setting: The multipoles (×'s) for the outer domain $\mathcal{D}_i$ are located on the inner auxiliary curve γ_i. This curve is constructed using the local radius of curvature of Γ_{ij}. The distance between two consecutive multipoles k and $k+1$ is determined using rule 3.

The method is based on three ideas. First, it is expected that the complexity of the fields is higher where the interface presents a complex geometry. This is so because near these areas, the field may be focused, guided or may reach a resonant regime. Therefore these areas where the field is potentially complex need a dense distribution of multipole expansions in order to represent the field adequately. Second, a large total number of multipole expansions is computationally expensive, and hence this number should be kept to a minimum. In consequence, the density of multipoles should be low in those regions where the field is expected to be regular. Taking into account these two points, it is proposed a distribution of multipole expansions adapted to the field complexity which, in turn, has to be extracted from the geometry of the interface curve Γ_{ij}. The third point is that, in any case, the multipole expansions have to be located avoiding numerical dependencies among them. This precludes the problem of ill-conditioned matrices explained before.

These ideas are implemented by following certain simple semi-heuristic rules. Some of these rules are expressed in terms of the concept of *area of maximum influence* [51] of a multipole expansion, which is recalled here. The area of maximum influence of a multipole expansion is (in 2D) a circle of radius R centered at the source [Fig. 3.1(b)]. This source "illuminates" the nearest part of the boundary. Therefore, when imposing the boundary conditions [Eq. (2.7)], each multipole expansion has a maximum influence on the collocation points contained in a certain segment of Γ_{ij}, and it has almost no influence on the collocation points in those parts of the boundary lying far away from it and closer to other multipole expansions. Typically $R = \alpha\, d$, where d is the minimum distance from the source to the boundary, and $\alpha \approx 1.2 \cdots 1.4$ [52]. With this concept the following rules can be enunciated.

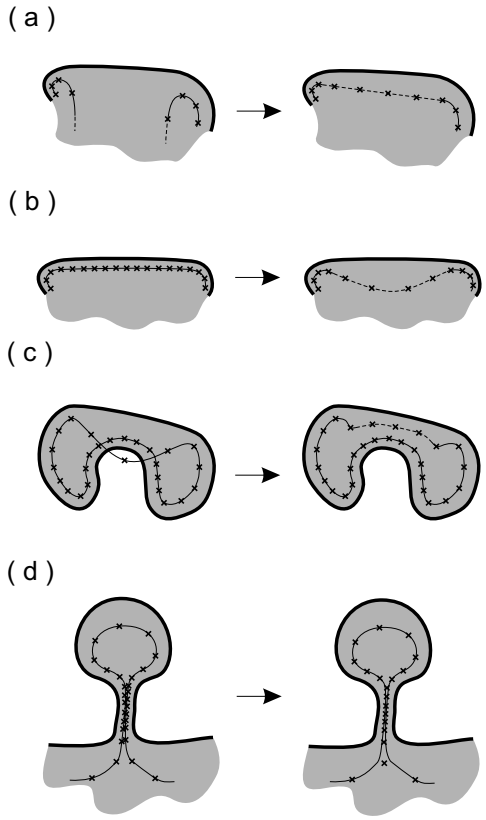

Fig. 3.3 Refinements of the basic procedure for the Automatic Multipole Setting. The thin lines depict the auxiliary curves γ_i. The left column represents the distribution of multipoles generated with the basic procedure without refinements and the right column with the corresponding refinements.

To ensure that the multipole expansions distribution is able to model the complexities of the field two rules are stated:

> **Rule 1:** Let a multipole expansion be located in the concave side of a part of Γ_{ij}. The distance d from the multipole expansion to the boundary must be $d \leq \rho$, where ρ is the local radius of curvature of Γ_{ij} [Fig. 3.1(a)].
>
> **Rule 2:** Every part of the boundary Γ_{ij} has to be inside the area of maximum influence of some multipole expansion [51] [Fig. 3.1(b)].

Rule 1 helps –together with rule 2– to obtain a denser distribution of multipoles where the curvature is high. This rule is also related to a guideline [53] used in the Method of Auxiliary Sources. The same argument employed in Ref. [53] can be applied to justify rule 1. The content of rule 2 is clear: it avoids the boundary conditions not being accurately fulfilled in any part of the interface. The next rule avoids numerical dependencies among multipole expansions:

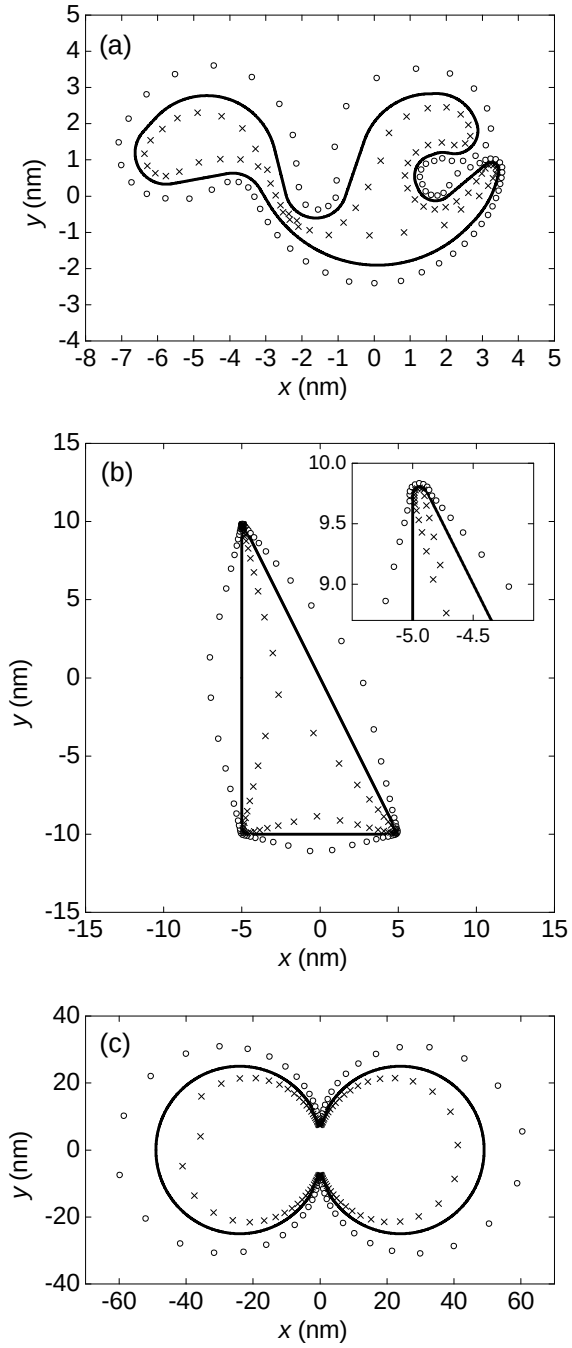

Fig. 3.4 Distributions of multipoles generated with the Automatic Multipole Setting method: (a) Generic domain shape; note that the procedure takes into account the *global* topology of the domains, (b) Triangular cross section cylinder (see subsection 3.3.1); the corners of the triangle were rounded as in reference [54], (c) Fused cylinders (see subsection 3.3.1); the radii of the circumferences are $r = 25\,\mathrm{nm}$ and the distance between the centers is $l = 48\,\mathrm{nm}$. The cusps were rounded with a radius $r_\mathrm{c} = 0.25\,\mathrm{nm}$.

Rule 3: Let there be two multipole expansions whose minimum distances to the boundary are d_k, d_l and whose radii of maximum influence are R_k, R_l, respectively. If their areas of maximum influence overlap on the boundary, the distance $s_{k\,l}$ between the multipoles must be $s_{k\,l} \geq \max(R_k, R_l) = \alpha \max(d_k, d_l)$ [55] [Fig. 3.1(c)].

The considerations that led to rule 3 [56] necessitate that the distances from the multipoles to the boundary are always smaller than the wavelength in the domain where they act. A last obvious rule is:

Rule 4: A multipole expansion acting in domain $\mathcal{D}_i$ has to be located outside this domain [57].

Without describing in full detail the AMS algorithm, now an appropriate way to incorporate the previous three ideas and rules is presented. Figure 3.2 shows how, given an interface curve Γ_{ij}, the locations of the multipole expansions for domain $\mathcal{D}_i$ are defined. First, an auxiliary curve γ_i outside $\mathcal{D}_i$ (see rule 4) and running "parallel" to Γ_{ij} is constructed and then, starting from one end of γ_i, multipolar sources are laid along it. Two consecutive multipoles $(k,\ k{+}1)$ may be neither too close (see rule 3) nor too far (see rule 2) from each other. To enforce rule 1, and to minimize the total number of multipole expansions, we construct the auxiliary curve γ_i by defining the distance $d_{\Gamma-\gamma}$ between Γ_{ij} and γ_i as a fraction of the local radius of curvature ρ of the interface (but attending to the condition $d_{\Gamma-\gamma} < \lambda^{\mathcal{D}_i}$), i.e., $d_{\Gamma-\gamma} = \min(\beta\,\rho,\ \eta\,\lambda^{\mathcal{D}_i})$, with $\beta, \eta \in (0, 1)$. In this manner, the curve γ_i runs very close to the interface where the radius of curvature is small and recedes farther away where the radius of curvature is large. With such a curve γ_i and by using rule 2, and rule 3 to distribute the multipole expansions, a tight distribution of multipoles is defined near the irregularities of the boundary, whereas a less dense and farther located multipole distribution arises where the interface is flatter. Values that proved to be adequate are $\beta \approx 0.25$[1], $\eta \approx 0.5$ and $s_{k\,k+1} = \max(R_k, R_{k+1}) = \alpha \max(d_k, d_{k+1})$, i.e., consecutive multipoles are located as close as rule 3 permits.

Note that the construction of γ_i depends only on the local radius of curvature of the interface. Hence, it can be said that γ_i is constructed with a *local* algorithm. To be useful for a large number of geometries, the construction of the "parallel" curve γ_i has to be refined with a set of modifications to cope with some problems. For example, when the boundary has a straight segment, the radius of curvature becomes infinite and the construction of γ_i fails [Fig. 3.3(a)]. To avoid this problem, for a flat section of Γ_{ij}, the curve γ_i is constructed by interpolation from the previous and next sections of γ_i. A different problem occurs when the flat section is long in comparison with the radius of curvature of the previous and following sections: the interpolation produces an unnecessarily large number of multipole expansions [Fig. 3.3(b)]. To avoid this, a special kind of interpolation in which γ_i recedes from Γ_{ij} near the middle of the flat segment is used. With these modifications, the construction of the curve γ_i is not *local* anymore,

[1] In the convex side of Γ_{ij} a correspondingly larger value of β is used to obtain a similar number of multipoles at both sides of the interface.

because it uses information about extended parts of Γ_{ij} to define the distance between both curves. But it does not take into account the *global* topology of the interface. Other refinements have been incorporated to make the method truly global. The effect of two of them is described in the Figs. 3.3(c, d). For domains with necks, it may happen that a multipole is located outside the allowed region (against rule 4) [Fig. 3.3(c)]. This problem is avoided by deforming the curve γ_i appropriately. As shown in Fig. 3.3(d) it may also occur that multipoles come too close to each other (against rule 3). This is prevented by detecting and substituting them by one single multipole. The implementation includes several such refinements and works satisfyingly for quite arbitrary geometries. It has free parameters (such as α, β and η) that can be tuned in specific cases to produce multipole distributions with a higher or lower density. The algorithm has been embedded in MaX-1 [58] which contains the latest implementation of the MMP method. Examples of the resulting multipole distributions obtained with this algorithm are presented in Figs. 3.4(a, b, c).

The presented method computes the position of the multipole expansions. The maximum multipolar order can be the same for all multipole expansions, or it can be variable. In principle, since the procedure produces denser distributions of multipoles close to the irregularities of the boundary, a fixed number of multipolar orders is appropriate. When a high accuracy is required at corners of the boundary, a scheme that proved to give good results is to correlate the maximum order of each multipolar expansion with the inverse of the distance source-interface, in such a way that sources close to the interface have higher multipolar order.

It can be asked if the multipole distributions generated with this AMS algorithm are optimal or not, although it is not completely clear what does 'optimal' mean in the context of AMS. Theoretically it would be possible to find more economical distributions of multipoles producing equal or more accurate results, but in practice this requires a tremendous effort in most cases. The main advantage of the method is that, in complex problems where several hundreds of multipole expansions are used, it simplifies enormously the modeling. For optimization problems an AMS algorithm is mandatory: here many electrodynamic calculations have to be performed and setting the multipoles by hand is not possible (see also section 4.5).

3.3 Computation of surface plasmons

Studying the interaction of light with nano-sized structures is important both theoretically and from a technological point of view. In particular, metallic nanostructured objects show a very interesting behavior: an electromagnetic field may excite collective oscillations of the object's free electrons and, for a certain frequency range of the exciting field, a complex resonant behavior can occur with strong near-field enhancement and localization. This resonant phenomenon is governed by the dielectric function $\varepsilon(\omega)$ of the metallic object and by its geometry [59–61]. For example, spherical particles small in comparison with the exciting wavelength exhibit a main resonance for $\Re[\varepsilon(\omega)] = -2\varepsilon^{\text{background}}$ [where $\Re(\cdot)$ denotes real part and $\varepsilon^{\text{background}}$ is the permittivity of the underlying medium]. At

the resonance, the fields are quite localized at the surface and they are therefore known as *surface modes* or *surface plasmons*[2].

Due to their field distribution surface plasmons are very sensitive to surface properties, and for that reason they have been investigated in relation to optical sensing [62,63]. The large fields occurring at the surface make them interesting for Surface Enhanced Raman Scattering (SERS) [64]. Plasmon coupling along a chain of particles has been proposed for guiding energy in the subwavelength scale [65–68], and primitive routing devices [69, 70] have been considered in this context as well. The field-confinement properties of metallic media have stimulated studies concerning surface plasmon propagation in nanowires [71–74], and Scanning Near-Field Optical Microscopy (SNOM) [27, 75–78]. Extraordinary optical transmission through thin metallic films patterned with a subwavelength periodic array of holes [79, 80] has been attributed to the coupling of plasmons at both sides of the film. Other applications include surface plasmon microscopy [81, 82] and polarizing optical filters [83, 84].

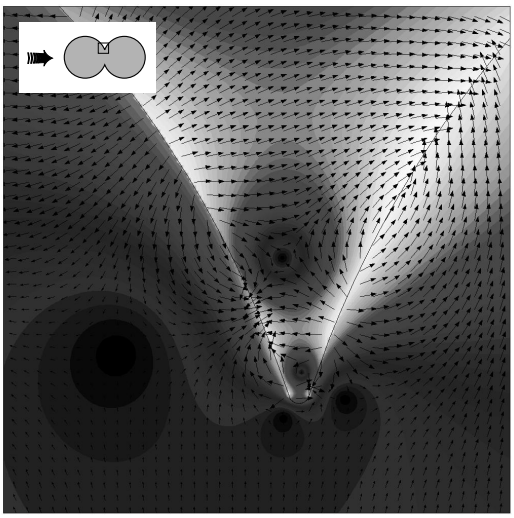

Fig. 3.5 Detail of the electric field distribution around the upper cusp (see inset). Black corresponds to zero field whereas white corresponds to maximum field. The lateral size of the figure is 12 nm. A complex field pattern can be observed which justifies a dense distribution of multipoles near the cusps (see Fig. 3.4).

Excluding those cases in which the electrostatic approximation [85] can be made, the computation of the resonances' spectrum requires the consideration of retardation effects and hence the resolution of the full vectorial Maxwell's equations is needed. Analytical solutions are available only for very simple ge-

[2]The name 'plasmon' (with the same ending as the quanta of various fields) should not lead to believe that the theory behind these computations is quantum mechanical. The whole treatment is classical (Maxwell's equations, indeed) and the only relevant quantum physics is hidden in the dielectric function $\varepsilon(\omega)$ which is considered as a given function.

ometries and, therefore, numerical methods have to be used in general. At the resonances, very strong enhancement of the electromagnetic field is achieved and the field distribution may present a fairly complex structure, which demands a very accurate modeling scheme. Techniques like the Discrete Dipole Approximation, the T-matrix method or the Green's Dyadic technique, have been applied for the computation of near-field optical problems. An overview of these and other methods can be found in Refs. [86, 87]. These numerical methods have allowed the computation of plasmon resonances for complex geometrical configurations such as isolated particles of irregular shapes [88], particles on top of a substrate [89, 90], interaction among particles [76, 91], cylinders of irregular cross sections [54,92] and gratings [84,93]. Numerical techniques have difficulties with large field gradients and to overcome this issue a Green's Dyadic method with Finite Elements has been developed [94]. Nevertheless most of the usual techniques are specific for one type of geometrical configuration or they are not flexible enough to be extended for the computation of all the mentioned geometrical arrangements. Therefore, here it is proposed the computation of surface plasmons in structures with a wide range of geometrical configurations using the MMP method with AMS.

As already stated earlier the whole treatment presented here is classical. Hence, macroscopic Maxwell equations and boundary conditions have been applied as well as bulk permittivity functions to model surface plasmons in nanoscopic systems.

It is worth mentioning that the applicability of such classical macroscopic approach may be questioned when size ranges of the underlying metallic structure tend towards the nanometer scale. Thus, with decreasing particle size fundamental processes give rise to spatial dispersion, namely the electron scattering at confined particle boundaries will affect the mean free path of conduction electrons, resulting in wavelength-shift and broadening of the surface-plasmon resonance [95–97]. Proper quantum surface effects arise within remarkably lower length scales around the Fermi wavelength of the conduction electron gas indicating a fundamental breakdown of all Mie-like theories. Nevertheless, balancing effects between the quantum-spillout phenomenon (causing red-shift) and the reduced screening of the Coulomb interaction (causing blue-shift) can result in a surprising agreement with classical predictions involving bulk dielectric functions [97] even for the size ranges addressed by the various geometries in the examples to be presented.

In the framework of metallic nanoparticles finite-size dependences originating from quantum effects are still under discussion. Here, the interest in surface-plasmon modes is mainly driven by the large field variations of this resonant state defining, hence, an attractive test case for the validation of computational electromagnetics codes. All computations in this section have been performed with MaX-1 [58] which contains an AMS procedure following the principles described in section 3.2.

In the computations in the following subsections, it is assumed that the relative permeability of all media is $\mu_r = 1$.

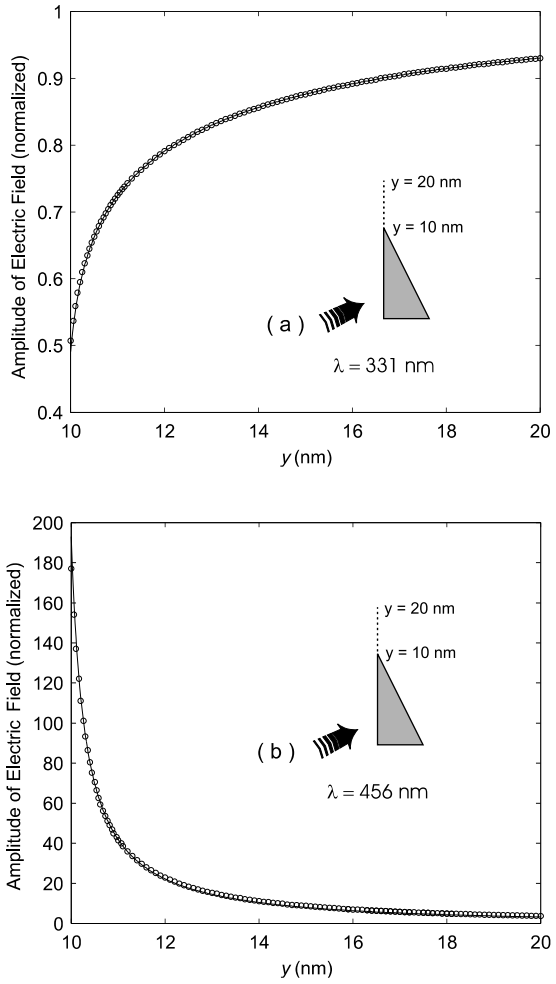

Fig. 3.6 Comparison of the electric field amplitude computed using two different techniques. The plots show the amplitude (normalized to the incident amplitude) along the dotted line (see insets). Circles: Green's Tensor Technique with Finite Elements, Line: MMP with Automatic Multipole Setting. (a) $\lambda = 331\,\mathrm{nm}$, (b) $\lambda = 456\,\mathrm{nm}$.

3.3.1 Cylinders with irregular cross section

Analytical solutions for scattering on cylindrical structures are available only for cylinders with circular or elliptical cross section. For circular cylinders whose diameter is small compared to the wavelength the main resonance occurs for $\Re[\varepsilon(\omega)] = -\varepsilon^{\mathrm{background}}$. However, to determine detailed features of the plasmon resonances of a cylinder with arbitrary cross section –such as, e. g., the enhancement of the electromagnetic field– a numerical computation is required. In this subsection calculations are shown for two different geometries in order to assess the accuracy of the method.

Fused cylinders

In the first computation, the scattering of a plane wave on a silver cylinder with the cross section depicted in Fig. 3.4(c) is presented. The background medium is vacuum and the relative permittivity of silver for the incident wavelength ($\lambda = 340\,\mathrm{nm}$) is $\varepsilon_r^{\mathrm{Ag}} = -1.16 + i\,0.30$. This wavelength corresponds to one of the surface modes of this structure [98]. The wave vector of the exciting field is $\mathbf{k} = \|\mathbf{k}\|\,\mathbf{e}_x$ and the electric field vector is contained in the XY plane (i.e., H polarization). Figure 3.5 displays the complexity of the electric field near to a small radius of curvature part of the interface. This justifies the main assumption for the AMS procedure: a dense multipole distribution is needed near the geometrical irregularities of the interface [Fig. 3.4(c)]. For this computation the highest relative error (see subsection 2.2.6) along the interface was 0.48 % and the average relative error along the interface was 0.012 % which demonstrate the high accuracy of the solution.

Triangular cross section cylinder

A second scattering computation is shown now in order to compare our results with reference data obtained with the Green's Tensor Technique with Finite Elements [94]. In the Figs. 3.6(a, b) it can be seen that the agreement between both techniques (including the maximum values of the electrical field) is excellent. The cross section geometry is plotted in Fig. 3.4(b). The wave vector of the incident plane wave is contained in the XY plane, and its direction is perpendicular to the triangle's hypotenuse, coming from the bottom-left of the figure (Fig. 3.6, insets). The electric field vector is contained in the XY plane (H polarization). For such a silver cylinder in vacuum the lowest and highest plasmon resonances occur for $\lambda = 331\,\mathrm{nm}$ and $\lambda = 456\,\mathrm{nm}$ [92]. For these wavelengths the dielectric constants are $\varepsilon_r^{\mathrm{Ag}}(\lambda = 331\,\mathrm{nm}) = -0.61 + i\,0.28$ and $\varepsilon_r^{\mathrm{Ag}}(\lambda = 456\,\mathrm{nm}) = -7.34 + i\,0.23$. Figure 3.6 depicts the amplitude of the electric field (normalized to the incident amplitude) along the vertical segment with $x = -5\,\mathrm{nm}$ and $y \in [10\,\mathrm{nm}, 20\,\mathrm{nm}]$. The average relative error along the boundary in the MMP computations was 0.013 % for the short wavelength and 0.22 % for the long one.

3.3.2 Circular cylinder near an interface

Proximity between particles modifies their respective surface plasmons [98]. This effect is of great interest in SERS because higher field enhancements can be achieved. An irregular particle presents a rich spectrum of plasmon resonances by itself and the spectrum resulting from the interaction with another object is even more complex. Hence, it may be very difficult to interpret this spectrum (especially if one takes into account that plasmons have complex resonance frequencies and, therefore, the modes broaden and overlap). For this reason, the study is restricted to the interaction of a simple structure (cylinder with circular cross section) with a substrate.

The simulated system is an infinitely long silver cylinder of radius $r = 25\,\mathrm{nm}$, near the interface between two different media. This interface is the XZ plane and the cylinder's axis is parallel to the Z axis (Fig. 3.7, insets). The medium above the interface is vacuum whereas below the interface $\varepsilon_r = 2.25$. For sim-

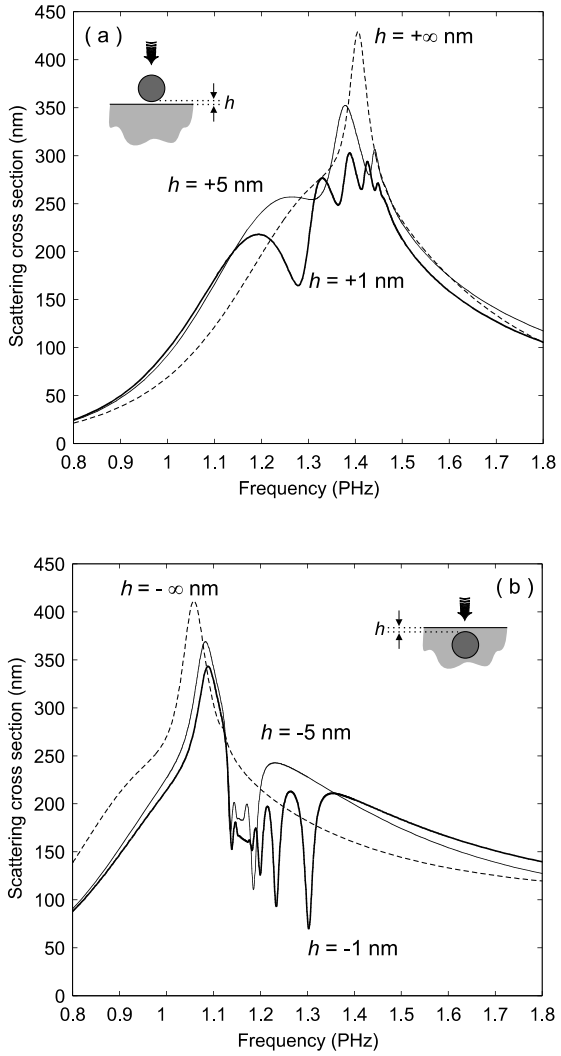

Fig. 3.7 Scattering cross section as a function of the frequency. (a) Cylinder above the interface, (b) cylinder below the interface. The parameter h denotes the distance between the cylinder and the interface.

plicity a Drude model was used to represent the dielectric constant of silver:

$$\varepsilon_r^{\mathrm{Ag}}(\omega) = 1 - \frac{\omega_p^2}{\omega(\omega + i\gamma)}, \tag{3.1}$$

with $1/\gamma = \tau = 1.45 \times 10^{-14}\mathrm{s}$ and $\omega_p = 1.32 \times 10^{16}\mathrm{s}^{-1}$. This $\varepsilon_r^{\mathrm{Ag}}(\omega)$ function suffices for the purposes desired here, but for more realistic results the experimental values of the dielectric constant should be used. The excitation is a plane wave

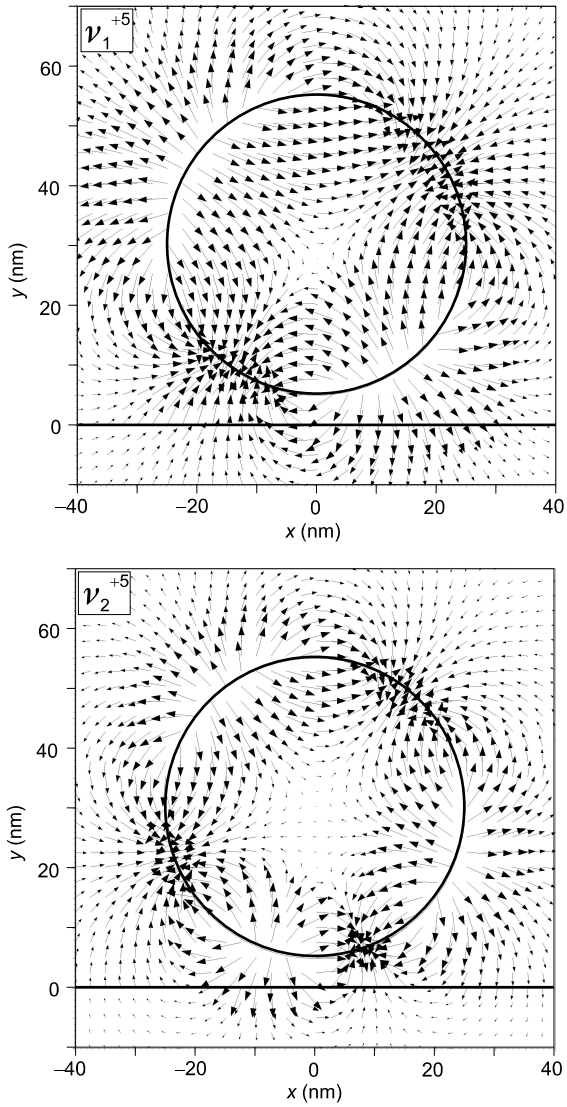

Fig. 3.8 Electric field for the two highest plasmon resonances (ν_1^{+5}, ν_2^{+5}) when $h = +5\,\mathrm{nm}$.

with $\mathbf{k} = -\|\mathbf{k}\|\,\mathbf{e}_y$ and the electric field vector is contained in the XY plane (H polarization). To study the influence of the coupling strength on the spectrum, the computations were performed for various distances between the interface and the cylinder. The distance between the interface and the cylinder closest point to the interface is h (positive if the cylinder lies in vacuum). In Fig. 3.7(a, b) the scattering cross section as a function of the exciting field frequency is plotted for several values of h.

For $h = \pm\infty$ a single maximum is found, which shifts according to the background medium. The amplitude of the electric field is enhanced by a factor 246 in vacuum ($h = +\infty$) and by a factor 167 in dielectric ($h = -\infty$). For $h = +5\,\text{nm}$, the spectrum presents a bump (for the frequency $\nu_0^{+5} = 1.26$ PHz) in addition with two distinct maxima ($\nu_1^{+5} = 1.3785$ PHz, $\nu_2^{+5} = 1.441$ PHz). The field patterns for ν_1^{+5} and ν_2^{+5} are different: the field lines of the first mode have a 4-fold pattern whereas the second mode has a 6-fold pattern (Fig. 3.8). For ν_0^{+5} the pattern is again 4-folded (which is the same as when there is no interface) and a small enhancement of 147 occurs, whereas for ν_2^{+5} the enhancement factor is 498. For $h = +1\,\text{nm}$ a more complex structure is revealed with more modes ($\nu_0^{+1} = 1.195$ PHz, $\nu_1^{+1} = 1.3295$ PHz, $\nu_2^{+1} = 1.3875$ PHz, $\nu_3^{+1} = 1.4255$ PHz, $\nu_4^{+1} = 1.448$ PHz) and stronger enhancements (up to 1658 for ν_3^{+1}). The field lines present a similar behavior as before: ν_1^{+1} 4-folded and ν_4^{+1} 10-folded (Fig. 3.9). The enhancement is again small for ν_0^{+1} (only 241) which is 4-folded. The spectrum is even more complex for cylinders under the interface [Fig. 3.7(b)].

In all the computations the maximum relative error along the interface was smaller than 0.2 % and the average relative error was smaller than 0.02 %.

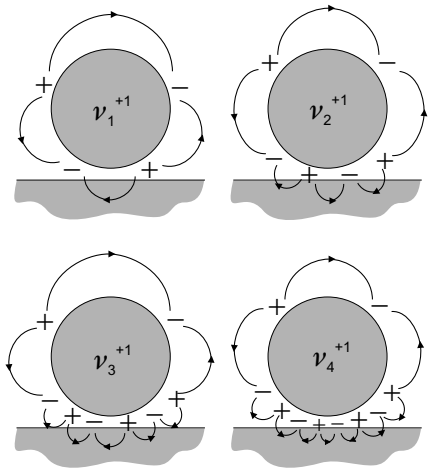

Fig. 3.9 Diagram of the electric field lines and charge distribution for the four highest plasmon resonances (ν_1^{+1}, ν_2^{+1}, ν_3^{+1}, ν_4^{+1}) when $h = +1\,\text{nm}$.

3.3.3 Periodic grating

The MMP method allows a very efficient computation of periodic structures [26]. For this purpose a special kind of boundary is implemented to define the fictitious boundaries of the system's primitive unit cell. Here, the AMS procedure is used to model a periodic grating. A straightforward modification to the AMS technique is required: the fields have to be expanded only inside the primitive cell and, therefore, for boundaries defining the unit cell only multipoles lying outside the

cell have to be generated.

The modeled system is a thin silver film (same dielectric constant as in the previous subsection) in vacuum. The metallic film has a thickness of 112 nm and lies in the XZ plane. It is corrugated on both sides of the film [the corrugations are parallel to the Z axis and there is no relative phase shift between the upper and lower gratings (Fig. 3.11, inset)]. The period of the upper corrugation is 150 nm and that of the lower corrugation is 300 nm. The geometry of the grooves consists of gaussian shaped dips inside the film:

$$H \exp\left[-\left(\frac{x-x_0}{w}\right)^2\right], \tag{3.2}$$

where the height H of the dips is 50.5 nm and the widths w are 10 nm at the upper corrugation and 12 nm at the lower one. The excitation is a plane wave with $\mathbf{k} = -\|\mathbf{k}\|\,\mathbf{e}_y$ and the electric field vector is contained in the XY plane (H polarization).

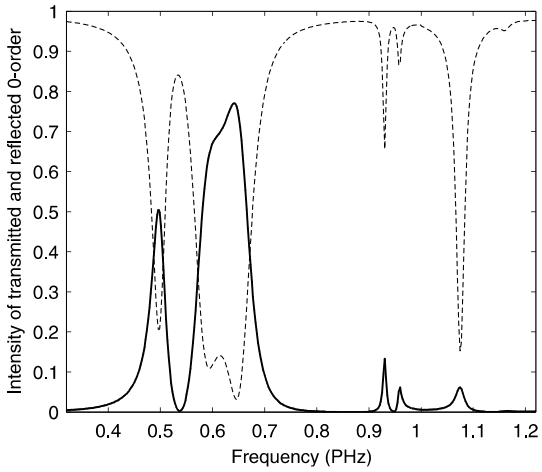

Fig. 3.10 Intensity of the 0-order waves transmitted (solid line) and reflected (dashed line) by the metallic thin-film grating.

For the frequencies considered in Figs. 3.10 and 3.11, the penetration depth is $\delta \approx c/(2\,\omega_p) \approx 13$ nm and in principle no transmission should be expected. Nevertheless, coupling of the plasmons in the upper grating with those of the lower corrugation produces a surface-plasmon-assisted resonant tunneling of light which has been investigated for complete [79,99] and incomplete [84] perforation of the film. This is clearly seen in Fig. 3.10 where the intensities of the 0-order transmitted and reflected waves are plotted and a power transmission of almost 80 % occurs for a resonant frequency. Another unexpected phenomenon is patent in Fig. 3.11 where the 1st-order intensities transmitted and reflected by the structure (which has 300 nm periodicity) are plotted. For a frequency of 1.08 PHz

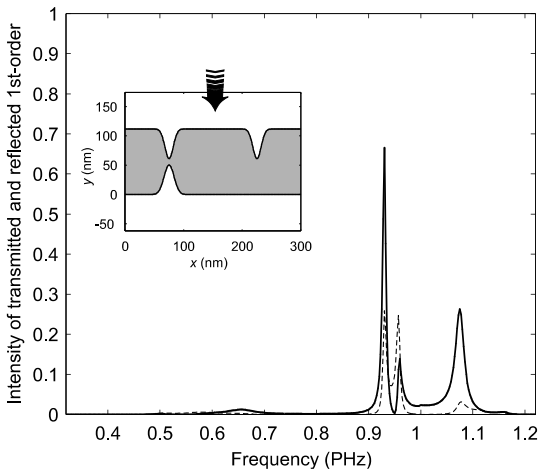

Fig. 3.11 Intensity of the 1st-order waves transmitted (solid line) and reflected (dashed line) by the grating (period 300 nm). Inset: geometry of one period of the grating.

(corresponding to a wavelength of 278 nm) the 1st-order is a propagating wave. But for this wavelength the periodicity of the upper corrugation (150 nm) should not allow any transmitted or reflected propagating order at all (except the 0-order). Again resonant plasmon coupling with the lower grating is responsible for this effect.

In all the computations regarding the metallic grating the maximum relative error along the interface was smaller than 0.34 % and the average relative error was smaller than 0.02 %.

3.4 Waveguides and photonic crystals

The AMS has been employed for the modeling of other electrodynamic problems. For instance, the computation of the modal fields and propagation constants of waveguides with complex cross sections, and the calculation of band structures of photonic crystals. These computations require the resolution of an eigenvalue problem. Since a method for the resolution of this type of problems will be presented in next chapter, these examples are deferred to sections 4.3, 4.4, and 4.5.

4

Computation of eigenvalue problems

4.1 Introduction

All applications shown in chapter 3 consisted in the resolution of diffraction problems: an incident field hits on an obstacle and it is scattered by it. The presentation of the MMP method in chapter 2 was formulated as a scattering problem as well. There are, however, many interesting situations where a self-sustained resonant oscillation occurs in an energetically closed system (in fact, the surface plasmons applications studied in chapter 3 were interesting systems precisely because a resonant mode was excited by an incident plane wave). In those resonant situations, e.g., cavities and waveguides, there is no excitation. This kind of configurations without excitation are mathematically formulated as eigenvalue problems.

In this chapter we will be concerned with the computation of several such problems, like the determination of the band structure and modal fields of photonic crystals, and the characterization of conventional as well as photonic crystal waveguides. The band structure of a photonic crystal is of primordial importance to understand the behavior of any system based on the photonic crystal concept. The significance of waveguide computations is obvious and it is not necessary to stress it here.

There is a standard way to solve eigenvalue problems within the MMP method. However, as it will be explained in section 4.2, for the type of systems studied in this chapter this procedure is not very well suited. Therefore, a novel technique for the resolution of eigenvalue problems with the MMP method is developed here. The technique is based on the investigation of the associated scattering problem. The resonances of this associated problem are determined, which correspond to the eigenvalues of the original eigenvalue problem.

In section 4.2 the technique is presented and some numerical details are elucidated. In the following sections several applications are presented: section 4.3 shows band structure computations of metallic photonic crystals, section 4.4 demonstrates photonic crystal defects, and in section 4.5 the procedure is applied to the determination of modes and propagation constants in waveguides.

4.2 Solution of non-linear eigenvalue problems with MMP

The determination of the propagation constants k_z in a waveguide (for given ω) or the computation of the resonant frequencies in a cavity are, in general, non-linear eigenvalue problems. Eigenvalue problems do not fit well in the formulation of MMP presented in chapter 2 because that description presented the MMP method as the resolution of a scattering problem with a given excitation $\Phi_{\text{exc}}(\mathbf{r})$. Nevertheless it is possible to solve homogeneous problems (i.e., without excitation) with MMP. The standard way to tackle an eigenvalue problem with MMP [17] consists in the following procedure [let us denote with λ the magnitude considered as eigenvalue (e.g., the propagation constant or the frequency)]: (*i*) One of the basis functions $\varphi_l^{\mathcal{D}_i}(\mathbf{r})$ expanding the field is artificially considered as excitation. In this way a scattering problem is defined. (*ii*) The matrix Eq. (2.8) is solved as a function of the parameter λ. We denote these solutions $F(\lambda)$. Note that the matrix $A(\lambda) = A_{\alpha\beta}(\lambda)$ depends on λ in a complex way, since this is a non-linear eigenvalue problem. (*iii*) The residual $R(\lambda) = \|A(\lambda)F(\lambda) - G(\lambda)\|_2$ of every computation in previous step is determined. (*iv*) The eigenvalues are obtained as those values of λ for which the *cost* function $c_1(\lambda) = R(\lambda)$ is minimum. The trivial solution $F = 0$ may appear as a minimum of the cost function as well. This happens when the basis function $\varphi_l^{\mathcal{D}_i}(\mathbf{r})$ is "reconstructed" (with negative sign) by the remaining basis functions. To avoid this effect, eventually, the minima of the cost function $c_2(\lambda) = R(\lambda)/\alpha(\lambda)$ are searched instead, where $\alpha(\lambda)$ is an amplitude defined in order to discard trivial solutions. The amplitude can be any function which is zero for trivial solutions. It has been observed that the procedure works efficiently when the excitation field $\varphi_l^{\mathcal{D}_i}(\mathbf{r})$ is not too different from the sought modal field. Nevertheless for waveguides or photonic crystals with complex shapes it is difficult to know a priori how the modes should look like. Therefore a different method is proposed which does not rely on setting as excitation a basis function similar to the sought mode.

The method is inspired by the surface plasmon applications shown in chapter 3. In those examples, the existence of a resonant mode of the structure leaves its signature as a resonance in the scattering cross section when the structure is excited by a plane wave. Here, a similar procedure will be employed. The difference lies in the selection of the excitation field $\Phi_{\text{exc}}(\mathbf{r})$ (which is not a plane wave) and the cost functions $c(\lambda)$ where the signature of the resonant modes is sought (which are not the scattering cross section). Related concepts have also been employed in the context of the Method of Auxiliary Sources [29, 100] and the Finite Difference Time Domain method (FDTD) [101–103].

4.2.1 Foundation of the method

The basis of the method for the determination of the eigenvalues will be now described. It is not intended to present the argument rigorously (in the mathematical sense of the word), but only to illuminate it from the perspective of the spectral theory of the involved operators. In this subsection the Dirac notation of bras and kets is employed.

Let us consider the following eigenvalue problem in a Hilbert space:

$$[\lambda\mathbb{I} - \mathbb{H}(\lambda)]|\phi_\lambda\rangle = |0\rangle, \tag{4.1}$$

where $\mathbb{I}$ denotes the identity operator and $\mathbb{H}(\lambda)$ is the operator we are interested in. The dependence on λ of the operator $\mathbb{H}$ serves as a reminder of the non-linearity of the eigenvalue problem. The eigenvector corresponding to the eigenvalue λ is denoted by $|\phi_\lambda\rangle$, and $|0\rangle$ is the null vector. The paradigmatic example of Eq. (4.1) is the Helmholtz equation $[k^2 + \Delta]\phi_k(\mathbf{r}) = 0$ supplemented with suitable boundary conditions for various problems such as metallic waveguides, free space, etc.

When the appropriate mathematical conditions [104–106] are met, the spectrum $\sigma(\mathbb{H})$ of the operator has a point part (corresponding to the bound states) and a continuous part (corresponding to the radiation states):

$$\sigma(\mathbb{H}) = \sigma_\mathrm{p}(\mathbb{H}) \cup \sigma_\mathrm{c}(\mathbb{H}) = \{\lambda_j\} \cup \{\lambda(k)\}, \tag{4.2}$$

where j is a discrete index and k a continuous one. The corresponding eigenvectors are denoted by $|u_j\rangle$ and $|v(k)\rangle$, respectively. The two examples mentioned before do only possess point and continuous spectrum, respectively, and the associated eigenvectors (in position representation) are

$$\begin{aligned} &\langle\mathbf{r}|u_j\rangle = u_j(\mathbf{r}) \quad \text{metallic waveguide} \\ &\langle\mathbf{r}|v(\mathbf{k})\rangle = \tfrac{1}{(2\pi)^{\frac{3}{2}}} e^{i\mathbf{k}\cdot\mathbf{r}} \quad \text{3D free space,} \end{aligned} \tag{4.3}$$

[the continuous index k labeling the eigenvalues in $\sigma_\mathrm{c}(\mathbb{H})$ becomes a vector index $\mathbf{k}$ for 3D problems].

With the appropriate mathematical conditions, the eigenvectors constitute an orthonormal (generalized) basis, which permits (formally) a spectral decomposition of the identity:

$$\mathbb{I} = \sum_j |u_j\rangle\langle u_j| + \int \mathrm{d}k\, |v(k)\rangle\langle v(k)|, \tag{4.4}$$

and of the operator $\mathbb{H}$:

$$\mathbb{H} = \sum_j \lambda_j |u_j\rangle\langle u_j| + \int \mathrm{d}k\, \lambda(k) |v(k)\rangle\langle v(k)|. \tag{4.5}$$

The application of these decompositions to the second example (3D free space) mentioned above gives the well known relations

$$\langle\mathbf{r}|\mathbb{I}|\mathbf{r}'\rangle = \delta(\mathbf{r} - \mathbf{r}') = \frac{1}{(2\pi)^3} \int_{\mathbb{R}^3} \mathrm{d}\mathbf{k}\, e^{i\mathbf{k}\cdot(\mathbf{r}-\mathbf{r}')}, \tag{4.6}$$

and

$$\langle\mathbf{r}|-\Delta|\mathbf{r}'\rangle = \frac{1}{(2\pi)^3} \int_{\mathbb{R}^3} \mathrm{d}\mathbf{k}\, k^2 e^{i\mathbf{k}\cdot(\mathbf{r}-\mathbf{r}')}. \tag{4.7}$$

The following scattering problem is associated with the eigenvalue problem (4.1):

$$[\lambda\mathbb{I} - \mathbb{H}(\lambda)]|f\rangle = |g\rangle, \tag{4.8}$$

where $|g\rangle$ is the excitation and $|f\rangle$ is the unknown. This problem is solved with help of the resolvent operator $\mathbb{R}_\lambda = [\lambda\mathbb{I}-\mathbb{H}(\lambda)]^{-1}$ which has the following spectral decomposition:

$$\mathbb{R}_\lambda = \sum_j \frac{1}{\lambda - \lambda_j}|u_j\rangle\langle u_j| + \int \mathrm{d}k\, \frac{1}{\lambda - \lambda(k)}|v(k)\rangle\langle v(k)|. \tag{4.9}$$

In position representation the resolvent operator becomes the Green's function $G(\mathbf{r}, \mathbf{r}')$. For the metallic waveguide:

$$\langle \mathbf{r}|\mathbb{R}_k|\mathbf{r}'\rangle = G_k(\mathbf{r}, \mathbf{r}') = \sum_j \frac{u_j(\mathbf{r})u_j(\mathbf{r}')^*}{k^2 - k_j^2}, \tag{4.10}$$

and for 3D homogeneous free space:

$$\langle \mathbf{r}|\mathbb{R}_k|\mathbf{r}'\rangle = G_k(\mathbf{r}, \mathbf{r}') = \frac{1}{(2\pi)^3}\int_{\mathbb{R}^3} \mathrm{d}\hat{\mathbf{k}}\, \frac{1}{k^2 - \hat{k}^2} e^{i\hat{\mathbf{k}}\cdot(\mathbf{r}-\mathbf{r}')} = \frac{e^{ik|\mathbf{r}-\mathbf{r}'|}}{|\mathbf{r}-\mathbf{r}'|}. \tag{4.11}$$

Equation (4.9) encapsulates in a distinct way the idea of the method. When the resolvent operator is applied to a given excitation:

$$|f\rangle = \mathbb{R}_\lambda|g\rangle = \sum_j \frac{1}{\lambda - \lambda_j}|u_j\rangle\langle u_j|g\rangle + \int \mathrm{d}k\, \frac{1}{\lambda - \lambda(k)}|v(k)\rangle\langle v(k)|g\rangle, \tag{4.12}$$

the following behavior as a function of λ is observed. (*i*) For $\lambda = \lambda_j \in \sigma_\mathrm{p}(\mathbb{H})$, $\mathbb{R}_\lambda$ does not exist. Equation (4.12) shows that the projection of $|f\rangle$ on $|u_j\rangle$ grows without bound when $\lambda \to \lambda_j$ (as long as the excitation is not orthogonal to the eigenvector corresponding to that eigenvalue, $\langle u_j|g\rangle \neq 0$). This means that the eigenvalues of $\mathbb{H}$ can be determined as the divergencies of a suitable cost function of λ, such as for example the norm $\langle f|f\rangle$ of the solution of the associated scattering problem. (*ii*) For $\lambda = \lambda(k) \in \sigma_\mathrm{c}(\mathbb{H})$, the resolvent $\mathbb{R}_\lambda$ exists but it is an unbounded operator. That means that, for certain excitations $|g\rangle$, the function $\langle f|f\rangle$ diverges as well. If one uses the divergences of $\langle f|f\rangle$ as a signature of the eigenvalues one could confuse a point in $\sigma_\mathrm{p}(\mathbb{H})$ with a point in $\sigma_\mathrm{c}(\mathbb{H})$. A different possibility is selecting as excitation a point source $|g\rangle = |\mathbf{r}_0\rangle$ (with a non-zero projection on the sought mode $\langle u_j|\mathbf{r}_0\rangle \neq 0$) and using as cost function the value of the solution $|f\rangle$ at a given point: $\langle \mathbf{r}|f\rangle = \langle \mathbf{r}|\mathbb{R}_\lambda|\mathbf{r}_0\rangle$. This is nothing else than the Green's function, as it was shown in the examples of Eq. (4.10) and (4.11). Note that the Green's function is known to exist and to be regular (except, of course, at the position of the excitation) for the values of $\lambda \in \sigma_\mathrm{c}(\mathbb{H})$. Hence, it only presents divergencies for $\lambda \in \sigma_\mathrm{p}(\mathbb{H})$. Equation (4.11) is an example of this statement for the simple case of 3D free space.

In general, $\langle \mathbf{r}|\mathbb{R}_\lambda|g\rangle$ with almost arbitrary excitation $|g\rangle$ will present resonances for $\lambda \in \sigma_\mathrm{p}(\mathbb{H})$. Other cost functions are also appropriate as explained in subsections 4.2.2 and 4.2.3.

4.2.2 Implementation of the method in MMP

To implement the previous ideas in the MMP method, the following procedure is adopted. The system is modeled as described in chapter 2, but additionally an extra monopolar source (the MMP-excitation) is introduced at point $\mathbf{r}_0$. It is worth noting that using a monopolar function [Eq. (2.6) with $n_l = 0$] as MMP-excitation, one obtains the correct behavior of a $\delta(\mathbf{r} - \mathbf{r}_0)$ excitation in the sense of subsection 4.2.1. Then, the density of electromagnetic energy at a given point $\mathbf{r}$ is computed as a function of the parameter λ (typically the angular frequency, $\lambda = \omega$, or the propagation constant, $\lambda = k_z$). The energy density is chosen instead of the Green's function itself, because the first function is positive. Finally, the eigenvalues are determined as the divergencies (resonances) of the energy density. Examples will be given in section 4.3.

4.2.3 Numerical issues

If Eq. (4.8) is projected on $|u_j\rangle$, the following is obtained:

$$(\lambda - \lambda_j) f_j = g_j, \tag{4.13}$$

where f_j, g_j are the projections of the respective vectors on the eigenvector $|u_j\rangle$. Here, it is again seen that $|f_j(\lambda)|^2$ *strictly diverges* for the value of the j-th eigenvalue.

As it was explained in subsection 2.2.6, within MMP the matrix equations are overdetermined. In this case Eq. (4.13) is substituted by

$$[(\lambda - \lambda_j)\delta_{ji} + \Delta\lambda_{ji}^{\xi_j}] f_i = g_j + \Delta g_j^{\xi_j}, \tag{4.14}$$

where ξ_j ($\xi_j = 1, \ldots, E_j$) labels the approximately redundant equations for the j-th eigenvector. The terms $\Delta\lambda_{ji}^{\xi_j}$ with the same j and different ξ_j are not exactly equal because the extra equations are not exactly redundant but only nearly redundant (the same is valid for $\Delta g_j^{\xi_j}$). These factors $\Delta\lambda_{ji}^{\xi_j}$, $\Delta g_j^{\xi_j}$ are very small in comparison to λ_j and g_j, respectively. Neglecting the terms with $i \neq j$ the system becomes

$$(\lambda - \lambda_j^{\xi_j}) f_j = g_j^{\xi_j}, \tag{4.15}$$

where $\{\lambda_j^{\xi_j} = \lambda_j - \Delta\lambda_{jj}^{\xi_j}\}$ (respectively $\{g_j^{\xi_j} = g_j + \Delta g_j^{\xi_j}\}$) is a set of values scattered around the true λ_j (respectively g_j). The solution of Eq. (4.15) in the least squares sense is

$$f_j(\lambda) = \frac{\overline{g_j}\,\lambda - \overline{\lambda_j g_j}}{\left(\lambda - \overline{\lambda_j}\right)^2 + \sigma_{\lambda_j}^2}, \tag{4.16}$$

where the bar denotes the mean with respect to the index ξ_j and σ_{λ_j} is the variance of the set $\{\lambda_j^{\xi_j}\}$. This function is the product of a lorentzian and a linear function. Analog to the non-overdetermined case, the value of $|f_j(\lambda)|^2$ resonates and grows when λ approaches eigenvalue λ_j. However, when λ is very close to λ_j, the value of $|f_j(\lambda)|^2$ decreases again and becomes zero for $\lambda = \overline{\lambda_j g_j}/\overline{g_j}$. In summary, the shape of the resonance is a lorentzian curve –whose width is

controlled by the dispersion of the set $\{\lambda_j^{\xi_j}\}$– which is pinched almost in its center. Figure 4.1 shows an example of this behavior. For this model example two eigenvalues and five nearly redundant equations for each of them where considered ($j = 1, 2$; $\xi_1 = \xi_2 = 1, \ldots, 5$). Thus, the overdetermined system does not lead to a strict divergency of $\sum_j |f_j(\lambda)|^2$ for the eigenvalues' frequencies. Note that this is not a real physical phenomenon but a numerical effect due to the overdetermination of the system.

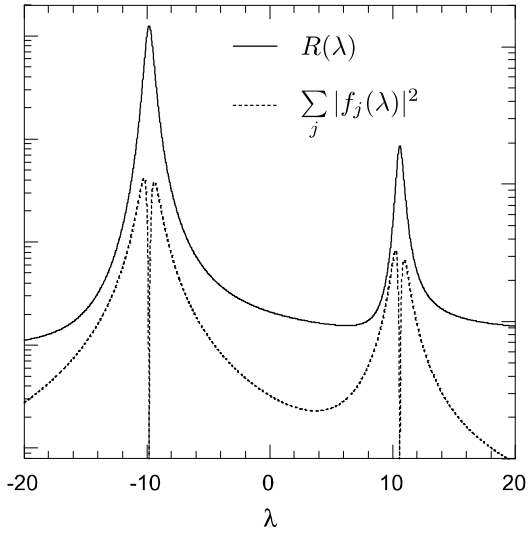

Fig. 4.1 Behavior of the cost functions $\sum_j |f_j(\lambda)|^2$ and $R(\lambda)$. In this model example there are only two eigenvalues, ($\lambda_{1,2} \approx \pm 10$). The first cost function (dashed line) presents dips at the centers of the resonances due to the overdetermination of the equations. The residual $R(\lambda)$ (continuous line) has no dips.

When the MMP model is correct, the dispersion of the set $\{\lambda_j^{\xi_j}\}$ is very small. This means that the width of the lorentzian is small and the dip at its center is even narrower. In this case an extremely fine discretization in λ would be required to resolve the dip at the center of the lorentzian resonance. Examples will be shown in subsection 4.3.1.

By contrast with the amplitude $f_j(\lambda)$, the residual $R(\lambda)$ is given by

$$R(\lambda) = \sum_j E_j \left[\overline{g_j^2} - \frac{(\overline{g_j}\,\lambda - \overline{\lambda_j g_j})^2}{\left(\lambda - \overline{\lambda_j}\right)^2 + \sigma_{\lambda_j}^2} \right]. \tag{4.17}$$

Besides the constant terms, each term in the sum is again the product of a lorentzian function and a polynomial in λ. It can be shown that the residual has maxima for the values $\overline{\lambda_j g_j}/\overline{g_j}$ [assuming that the interaction between the different terms in the sum of Eq. (4.17) is negligible]. In brief, the residual has maxima exactly at those points where $|f_j(\lambda)|^2$ is pinched. This is observed in Fig. 4.1.

It is important to be aware of the numerical behavior of the energy density (i.e., the dips at the center of the resonance). Otherwise, occasionally, one single eigenvalue could be mistaken as two different eigenvalues. Although this could be seen as an issue, we have never experienced any difficulty because of that. In fact, when the MMP model is correct, the dip in the resonance curve is always so narrow that an extra fine discretization has to be used to resolve the dip. However, the utilization of the residual $R(\lambda)$ as cost function can be employed in case of doubt. Examples will be shown in subsection 4.3.1.

4.3 Band structures of metallic photonic crystals

Understanding the behavior of defect-free photonic crystals and designing devices based upon them require a knowledge of the wave propagation properties in the crystal. This information is contained in the band structure and eigenmodes of the periodic structure. At present, after more than one decade of investigations, photonic band gap calculations are continually performed. In the most basic level, it is important to find perfect crystal structures with improved features. In this context, new geometries have been investigated, e.g. the Kagomé structure [107], and symmetry techniques to enhance the gaps have been applied [108–110]. The next level comprises the characterization of crystals with impurities (such as cavities [111,112] and channel waveguides [113–116]) and surface waves [117,118], which are likely needed for the design of devices with useful functionalities. The band structure and modal fields are essential tools here as well.

Initially, most computational techniques focused on dielectric materials with frequency-independent parameters, but there has been an increasing interest in photonic crystals with frequency-dependent permittivities $\varepsilon(\omega)$. In particular, the inclusion of metallic components is actively researched since it can enlarge the size of the gaps [119,120]. The occurrence of flat bands related with plasmon resonances of the individual scatterers in the crystal may be used for other applications [121] due to the very low group velocities involved. Finally, metallic photonic crystal structures are of obvious interest considering new applications in the microwave regime [122].

There exists a vast literature documenting the various methods for the computation of photonic band structures. Despite the convergence problems alluded to by many authors [123–127] when high dielectric contrasts are involved, the plane wave method [15, 128] is the most used one. In its simplest formulation it only treats the case of frequency-independent materials, but some authors have extended it for particular functional forms of $\varepsilon(\omega)$ [129–131]. Nevertheless, those generalizations are not always satisfactory as noted in Refs. [101] and [132]. A second class of methods (Korringa-Kohn-Rostoker [127, 133], augmented plane wave [134] and others based on scattering matrices [135]) uses mainly spherical functions instead of plane waves as basis functions to expand the fields. These techniques are very accurate as a rule and can handle frequency dependent materials, but they are only appropriate for photonic crystals with spherical elements. A third possibility is the FDTD [103, 136] method. The standard formulation does not cover the frequency-dependent case, but generalizations have already been proposed [101,137] (which require considering non-local effects in time). In

particular, Sakoda [138] has shown FDTD computations of band structures and modal fields for perfect crystals, cavities and channel waveguides with dielectric or metallic components. There are other alternatives such as the transfer matrix method [139] or the finite element method [140].

At present only Sakoda's approach has proven to be capable of computing band structures for arbitrary frequency dependence and arbitrary geometry; it has also been applied to the difficult case of metallic structures in H polarization, where the fields can be strongly localized at the metal surface (surface plasmons). Here an alternative frequency domain method, based on MMP, is proposed for the same kind of metallic photonic crystal configuration. Like the second class of methods mentioned before, the basis functions most frequently employed by the MMP method are spherical functions (cylindrical for two-dimensional problems). Nevertheless, the use of multiple functions with different origins allows one to achieve a good convergence for non circular shapes as well. MMP can handle arbitrary frequency-dependent permittivities, including metallic materials.

Before the method for the computation of band structures is presented, a few further elements required for the simulation of periodic systems with MMP [26] will be summarized. The computation can be restricted to one single primitive cell of the periodic system, which includes several domains $\mathcal{D}_i$ representing the elements contained in it. As primitive cell the parallelogram defined by the primitive vectors $\mathbf{a}_1$ and $\mathbf{a}_2$ is chosen. Two fictitious boundaries along $\mathbf{a}_1$ and $\mathbf{a}_2$ are necessary, where additional collocation points will be introduced. The basis functions $\varphi_l^{\mathcal{D}_i}(\mathbf{r})$ expand the field only inside the primitive cell. Several multipole and Bessel expansions located in the cell are employed to represent the field scattered at the elements contained in it. Additionally, a set of multipole expansions around the cell is needed. These sources model the incident radiation field inside the primitive cell stemming from the rest of the crystal. Examples of the choice of the basis functions will be shown for the specific structures computed in subsections 4.3.1 and 4.3.2. The fields should satisfy Bloch's theorem:

$$\Phi^{\mathbf{k}}(\mathbf{r}+\mathbf{R}_{pq}) = e^{i\mathbf{k}\cdot\mathbf{R}_{pq}}\Phi^{\mathbf{k}}(\mathbf{r}), \tag{4.18}$$

where $\mathbf{k}$ belongs to the first Brillouin zone (1^{st}BZ) and $\mathbf{R}_{pq} = p\mathbf{a}_1 + q\mathbf{a}_2$ with $p, q \in \mathbb{Z}$. Equation (4.18) is employed to define Bloch boundary conditions which have to be fulfilled at the fictitious boundaries defining the primitive cell. For later use, the notation for the reciprocal lattice points is introduced: $\mathbf{G}_{rs} = r\mathbf{b}_1 + s\mathbf{b}_2$ with $r, s \in \mathbb{Z}$ and $\mathbf{a}_i \cdot \mathbf{b}_j = 2\pi\delta_{ij}$.

Let us apply the method presented in section 4.2 to the case of photonic crystals. Here, the eigenvalues λ are the square frequencies of the bands. To establish the approach let us compute the field excited by a source. We take $k_z = 0$ and H polarization for the sake of simplicity and because the cases studied in subsections 4.3.1 and 4.3.2 satisfy these conditions. Nevertheless, analog derivations can be done for the general 3D case [121, 141, 142]. The Bloch modes $H_z^{\mathbf{k},n}(\mathbf{r})$ (n labels the different bands) are the solutions of the eigenvalue problem

$$\Big[\frac{(\omega^{\mathbf{k},n})^2}{c^2} + \nabla_{\mathrm{T}} \cdot \frac{1}{\varepsilon_r(\mathbf{r}, \omega^{\mathbf{k},n})}\nabla_{\mathrm{T}}\Big] H_z^{\mathbf{k},n}(\mathbf{r}) = 0, \tag{4.19}$$

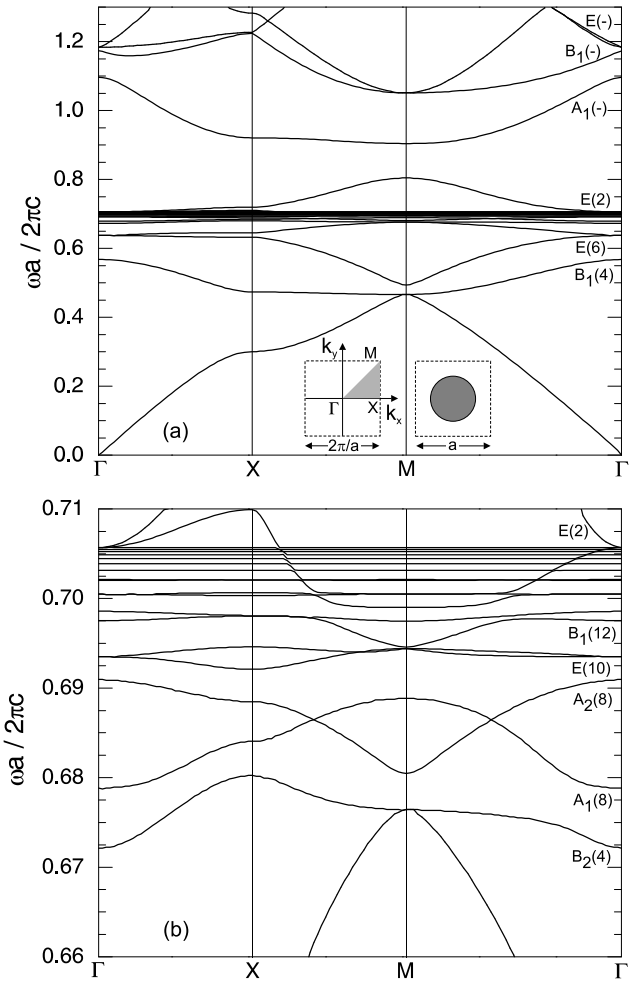

Fig. 4.2 Band structure of a square lattice of metallic circular cylinders. The bands are labeled with the corresponding irreducible representations of $\mathcal{G}_0(\Gamma)$. The bands corresponding to mPR are additionally labeled with the number of lobes of the plasmon from which they mainly stem. (a) General view. (b) Detailed view of the flat bands. The insets of (a) show the first Brillouin zone (left) and the primitive cell (right).

(c is the speed of light in vacuum and $\mu_r = 1$ is assumed). The Bloch modes constitute a basis:

$$\int_{1^{\text{st}}\text{BZ}} d\mathbf{k} \sum_{n=1}^{\infty} H_z^{\mathbf{k},n}(\mathbf{r}) H_z^{\mathbf{k},n}(\mathbf{r}')^* = \delta(\mathbf{r} - \mathbf{r}'). \tag{4.20}$$

The inhomogeneous problem reads

$$\left[\frac{\omega^2}{c^2} + \nabla_{\text{T}} \cdot \frac{1}{\varepsilon_r(\mathbf{r}, \omega)} \nabla_{\text{T}}\right] H_z(\mathbf{r}) = H_{z,\text{exc}}(\mathbf{r}), \tag{4.21}$$

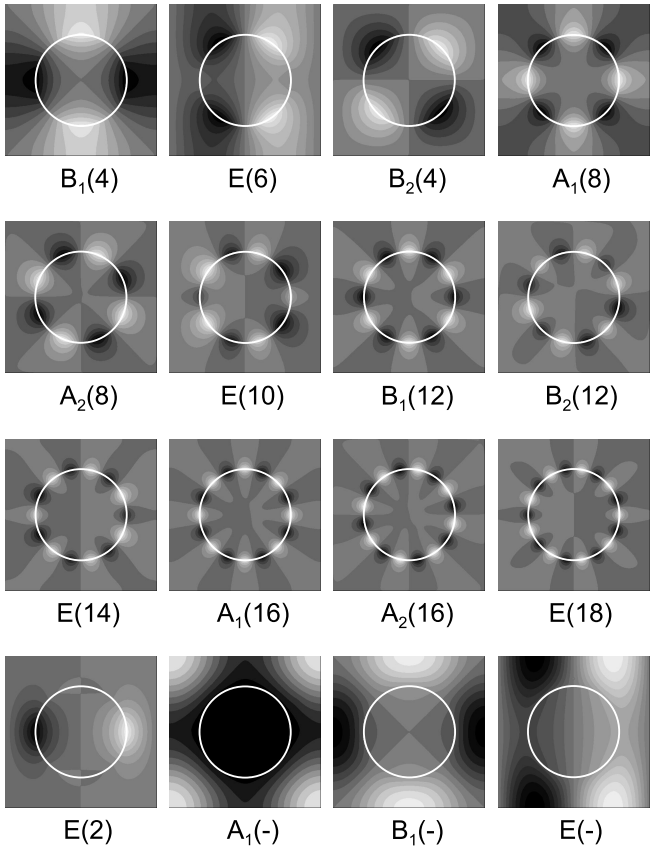

Fig. 4.3 Eigenmodes (at Γ point) of a square lattice of metallic circular cylinders. The plotted field is $H_z^{\Gamma}(\mathbf{r})$. The modes are labeled with the corresponding irreducible representations of $\mathcal{G}_0(\Gamma)$. The modes corresponding to mPR are additionally labeled with the number of lobes of the plasmon from which they mainly stem. For modes labeled with E, the other mode corresponding to the same eigenvalue looks the same but rotated 90°.

and its Green's function can be constructed with the help of the Bloch modes [143]:

$$G_\omega(\mathbf{r},\mathbf{r}') = c^2 \int\limits_{1^{\text{st}}\text{BZ}} d\mathbf{k} \sum_{n=1}^{\infty} \frac{H_z^{\mathbf{k},n}(\mathbf{r}) H_z^{\mathbf{k},n}(\mathbf{r}')^*}{\omega^2 - (\omega^{\mathbf{k},n})^2}. \tag{4.22}$$

The solution of Eq. (4.21) is then

$$H_z(\mathbf{r}) = \int\limits_{\mathbb{R}^2} d\mathbf{r}'\; G_\omega(\mathbf{r},\mathbf{r}') H_{z,\text{exc}}(\mathbf{r}'), \tag{4.23}$$

as can be verified using the closure equation [Eq. (4.20)].

Within the MMP method, the natural choice for the excitation is a multipolar function located in a certain point in the cell (monopoles have been mainly used, but the procedure works with higher order multipolar functions as well). When a monopole is introduced in position $\mathbf{r}_0$ inside the primitive cell, a set of monopoles (with corresponding phases) are set in $\mathbf{r}_0 + \mathbf{R}_{pq}$ implicitly, because Bloch boundary conditions are used. Hence the excitation is

$$H_{z,\mathrm{exc}}^{\mathbf{k}_0}(\mathbf{r}) = \sum_{\mathbf{R}_{pq}} \delta(\mathbf{r} - \mathbf{r}_0 - \mathbf{R}_{pq}) e^{i\mathbf{k}_0 \cdot \mathbf{R}_{pq}}, \tag{4.24}$$

where $\mathbf{k}_0$ is the current wave vector in the 1$^{\mathrm{st}}$BZ. Inserting this excitation in Eq. (4.23) and using the identity

$$\sum_{\mathbf{R}_{pq}} e^{i\mathbf{R}_{pq} \cdot (\mathbf{k} - \mathbf{k}_0)} = S_{1^{\mathrm{st}}\mathrm{BZ}} \sum_{\mathbf{G}_{rs}} \delta(\mathbf{k} - \mathbf{k}_0 - \mathbf{G}_{rs}), \tag{4.25}$$

(where $S_{1^{\mathrm{st}}\mathrm{BZ}}$ is the area of the 1$^{\mathrm{st}}$BZ) one obtains:

$$H_z^{\mathbf{k}_0}(\mathbf{r}) = c^2 S_{1^{\mathrm{st}}\mathrm{BZ}} \sum_{n=1}^{\infty} \frac{H_z^{\mathbf{k}_0,n}(\mathbf{r}_0)^* H_z^{\mathbf{k}_0,n}(\mathbf{r})}{\omega^2 - (\omega^{\mathbf{k}_0,n})^2}. \tag{4.26}$$

When $\omega \to \omega^{\mathbf{k}_0,n}$ two important facts are evident from Eq. (4.26): first, the amplitude of the field diverges, and second the field becomes the Bloch mode $H_z^{\mathbf{k}_0,n}(\mathbf{r})$. Therefore, by detecting these resonances of the field, we can find both the eigenvalues $\omega^{\mathbf{k},n}$ and eigenmodes $H_z^{\mathbf{k},n}(\mathbf{r})$ of the homogeneous problem [Eq. (4.19)].

For a given $\mathbf{k}_0$, the resonances are detected as maxima of an appropriately chosen cost function $c(\omega)$. The energy density in a certain point of the cell $c_3(\omega)$, and the residual $c_4(\omega) = R(\omega)$ are suitable choices of the cost function as it was explained in subsection 4.2.3. For different positions of the excitation one obtains different functions $c(\omega)$, but the resonances of all these functions occur for the same frequencies. One has just to be careful that the location $\mathbf{r}_0$ of the excitation is not a zero of the sought mode. It can also be shown that only those modes that possess the same symmetry as the source are excited. This can be in fact used to separate modes of different symmetries with very similar or degenerate frequencies (examples will be shown in Fig. 4.4). Other authors have employed different excitations and functions $c(\omega)$ to detect the eigenvalues: Reference [102] (where a time domain technique is shown) uses a dipolar pulse (in time) as excitation and $c(\omega)$ is the Fourier transform of the field in a point of the cell. The energy radiated through a circumference around the excitation [101] also works properly as cost function.

To compute a complete band structure, the following procedure is employed. First, a given point $\mathbf{k}_{\mathrm{ini}}$ of the boundary of the irreducible 1$^{\mathrm{st}}$BZ is chosen and the eigenvalues $\omega^{\mathbf{k}_{\mathrm{ini}},n}$ are found following the lines explained above. Note that finding the eigenvalues by searching the maxima of $c(\omega)$ is a slower algorithm than other advanced methods presented for example in Ref. [128]. However, as

noted by several authors [123,130], when the permittivity is frequency-dependent the computation of the bands is a non-linear eigenvalue problem and the cited methods cannot be applied [there are exceptions for very specific functional forms of $\varepsilon(\omega)$]. Once the eigenvalues are known for $\mathbf{k}_{\mathrm{ini}}$, the point in reciprocal space is shifted to $\mathbf{k}_{\mathrm{ini}} + \delta\mathbf{k}$ and the procedure is iterated. The only difference is that now the eigenvalues can be localized much faster since it is only needed to search for the maxima of $c(\omega)$ in the neighborhood of each $\omega^{\mathbf{k}_{\mathrm{ini}},n}$. The use of this Eigenvalue Estimation Technique (EET) [17] compensates the large computational burden in the determination of $\omega^{\mathbf{k}_{\mathrm{ini}},n}$ for the initial point $\mathbf{k}_{\mathrm{ini}}$. The knowledge of the symmetry of the crystal is important while choosing the initial $\mathbf{k}_{\mathrm{ini}}$ point. If possible, it should be such that the point group $\mathcal{G}_0(\mathbf{k}_{\mathrm{ini}})$ of the $\mathbf{k}_{\mathrm{ini}}$ vector [144] has only irreducible representations. This excludes the possibility of having intersecting bands at point $\mathbf{k}_{\mathrm{ini}}$ (if accidental degeneracies are disregarded). Otherwise only one of the bands crossing at $\mathbf{k}_{\mathrm{ini}}$ will be traced by the EET. Only at points where two bands cross with the same slope (this may happen at high symmetry points of the 1$^{\mathrm{st}}$BZ) [145] is this EET likely to fail in tracing the bands. This problem can be avoided by starting the calculation from $\mathbf{k}_{\mathrm{ini}}$ points lying to the left and to the right of the problematic point and approaching to it.

Numerical computations –obtained with the described method– of the band structure of photonic crystals are presented now. The studied structures are metallic photonic crystals (invariant along the Z axis) in H polarization. Crystals composed of metallic materials were chosen not only due to the increasing interest shown recently for these systems, but also because only a few methods are able to compute band structures for arbitrary $\varepsilon(\omega)$. The H polarization was selected as a stringent test case for the method. In contrast to the E polarization, where the Bloch modes are uniquely modified plane waves, for H polarization other very flat bands appear which are related to the plasmon resonances of the individual components of the crystal. In this case, the fields are strongly localized at the interface of the metal. This localization poses additional problems for some techniques, whereas the nature of the multipole expansions can be advantageously exploited to treat this configuration.

In subsection 4.3.1 results obtained with the described method are compared to those obtained with a FDTD approach [132] for a crystal made of circular cylinders. By contrast, in subsection 4.3.2 a structure deviating from the circular geometry is computed. It is worth noting that there are virtually no reports about metallic (not perfectly conducting) photonic crystals with a cross section other than circular.

The numerical results presented here were computed with programs based on MaX-1 [58].

4.3.1 Square lattice of circular cross section cylinders

Here a square lattice with lattice constant a is considered. In each primitive cell there is one single cylinder with circular cross section of radius $r = 0.3a$ [Fig. 4.2(a) right inset]. The background is vacuum and the relative permittivity of the cylinders is given by the Drude model:

$$\varepsilon_r(\omega) = 1 - \frac{\omega_p^2}{\omega(\omega + i\gamma)}, \tag{4.27}$$

where the parameters ω_p and γ are chosen as in Ref. [132]: $\omega_p = 2\pi c/a$, $\gamma = \omega_p/100$. In order to compare our results with those of Ref. [132], in-plane propagation will be considered, i.e., the propagation constant k_z along the Z axis is set to zero. Note, however, that the proposed method is not restricted to in-plane propagation nor to a specific permittivity function.

The space group of this crystal is $p4m$ and its associated crystallographic point group is $4mm$ (C_{4v} in Schönflies notation). For the Γ point in the 1st BZ the group $\mathcal{G}_0(\Gamma)$ has four one-dimensional irreducible representations (A_1, A_2, B_1, B_2) and one two-dimensional irreducible representation (E). These representations are used to label the bands at the Γ point (the assignment was done by inspecting the modal fields). The band structure of this system is shown in Fig. 4.2 while the corresponding modal fields (for the Γ point) are plotted in Fig. 4.3. Observe that two different kinds of modes are present: modes of the first type (labeled with a dash inside the brackets) are large mainly in the vacuum and are essentially modified plane waves (mPW). The second type (labeled with a number inside the brackets) includes modes that are localized close to the cylinders' surface. These are essentially modified plasmon resonances (mPR) of the individual cylinders. To distinguish different mPR modes labeled with the same irreducible representation, a number is included which denotes the number of lobes n_L of the plasmon resonance from which they mainly stem.

In order to understand the relationship between the degeneracies at the Γ

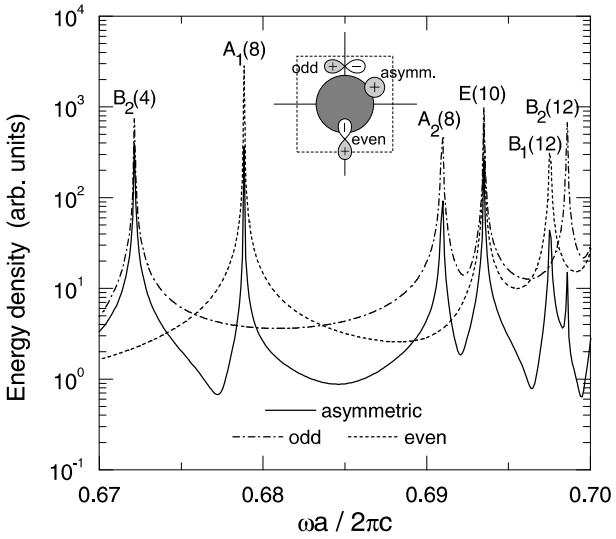

Fig. 4.4 Resonances of the energy density at an arbitrary point in the cell as a function of the normalized frequency (the point of the 1st BZ considered here is Γ). The denominations "asymmetric", "odd" and "even" are related to the type and position of the excitation and are explained in the text and in the inset.

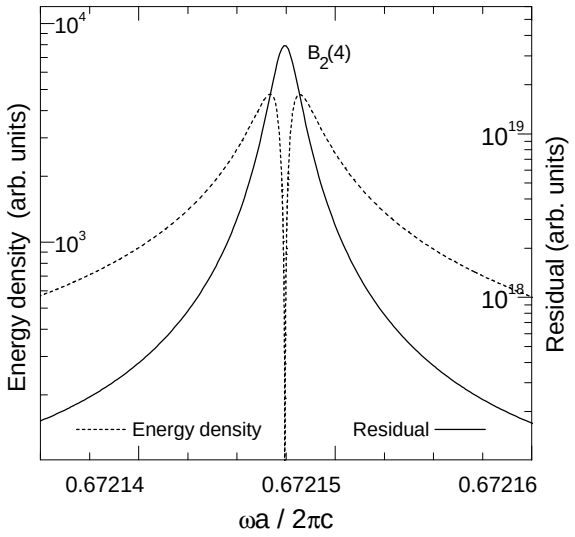

Fig. 4.5 Behavior of the energy density and residual cost functions close to the resonance peak $B_2(4)$ shown in Fig. 4.4. The energy density (dashed line) presents a dip at the center of the resonance curve due to the overdetermination of the equations. The residual $R(\omega)$ (continuous line) has no dip.

point and the number of lobes of a mPR mode the following argument can be used, which is presented first in general for the case of one isolated cylinder. Let be the cross section of this cylinder a regular polygon with n_{S} sides. The symmetry group $C_{n_{\mathrm{S}}v}$ of the cylinder has several irreducible representations of various dimensions. Let us now consider a plasmon resonance of the cylinder. The field corresponding to this resonance has n_{L} lobes (typically an even number). If the eigenvalue corresponding to this mode is non-degenerate, then the mode has to be invariant (up to a sign) under the group operations. But, in general, it is not possible distributing n_{L} lobes among n_{S} sides in such a way that the pattern is invariant under the group operations. When n_{L} and n_{S} are not compatible, the group operations transform the "asymmetric" pattern of the mode into a linear superposition of the modes corresponding to a degenerated eigenvalue. In this way they build the basis of an irreducible representation with dimension higher than 1. Specifically, those modes for which n_{L} is a multiple of n_{S} correspond to non-degenerate eigenvalues while the others correspond to degenerate ones.

The application of this argument to the geometry considered in this subsection goes as follows: One isolated circular cylinder is a polygon with $n_{\mathrm{S}} = \infty$ and, hence, all modes are degenerate. Since the group $C_{\infty v}$ of the circular cylinder has only one-dimensional (A_1, A_2) and two-dimensional (E_1, E_2, E_3, ...) irreducible representations, all modes come in pairs. These couples have an angular dependence given by the functions

$$\{\, \cos(\frac{n_{\mathrm{L}}}{2}\phi),\ \sin(\frac{n_{\mathrm{L}}}{2}\phi)\,\}, \qquad n_{\mathrm{L}} = 2k,\ k \in \mathbb{N}. \tag{4.28}$$

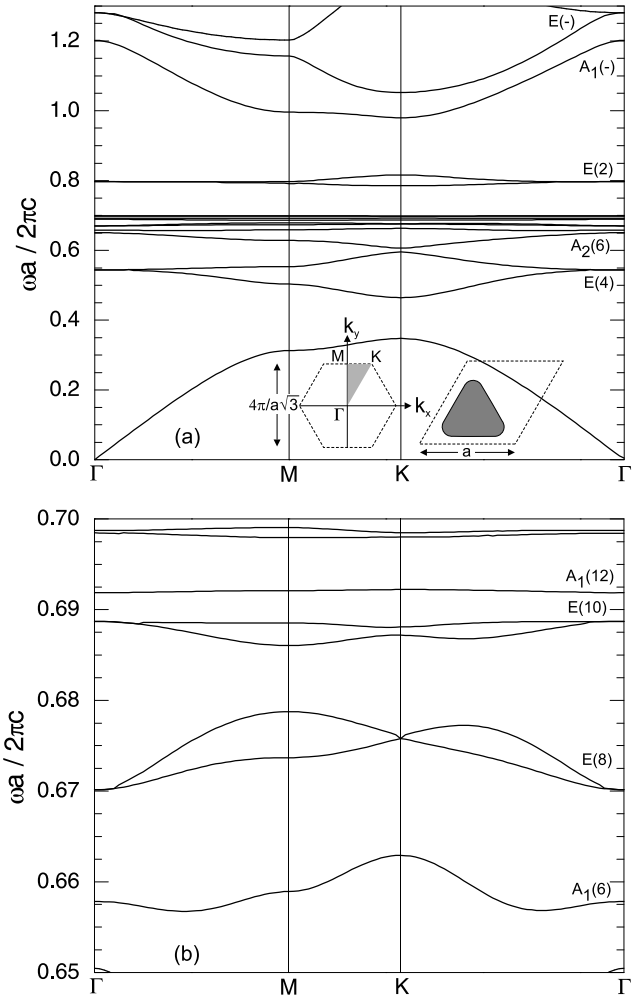

Fig. 4.6 Band structure of a triangular lattice of metallic triangular cylinders. The bands are labeled with the corresponding irreducible representations of $\mathcal{G}_0(\Gamma)$. The bands corresponding to mPR are additionally labeled with the number of lobes of the plasmon from which they mainly stem. (a) General view. (b) Detailed view of the flat bands. The insets of (a) show the first Brillouin zone (left) and the primitive cell (right).

When circular cylinders are arranged in a square lattice, the group to consider (for the Γ point) is C_{4v}. Therefore, the non-degenerated eigenvalues will be now those corresponding to $n_{\mathrm{L}} = 4k$, $(k \in \mathbb{N})$ while for $n_{\mathrm{L}} \neq 4k$ the eigenvalues will have a two-fold degeneracy. This is consistent with the band structure shown in Fig. 4.2. In summary: the degeneracy of eigenvalues corresponding to modes with $n_{\mathrm{L}} = 4k$ of the isolated cylinder is lifted when they are arranged in the square lattice. This is easy to understand from a perturbation point of view: If one considers, for instance, the mode with $n_{\mathrm{L}} = 4$ of an isolated cylinder and

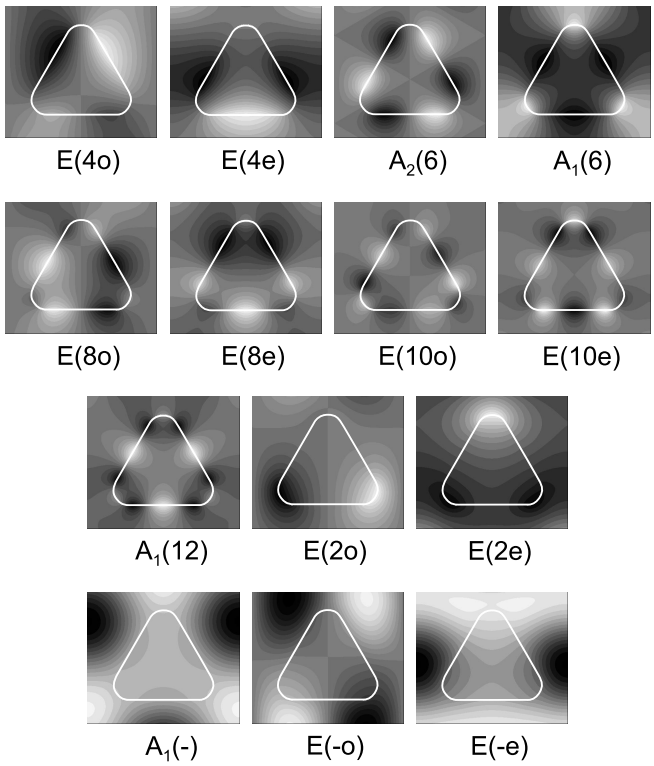

Fig. 4.7 Eigenmodes (at Γ point) of a triangular lattice of metallic triangular cylinders. The plotted field is $H_z^{\Gamma}(\mathbf{r})$. The modes are labeled with the corresponding irreducible representations of $\mathcal{G}_0(\Gamma)$. The modes corresponding to mPR are additionally labeled with the number of lobes of the plasmon from which they mainly stem. The degenerated modes are tagged with an "o" or "e" corresponding to odd or even modes under reflections in the vertical symmetry plane.

arranges this modal field in a square lattice, one observes that the overlapping of modes of contiguous cylinders is different for the two functions in Eq. (4.28). This is because for the cosine the lobes are directed toward the nearest neighbors whereas for the sine the lobes point along the diagonals. For modes with $n_{\mathrm{L}} \neq 4k$, it is clear that, when the modes with cosine and sine angular dependence are arranged in a lattice, the two patterns look exactly alike (modulo a rotation of 90°) and therefore the frequency of the eigenvalues is shifted –with respect to that of the isolated cylinder– but the degeneracy is not removed.

The following basis functions were employed to obtain the presented numerical results. The field inside the cylinder is modeled with a Bessel expansion of order n_{B} at its center, and the field around the cylinder is simulated with one multipole expansion of order $n_{\mathrm{H,in}}$ at its center plus four multipole expansions of order $n_{\mathrm{H,out}}$ at the nearest neighbors centers. A multipolar function of zero (monopole) or first (dipole) order in a certain point of the cell was chosen as

excitation. For the lowest and highest bands $n_{\mathrm{B}} = n_{\mathrm{H,in}} = 10$ and $n_{\mathrm{H,out}} = 5$ is enough to achieve good accuracy (1% averaged relative error or better); for the very flat bands corresponding to mPR with a high number of lobes and very localized fields $n_{\mathrm{B}} = n_{\mathrm{H,in}} = 15$ $n_{\mathrm{H,out}} = 7$ were used.

As cost function the energy density at an arbitrary point in the cell was chosen. This function is shown in Fig. 4.4. The fine details of the behavior of this function (which were analyzed in subsection 4.2.3) are demonstrated in Fig. 4.5. The discretization used in Fig. 4.4 shows the maxima without resolving the dip. As mentioned in subsection 4.2.3, only when a much finer discretization is employed it is possible to resolve the dip, as in Fig. 4.5, which shows a magnified view of the $\mathrm{B}_2(4)$ peak of Fig. 4.4 but with a very thin ω-discretization. To stress the importance of the location $\mathbf{r}_0$ and multipolar order n_l of the excitation, the cost function was computed for several source locations and orders: first, for a monopole [$n_l = 0$ in Eq. (2.6)] asymmetrically located, second, for a dipole located on the vertical symmetry plane (not in the center of the cylinder) and odd under reflections in this plane [$n_l = 1$ and cosine in Eq. (2.6)], and third, for an equally located dipole but with opposite parity [$n_l = 1$ and sine in Eq. (2.6)]. Figure 4.4 shows that modes with a symmetry other than that of the source are not excited. As explained above, this can be used to resolve closely located eigenvalues corresponding to different symmetries.

The results presented here are similar to those shown in Ref. [132]. There are, however, a few discrepancies: Here, a slightly lower value for the band denoted as $\mathrm{B}_1(4)$ was found (near the Γ point). The bands denoted E(10) are missing in Ref. [132]. Finally, the inspection of the field patterns suggests that the presented method is able to compute the modes with a higher accuracy [compare the noise-affected mode in Fig. 12(b) of Ref. [132] with the smooth mode $\mathrm{A}_2(8)$ of Fig. 4.3]. The good convergence and small relative error achieved in our computations give also good confidence in the accuracy of the method.

4.3.2 Triangular lattice of triangular cross section cylinders

The system analyzed here consists of a triangular lattice with lattice constant a. In each primitive cell there is one single cylinder whose cross section is an equilateral triangle of side $s = 0.8a$. The triangle sides are parallel to the primitive lattice vectors and the corners of the triangle are rounded with a radius $r_{\mathrm{c}} = 0.1a$ [Fig. 4.6(a) right inset]. The background is vacuum and the relative permittivity of the cylinders is given by Eq. (4.27). Again, only in-plane propagation is considered.

The space group of this crystal is $p3m1$, and its associated crystallographic point group is $3m$ (C_{3v} in Schönflies notation). For the Γ point in the 1^{st}BZ the group $\mathcal{G}_0(\Gamma)$ has two one-dimensional irreducible representations (A_1, A_2) and one two-dimensional irreducible representation (E). The band structure of this system is shown in Fig. 4.6 while the corresponding modal fields (for the Γ point) are plotted in Fig. 4.7. The bands are labeled with the same scheme that was used in subsection 4.3.1. The modes associated with plasmons of $n_{\mathrm{L}} = 2, 4, 8, 10, 14, \ldots$ are degenerated at the Γ point and those with $n_{\mathrm{L}} = 3k$, ($k \in \mathbb{N}$) are non-degenerated, as expected from the symmetry considerations explained in

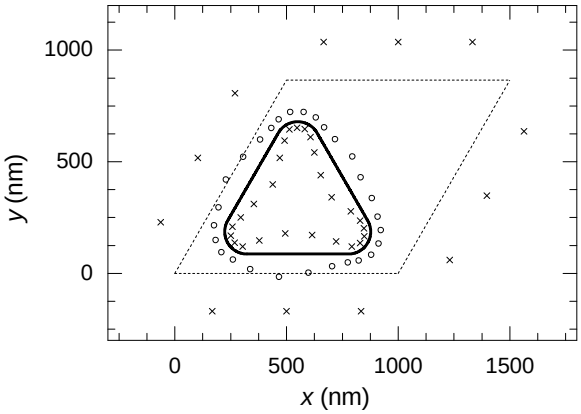

Fig. 4.8 Distribution of multipole expansions. The ∘'s are the locations of the multipole expansions modeling the fields inside of the triangle. The ×'s are the locations of the multipole expansions simulating the field inside the cell around the triangle. The locations were computed with the Automatic Multipole Setting procedure shown in chapter 3.

previous subsection (in contrast with the previous subsection, the symmetries of the isolated triangle and the crystal are the same and, therefore, the degeneracies are not changed). Observe that, as opposed to the rectangular lattice, this system presents a wide band gap between the first and second bands.

Due to the non-circularity of the cylinders, different basis functions as those in the example shown in previous subsection are needed. Here only multipole expansions are employed, whose location was determined with the Automatic Multipole Setting procedure presented in chapter 3. The expansions locations are represented in Fig. 4.8. The order of the multipole expansions was $n_{\mathrm{H,in}}$ for those inside and around the triangle and $n_{\mathrm{H,out}}$ for those around the primitive cell. For the lowest and highest bands $n_{\mathrm{H,in}} = 2$, $n_{\mathrm{H,out}} = 3$ were enough to achieve an accuracy of 0.1% averaged relative error (or better), while for the mPR bands with a large number of lobes $n_{\mathrm{H,in}} = 5$, $n_{\mathrm{H,out}} = 3$ were used.

The bands were determined by detecting the maxima of the residual $R(\omega)$. Since the group $\mathcal{G}_0(\mathrm{M}) = m$ (C_s in Schönflies notation) has only one-dimensional irreducible representations, the M point was chosen as initial $\mathbf{k}_{\mathrm{ini}}$ point for the EET.

4.4 Defects in photonic crystals

It is well known that the most salient feature of photonic crystals is the existence of frequency band gaps [146]. For frequencies belonging to the band gap, the eigenvalue problem of Eq. (4.19) (or the corresponding eigenvalue problem for the appropriate polarization) has no solution. This means that, no matter what the value of the $\mathbf{k}$ vector is, there are no Bloch modes $\Phi^{\mathbf{k}}(\mathbf{r})$ corresponding to those frequencies. Thus, the electromagnetic fields are excluded from the crystal. This fact can be exploited for many applications [138].

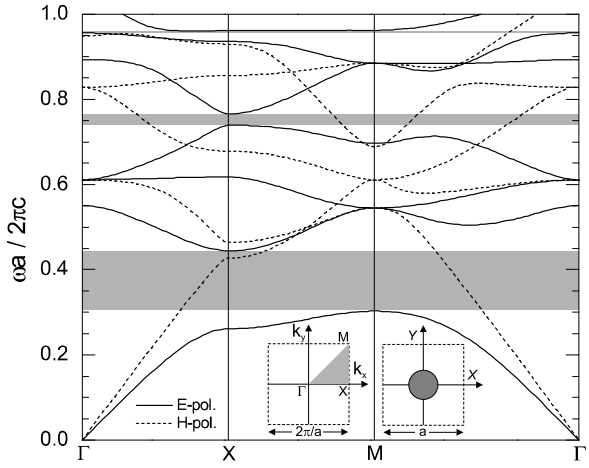

Fig. 4.9 Band structure of a perfectly periodic 2D photonic crystal (solid lines: E polarization; dashed lines: H polarization). There are three band gaps for E polarization, and they are shown as shaded regions (the upper gap is very narrow and is centered in $\omega a/(2\pi c) \approx 0.96$). The insets show the first Brillouin zone (left) and the primitive cell (right). The radii of the rods are $r = 0.18a$. The permittivity of the rods is $\varepsilon_r = 11.56$ and the background is vacuum.

Once the properties of a perfectly periodic photonic crystal are determined, the next level of complexity consists in the investigation of structures where this perfect translational symmetry is broken. The introduction of defects in the crystal disrupts the symmetry and may lead to the appearance of additional modal fields (*defect modes*) [147, 148]. The existence of defect modes allows the optical field entering inside the crystal.

The simplest defects are *point* [111, 149–152] and *line* [153–156] defects. In the case of a point defect, the periodicity of the crystal is broken at one single lattice site. This can be done, e.g., by means of a vacancy, interstitial, or substitutional defect. Point defects give rise to modal fields localized around the defect site, which behaves like a resonant cavity. Line defects can be constructed as a concatenation of point defects or by sliding two parts of the crystal with respect to each other (as in a stacking fault, for instance). These one-dimensional defects allow the propagation of energy along them, behaving, hence, as a waveguide. Other kinds of symmetry breakings which can be classified between point and line defects are the *coupled-cavity waveguides* (CCW) [157–160]. This type of impurity consists of a chain of more or less weakly coupled point defects. They permit the guiding of fields as the line defects do.

In order to study the mentioned defects, the *supercell* methodology [147, 161] can be employed. This technique, which is inherited from solid state physics, consists in defining a superlattice where the primitive (super)cell contains one single defect. The whole superlattice contains an array of defects (a 2D infinite array of cavities or an infinite set of parallel waveguides, for the cases of point

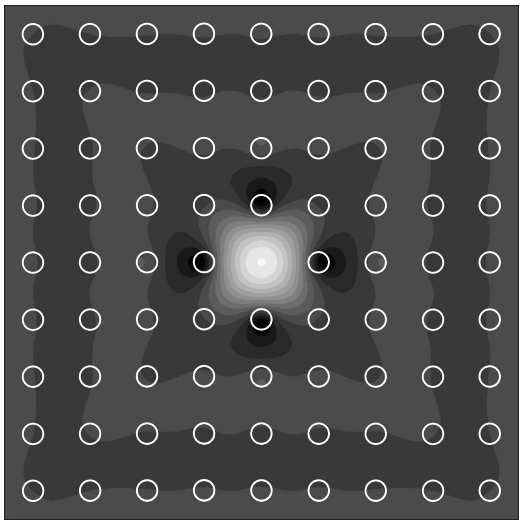

Fig. 4.10 Modal field of a point defect (vacancy). The plotted field is the electric field $E_z(\mathbf{r})$. The lattice constant is a and the radius of the cylinders is $r = 0.18a$ (the size of the supercell is $9a \times 9a$). The background is vacuum and the dielectric cylinders have relative permittivity $\varepsilon_r = 11.56$. The polarization is E.

and line defects, respectively). Nevertheless, when the supercell is large enough, the coupling between neighboring defects is negligible. In this way the properties of the isolated defects can be inferred.

The method presented in section 4.3 can be applied to the determination

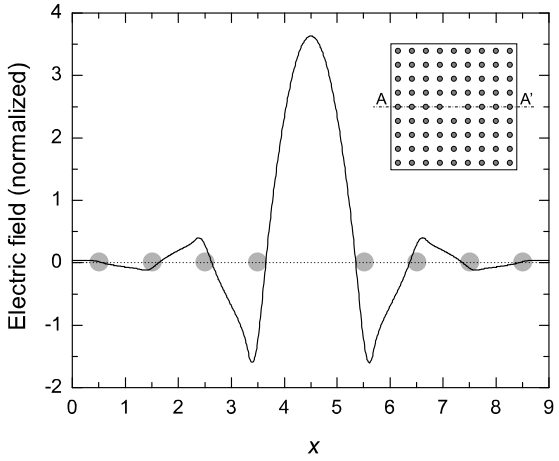

Fig. 4.11 Modal field $[E_z(\mathbf{r})]$ of a point defect (vacancy) along the horizontal line A–A′ dividing the supercell in two equal parts (see inset). The units in the horizontal axis are lattice constants a. Notice the negligible coupling with the neighboring supercells.

of defect bands. As examples, point and line defects are computed in subsections 4.4.1 and 4.4.2, respectively.

4.4.1 Point defect in square lattice

Here, the perfect crystal consists in a square lattice with lattice constant a. In each primitive cell there is one single cylinder with circular cross section of radius $r = 0.18a$. The background is vacuum and the relative permittivity of the rods is $\varepsilon_r = 11.56$. It is known that due to the non-connectedness of the dielectric elements in this configuration, this kind of crystal presents gaps only for E polarization [146]. This is in fact confirmed by the computations shown in Fig. 4.9.

If one single rod is removed (Fig. 4.10), a point defect of the acceptor type [147] is created. The corresponding defect mode is pushed out from the lower "valence" band. To compute the modes of this configuration, a supercell of 9×9 rods was chosen (to ensure that the coupling between defects is negligible). The procedure is analog to that explained in section 4.3. The excitation (a monopole) is located in a certain point inside the cavity. In this example only the Γ point ($\mathbf{k} = \mathbf{0}$) is of interest and no eigenvalue estimation technique is needed. However the EET could be employed to investigate the dependence of the modal field with the radius or permittivity of the defect. Figure 4.10 shows the field $E_z(\mathbf{r})$ of the defect mode. The cavity is single moded and the normalized frequency of the mode is $\omega a/(2\pi c) = 0.387$. Figure 4.11 shows the $E_z(\mathbf{r})$ field along the horizontal line dividing the supercell in two equal parts. The negligible field at the supercell boundaries suggests that no coupling among defects occurs.

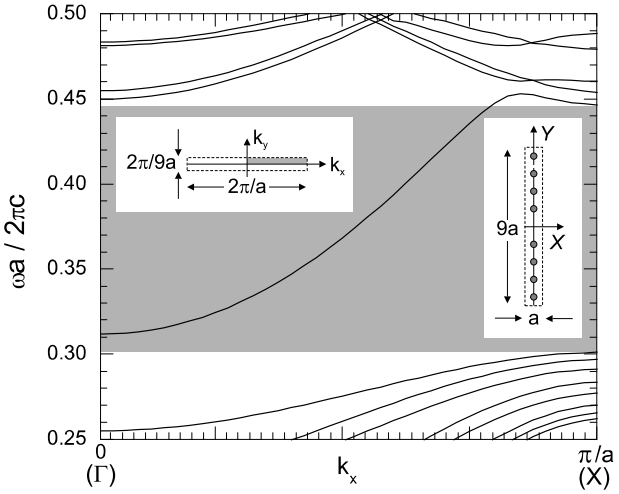

Fig. 4.12 Dispersion relation for the mode guided (E polarization) by a line of vacancies (Fig. 4.13). The insets show the first Brillouin zone (left) and the primitive cell (right). The shaded region represents the perfect crystal band gap.

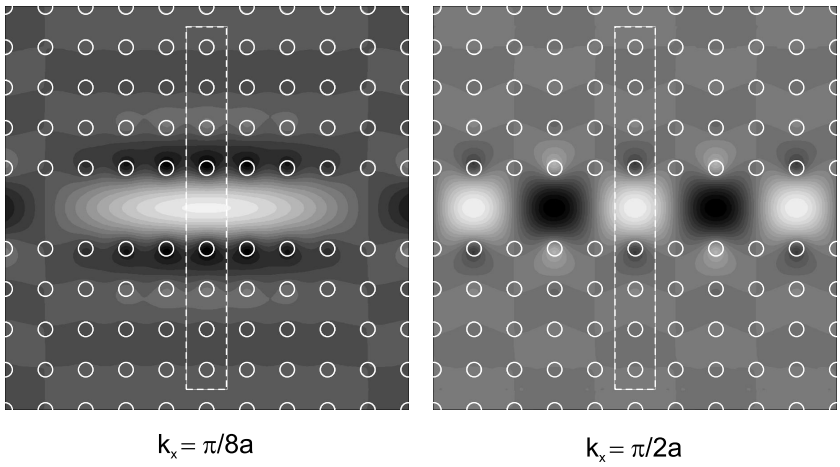

Fig. 4.13 Modes guided by a vacancy line defect. The plotted field is $E_z(\mathbf{r})$. The left plot represents the mode with $k_x = \pi/8a$ and the right one that with $k_x = \pi/2a$. The supercell employed in the calculation is shown as well (dashed box).

4.4.2 Line defects in square lattice

In this subsection, several kinds of line defects are addressed. The basis for the studied structures is the same perfect crystal as in subsection 4.4.1.

The best known line defect consists of a concatenation of vacancies [138, 146]. This kind of structure has been computed following the same principle as in subsection 4.4.1 for the point defect. Here, a supercell of 1×9 rods was chosen (Fig. 4.12, right inset). The band structure of this superlattice is shown in Fig. 4.12. If one compares the band structure of the perfect crystal (let us call it system I) in Fig. 4.9, with the band structure of the vacancy line defect (system II) in Fig. 4.12, two facts are observed: (i) system II has one additional band in the center of the band gap, and (ii) system II has more bands immediately above and below the band gap limits than system I. The band mentioned in (i) is the defect band. The fields and modal profiles corresponding to it (for two values of k_x) are plotted in Fig. 4.13 and Fig. 4.14, respectively. Note that for $k_x = \pi/8a$ the mode extends further in the lateral direction, as can be seen in Figs. 4.14(a, b). In fact Fig. 4.14(b) shows that, with this supercell size, there is still a very small coupling to the neighboring supercell. It is also interesting noticing that, for $k_x = \pi/2a$, the energy flows in the negative direction on the rods adjacent to the defect.

Regarding point (ii), the closely spaced bands immediately above and below the gap limits are in part due to the size of the primitive supercell, and in part due to the defect. If the *perfect* crystal is simulated with different unit cells (for instance the primitive cell $a \times a$, and the non-primitive unit cell $a \times 9a$), the same results have to be obtained. However, in the band structures, they appear in a different manner. The 1^{st}BZ corresponding to the primitive cell is a square of size $2\pi/a \times 2\pi/a$, whereas the 1^{st}BZ corresponding to the non-primitive unit

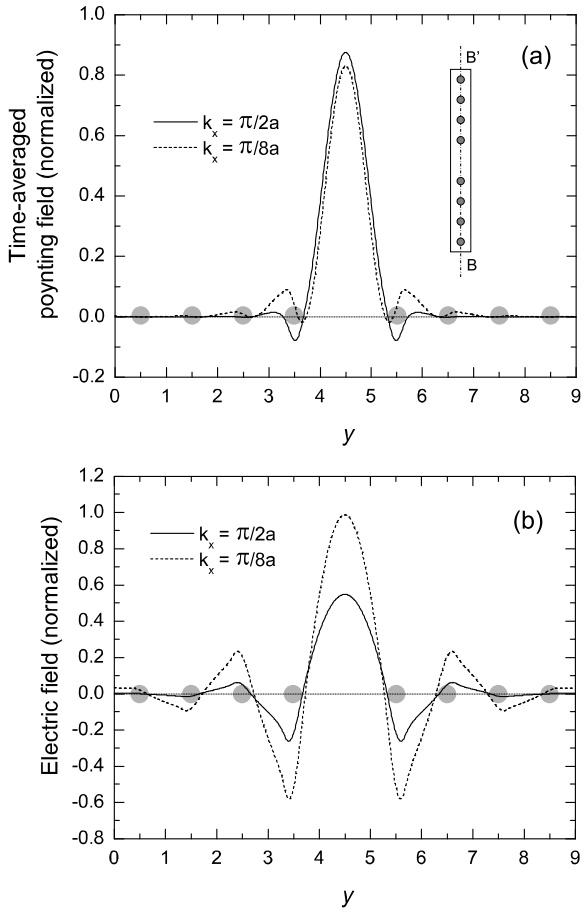

Fig. 4.14 Modal fields along the vertical line B–B′ dividing the supercell in two equal parts [see Fig.(a), inset]. The units in the horizontal axis are lattice constants a. (a) Power profile, (b) Electric field profile. All mode profiles are normalized in such a way that both modes ($k_x = \pi/8a$ and $k_x = \pi/2a$) carry the same power. The coupling with the neighboring supercells is very small. Note, however, that for $k_x = \pi/8a$ there is a small coupling with the neighboring supercells [(b), dashed lines].

cell is a rectangle of size $2\pi/a \times 2\pi/(9a)$. The band structure obtained with the non-primitive cell can be reconstructed from that of the primitive cell simply by folding the 1$^{\text{st}}$BZ corresponding to the primitive cell like an accordion on the 1$^{\text{st}}$BZ corresponding to the non-primitive unit cell (Fig. 4.15). By doing this folding, the bands above the 1$^{\text{st}}$BZ are warped in a complex way. For the non-primitive cell considered here ($a \times 9a$), each original band of the primitive system manifest itself along the ΓX direction as five bands in the band structure of the non-primitive system. In Fig. 4.12, there are eight bands immediately below the gap. This means that the three additional bands are due to the presence of the

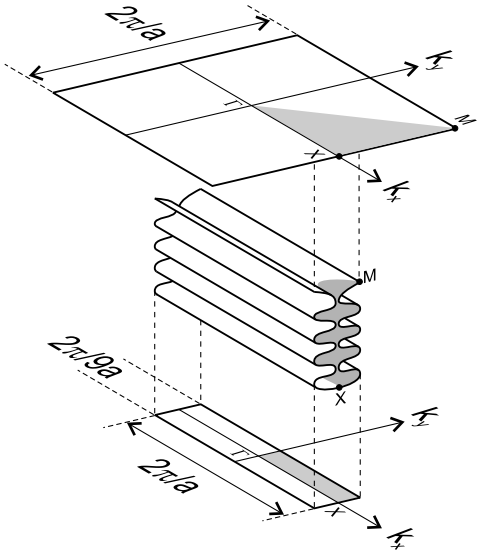

Fig. 4.15 Folding of the 1st BZ corresponding to the primitive cell, on the 1st BZ corresponding to the non-primitive cell. The accordion-like folded surface is the 1st BZ corresponding to the primitive cell (a square of size $2\pi/a \times 2\pi/a$).

defect.

The properties of the defect band can be varied by changing the width of the channel without rods in the crystal [153]. In this way it is possible to change the modal profile, the dispersion relation, or to design multimoded waveguides. The

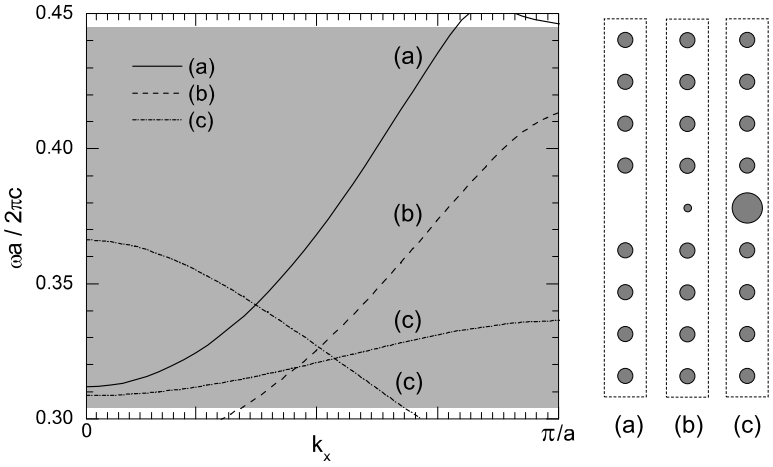

Fig. 4.16 Dispersion relations for various types of line defects: (a) line of vacancies, (b) line of substitutionals ($r = 0.09a$), (c) line of substitutionals ($r = 0.36a$). The shaded area represents the band gap of the perfect crystal.

possibility of positioning the defect band close to the gap center is also important, because defect modes with frequencies close to the gap limits have higher losses [116]. There are other ways of controlling the defect bands [113]. Instead of vacancy lines it is possible to employ lines of substitutionals, interstitials, etc. Figure 4.16 shows the dispersion relation for several such possibilities. Observe that the frequency of the vacancy line defect can be shifted downwards by adding thin dielectric columns [Fig. 4.16(b)]. Note that, by increasing the radius of the defect column, the multimoded regime is reached [Fig. 4.16(c)].

4.5 Propagation constants of guided modes

In this section a last application is presented where all the previously shown techniques are combined. Here, the propagation constants k_z of the modes in a waveguide with varying cross section are computed. The method for the computation of eigenvalues, the Automatic Multipole Setting procedure, and the eigenvalue estimation technique are all required in this example. For simplicity, a waveguide with perfectly conducting walls is considered.

The technique for the computation of eigenvalues presented in subsection 4.2.1 can be applied to the determination of the propagation constants of guided modes. Since the procedure is very similar to that shown in section 4.3, it is not explained in full detail again. The eigenvalue problem considered here is:

$$[(k_{\mathrm{T}}^n)^2 + \Delta_{\mathrm{T}}]\phi^n(\mathbf{r}) = 0, \tag{4.29}$$

with the corresponding Dirichlet or Neumann boundary conditions (for E or H polarization, respectively). The discrete index $n = 1, \ldots, \infty$ is a shorthand for the two indices needed to label the eigenmodes of this problem. The eigenvalues and eigenmodes of Eq. (4.29) are denoted by k_{T}^n and $\phi^n(\mathbf{r})$, respectively (k_{T}^n is the transverse wave number). For given angular frequency ω, each eigenvalue has an associated propagation constant $(k_z^n)^2 = \varepsilon\mu\omega^2 - (k_{\mathrm{T}}^n)^2$. Note that all but a finite number of modes are *evanescent* modes (with imaginary k_z^n). The associated scattering problem is:

$$[(\varepsilon\mu\omega^2 - k_z^2) + \Delta_{\mathrm{T}}]\phi(\mathbf{r}) = \phi_{\mathrm{exc}}(\mathbf{r}), \tag{4.30}$$

where both the excitation $\phi_{\mathrm{exc}}(\mathbf{r})$ and the solution $\phi(\mathbf{r})$ have a given propagation constant k_z. The appropriate Green's function to solve Eq. (4.30) is [analog to Eq. (4.22)]:

$$G_{k_z}(\mathbf{r}, \mathbf{r}') = \sum_{n=1}^{\infty} \frac{\phi^n(\mathbf{r})\phi^n(\mathbf{r}')^*}{(k_{\mathrm{T}})^2 - (k_{\mathrm{T}}^n)^2} = \sum_{n=1}^{\infty} \frac{\phi^n(\mathbf{r})\phi^n(\mathbf{r}')^*}{(k_z^n)^2 - k_z^2}. \tag{4.31}$$

The modes are excited with $\phi_{\mathrm{exc}}(\mathbf{r}) = \delta(\mathbf{r} - \mathbf{r}_0)$. The solution of the inhomogeneous equation is:

$$\phi(\mathbf{r}) = \sum_{n=1}^{\infty} \frac{\phi^n(\mathbf{r}_0)^*\phi^n(\mathbf{r})}{(k_z^n)^2 - k_z^2}. \tag{4.32}$$

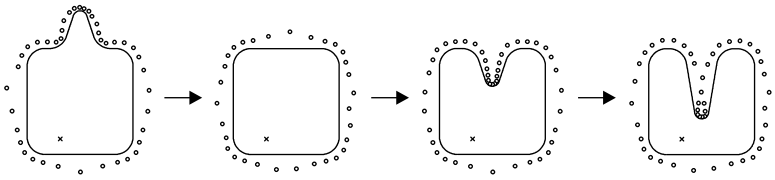

Fig. 4.17 Evolution of the geometry of the waveguide, and distribution of multipoles generated with the Automatic Multipole Setting procedure. The ∘'s represent the locations of the multipole expansions modeling the scattered field. The × is the position of the excitation $\phi_{\text{exc}}(\mathbf{r})$.

For $k_z^2 \to (k_z^n)^2$ the same kind of resonant behavior is observed as in section 4.3. Thus, in the same way as in that section, the modal fields and propagation constants can be determined. In the present context, k_z plays the same role as ω did in section 4.3. It is worth pointing out that the evanescent modes can also be found by searching along the imaginary axis ik_z.

In the application presented here, the propagation constants and modal fields of a waveguide are computed while its walls are deformed. The chosen geometry has no practical relevance but it allows one to grasp how a waveguide cross section could be optimized to achieve a given purpose.

The evolution of the geometry is shown in Fig. 4.17. The angular frequency is fixed to the value $\omega a/(2\pi c) = 0.8$, where a is the width of the waveguide. The medium inside the waveguide is vacuum. For each geometry in the sequence (90

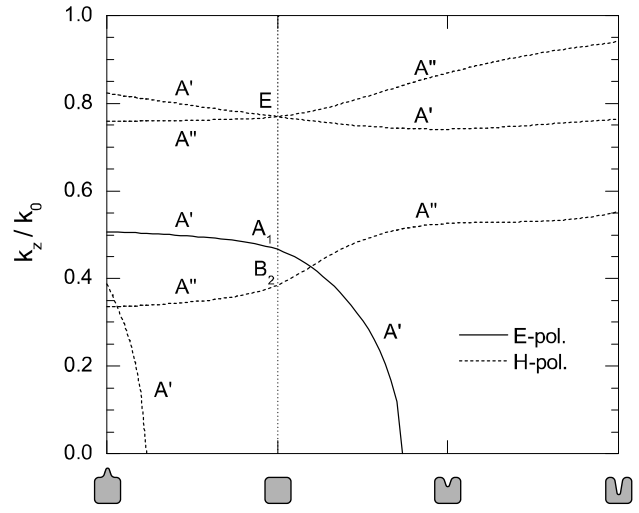

Fig. 4.18 Effective index (k_z/k_0) of the modes as a function of the shape of the waveguide (solid lines: E polarization; dashed lines: H polarization) ($k_0 = \omega/c$). The modes are labeled with the corresponding irreducible representations of the symmetry groups of the waveguides. The notation employed commonly for the modes corresponding to the square cross section is as follows: $\text{H}_{10} \oplus \text{H}_{01} \to \text{E}$, $\text{H}_{11} \to \text{B}_2$, $\text{E}_{11} \to \text{A}_1$.

intermediate geometries were computed) the multipole expansions have to be relocated (Fig. 4.17), and therefore an Automatic Multipole Setting procedure is mandatory. The variation of the propagation constants as the geometry changes is traced with the eigenvalue estimation technique (Fig. 4.18).

The modal fields are shown in Fig. 4.19 for the initial configuration, the square waveguide and the final configuration.

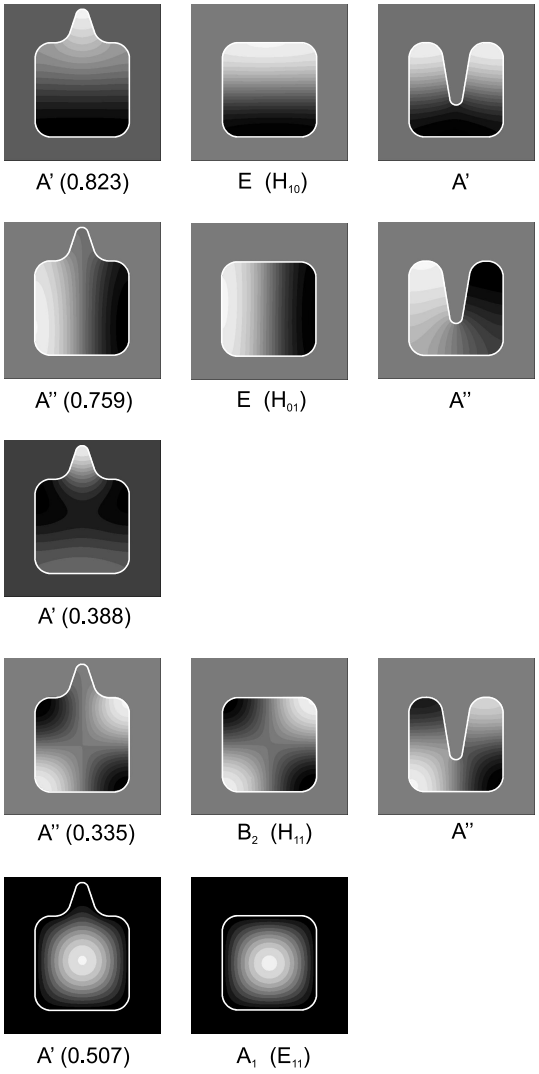

Fig. 4.19 Modal fields of the various modes. The first four rows (H-polarization) plot the $H_z(\mathbf{r})$ field and the last one (E-polarization) the $E_z(\mathbf{r})$ field. The modes are labeled with their irreducible representations. The numbers in the first column are the effective indices corresponding to the mode plotted above.

5

Modeling of photonic crystal waveguide discontinuities

5.1 Introduction

The eigenvalue computation method presented in the previous chapter allows one to study waveguiding structures. With the help of this method, the modal fields and propagation constants of conventional waveguides (i.e., waveguides with continuous translational invariance) can be determined and the defect bands of photonic crystal line defects can be analyzed. The analysis of waveguiding systems is important by itself, but in this chapter we go one step further and the following point of view is adopted: waveguides are considered as *given* constructive elements for the design of more complex devices. Indeed, many devices for the spatial or temporal modulation of the optical field are essentially waveguide discontinuities. A waveguide discontinuity consists of several input and output channels which are connected by an interaction region [5]. In this chapter photonic crystal waveguide discontinuities are analyzed, and in chapter 6 a non-periodic discontinuity in a conventional waveguide is modeled and optimized.

The simplest photonic crystal waveguide discontinuities are bends [16, 162, 163], branches [164–166], and intersections [114]. They are prerequisites for the development of photonic crystal optical circuits [167]. Much effort has been made recently for the analysis of wide angle bends [114] (to allow for ultra-small circuits) with the lowest possible reflection coefficient [16]. In this context, coupled-cavity waveguides seem to be quite promising [168]. The design of branching structures operating as power splitters [114, 164], and of waveguide intersections without crosstalk [169, 170] is also actively researched. Further structures (involving two different elements) are waveguides coupled to point defect microcavities [171–173], which can act as frequency discriminating systems [174]. Direct coupling of waveguides has been demonstrated for the design of directional couplers [12] and multiplexing systems [175], and indirect coupling via resonant cavities has been beautifully employed [176, 177] for the design of channel drop filters. A proposal for multichannel wavelength division multiplexing [178] has been presented as well. To conclude, two last applications are mentioned which concern the coupling to radiative modes (to be applied for the design of emitting antennas [117, 179] and detectors [180]) and the important issue of the in- and

outcoupling of the modes guided by a photonic crystal line defect to a conventional waveguide [181–183] (a sort of spot-size converter).

Up to now, the computation of photonic crystal waveguide discontinuities has been performed in time domain with FDTD (see for instance Ref. [16]), and in frequency domain with scattering matrix methods (see for instance Ref. [165]). However, as it will be explained in section 5.2, those methods present several disadvantages. Here, the goal is to present a general framework for the computation of photonic crystal waveguide discontinuities (in frequency domain) aiming at the three following aspects: (*i*) to avoid spurious reflections due to the impedance mismatching at the waveguide terminations, (*ii*) to characterize accurately the discontinuity, and (*iii*) to reduce the size of the computational domain.

After section 5.2, where the drawbacks of the commonly used methods are analyzed, the procedure developed here is presented and its features are explained in section 5.3. Then, in section 5.4, two applications are shown: a photonic crystal antenna and a T-junction presenting a filtering behavior.

5.2 Methods for the simulation of photonic crystal waveguide discontinuities

The FDTD method has been successfully applied to the computation of various photonic crystal waveguide discontinuities. Some prominent examples are Refs. [16, 164, 176, 182]. Here, the general advantages (such as easy modeling, etc.) and disadvantages (large memory requirements, etc.) of FDTD will not be discussed. Only those details specific for photonic crystal discontinuities are commented. The method is explained for the case of a T-junction discontinuity (Fig. 5.1) in Ref. [164]. It proceeds in the following way: (*i*) The input waveguide ① is excited with a pulse (typically originated from a dipole in front of the input waveguide entrance) containing the relevant frequencies. (*ii*) The pulse propagates along the input waveguide towards the T-junction. This waveguide has to be long enough to guarantee that the transients due to the coupling in the

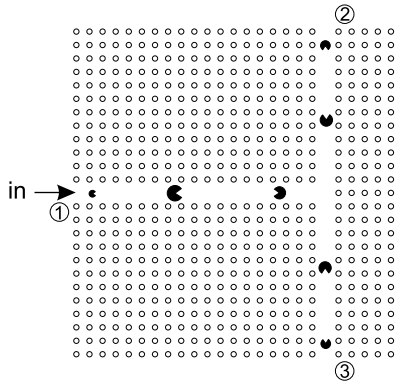

Fig. 5.1 T-junction in a photonic crystal. The discontinuity is fed from the left. The pacmen represent the incident, transmitted and reflected pulses at several different time instants (including the pulses reflected back at the crystal interfaces).

waveguide have decayed before the pulse arrives to the discontinuity. (*iii*) The incident, transmitted, and reflected pulses are recorded and Fourier-analyzed to determine the transmission [$T_2(\omega)$ and $T_3(\omega)$] and reflection [$R(\omega)$] coefficients as a function of frequency. Due to the finite size of the crystal, the pulses arriving to the waveguide terminations ①, ②, and ③ after interacting with the junction, are partially reflected back towards the junction. If these reflections are not carefully handled, they result in a complex mixture of the various transmitted and reflected pulses. To avoid this effect two mechanisms have been proposed. The first one [164] consists in defining very long arms for the T-junction. In this way, if the positions and the time windows where the pulses are recorded are properly chosen, the interferences between the various pulses are avoided. The second one makes use of sophisticated absorbing boundary conditions [184,185] to avoid spurious reflected pulses. The first approach requires huge computational domains (for instance Ref. [164] reports a computational domain of 140×180 crystal

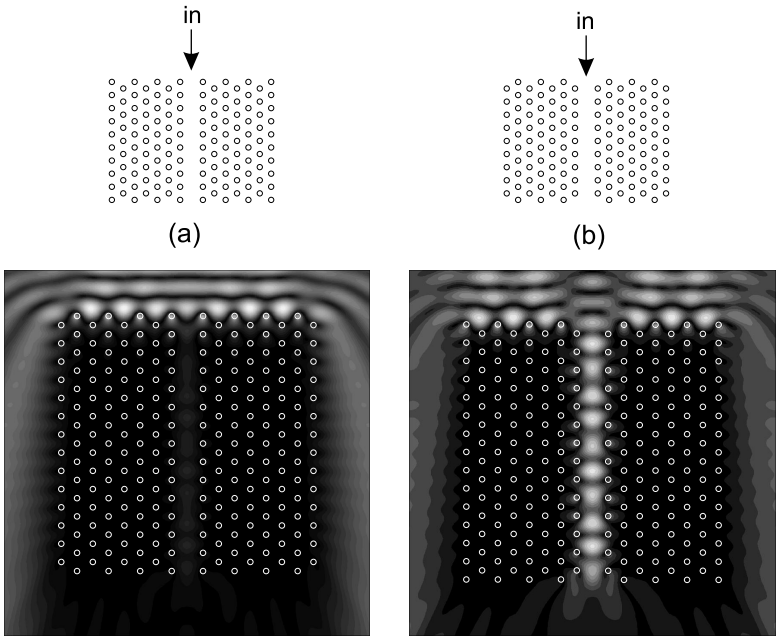

Fig. 5.2 Effect of "tapering" on the incoupling behavior. The crystal considered here is a triangular lattice of dielectric ($\varepsilon_r = 8.41$) circular cross section cylinders in vacuum. The radius of the cylinders is $r = 0.15a$, where a is the lattice constant (the band structure is plotted in Fig. 5.15). The waveguide is excited with a plane wave incident from the top (E polarization) with normalized frequency $\omega a/(2\pi c) = 0.473$ (which corresponds to an effective wavelength of $\lambda_{\text{eff}} \approx 2.8a$ [see Fig. 5.16(a)]). The only difference between (a) and (b) is the row where the crystal is terminated. Observe that in (b) a kind of ultrashort tapering occurs, which enhances the incoupling efficiency (the total power traveling downwards is approximately 26 times larger with taper than without it). The plotted field is the time averaged electric field.

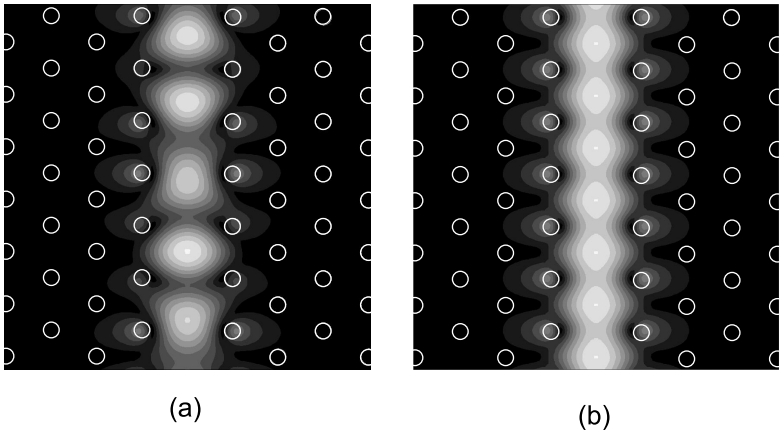

Fig. 5.3 Effect of the finite size of the crystal. The crystals in (a) and (b) have the same structure (described in Fig. 5.2). (a) Detail of Fig. 5.2(b) for the central 7 periods of the waveguide. (b) Modal field of an infinitely long waveguide computed with the supercell method. The pattern in (a) is due to the interference between the mode traveling downwards and the mode traveling upwards (reflected at the waveguide exit), whereas in (b) the field of the pure mode traveling downwards does not present such an effect. The plotted fields are the time averaged electric fields for $\omega a/(2\pi c) = 0.473$.

cells), whereas the second approach has to ensure that the perfectly matched layers perform equally well for all incidence directions and all k wave numbers included in the wave packet.

In the frequency domain, scattering matrix methods have also been applied for the analysis of photonic crystal discontinuities [149,165,175]. As with FDTD, finite size crystals are simulated. The field inside the scattering cylinders is modeled with Bessel functions whereas the field outside the cylinders is represented by multipolar functions and one additional excitation function (usually a plane wave). In this case Fourier transformations are obviously not required, but on the other hand –as several authors have mentioned [165,168]– it is very difficult to determine the value of $T_2(\omega)$, $T_3(\omega)$, and $R(\omega)$. The reason is again the reflection of the guided modes at the waveguides terminations: the field in each of the T-junction branches is a superposition of waves transmitted or reflected at the junction itself and reflected at the waveguide termination (at the crystal interface). As a consequence, it is not easy to characterize precisely the intrinsic behavior of the sole discontinuity.

The influence of the details of the waveguide termination and of the finite crystal size can be observed in the following two examples computed with MMP. In Fig. 5.2, it can be seen that the coupling to the waveguide is extremely sensitive to the fine details of the waveguide entrance: a very short tapering changes enormously the incoupling factor. The interference between the mode traveling downwards in the waveguide and the mode reflected back at the waveguide exit can be observed in Fig. 5.3(a). In this figure the field is compared with the

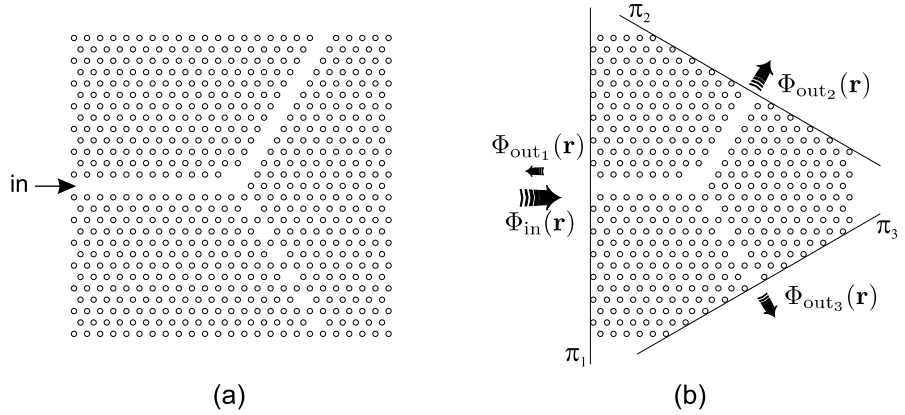

Fig. 5.4 (a) Typical photonic crystal discontinuity: three waveguides (two vacancy defect lines and a coupled-cavity waveguide) are connected in a central cavity. The Y-junction is fed from the left. (b) For the simulation, the crystal is cut by planes π_1, π_2, and π_3, and the fields arriving to those planes are matched to the modal fields [$\Phi_{\text{in}}(\mathbf{r})$, $\Phi_{\text{out}_1}(\mathbf{r})$, $\Phi_{\text{out}_2}(\mathbf{r})$, and $\Phi_{\text{out}_3}(\mathbf{r})$] of the corresponding infinitely long waveguides.

pure modal field traveling downwards (i.e., without reflected mode) [Fig. 5.3(b)] computed with the supercell approach (see subsection 4.4.2).

5.3 Impedance matching at waveguide terminations

5.3.1 General principle

From the discussion in the previous section, it is clear that the main difficulty stems from the impedance mismatching at the waveguide terminations. It is this mismatching what causes the undesired reflections. Therefore, the following procedure is proposed here (Fig. 5.4): The input and output waveguides are cut by planes (π_1, π_2, and π_3) at a certain distance from the discontinuity (this distance is discussed later). Then, the fields coming from the junction are matched at the

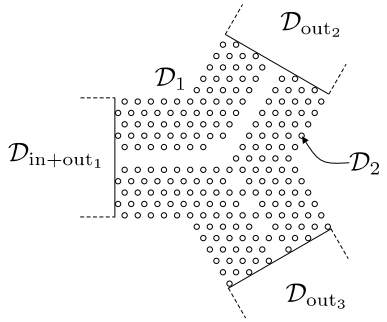

Fig. 5.5 MMP domains and boundaries employed for the simulation (the dashed lines are only a visual help, and they are not used for the modeling). $\mathcal{D}_1$ covers all the interaction region background, while $\mathcal{D}_2$ covers the inner part of all cylinders.

cut planes to the modal fields [$\Phi_{\text{in}}(\mathbf{r})$, $\Phi_{\text{out}_1}(\mathbf{r})$, $\Phi_{\text{out}_2}(\mathbf{r})$, and $\Phi_{\text{out}_3}(\mathbf{r})$] of the corresponding infinitely long waveguides. The procedure will be explained later in more detail, but let us anticipate that these modal fields of the input and output defect waveguides are computed with the supercell approach as shown in subsection 4.4.2.

The proposed idea is routinely used for many applications where discontinuities in *conventional* waveguides are present. In the context of the MMP method, it has been described for conventional metallic [186] (i.e., closed) and dielectric [187, 188] (i.e., open) waveguides. However the idea of defining input and output ports where the field is matched to the solution of the infinitely long waveguide, has not been employed –to the author's knowledge– for the computation of waveguides with *discrete* translational invariance. In comparison with the case of conventional waveguides, the application of the former idea to photonic crystals is more difficult. This is due to the fact that they possess only discrete translational symmetry, and to the fact that the energy waveguiding is not simple "index waveguiding", but the more complex "distributed Bragg waveguiding", which involves the scattering at a large number of elements. On the other hand, the analysis of open dielectric waveguide discontinuities can be more demanding, due to the coupling to the continuous set of radiative modes

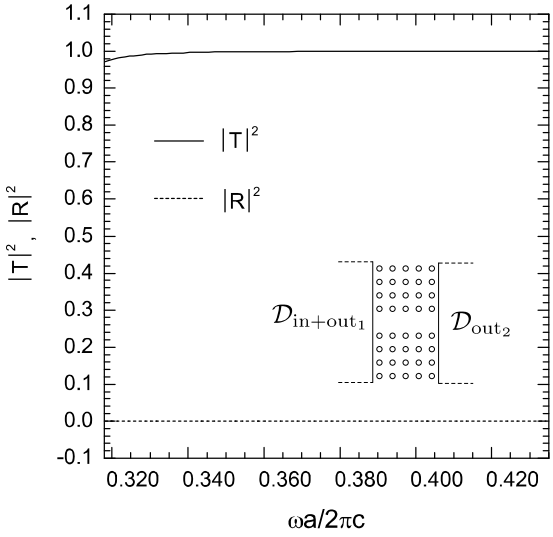

Fig. 5.6 Power transmission ($|T|^2$) and reflection ($|R|^2$) coefficients for a straight waveguide segment of length $5a$ (where a is the lattice constant, see inset). The photonic crystal considered here is a square lattice of circular cross section dielectric ($\varepsilon_r = 11.56$) cylinders ($r = 0.18a$) in vacuum. The polarization is E, and the waveguide is a vacancy defect line. The input and output modal fields were computed in subsection 4.4.2. Observe that the reflection coefficient is 0, and the transmission is 1 except for the low frequencies [corresponding to small wave vector numbers k and wide modal profiles, (see Fig. 4.14)]. The losses for small k are due to the thin waveguide walls.

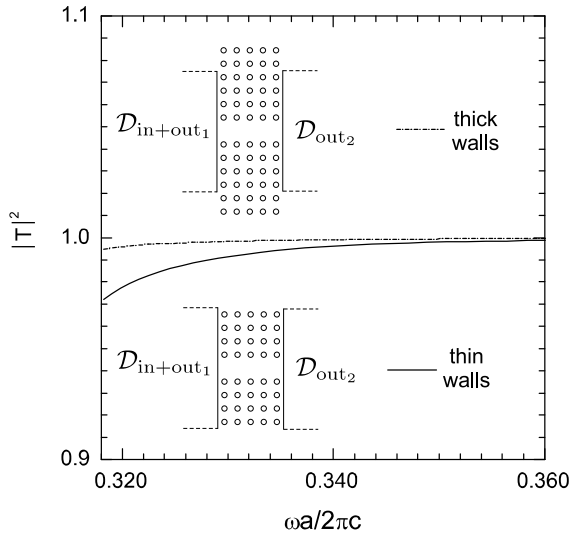

Fig. 5.7 Power transmission coefficients for a straight waveguide segment with photonic crystal walls of different thicknesses (see insets). The losses observed in Fig. 5.6 –for low frequencies– can be reduced by adding two further photonic crystal layers.

(see chapter 6). In this regard, photonic crystal waveguides are more akin to the metallic waveguides used in microwave applications, which strictly confine the electromagnetic field.

The main advantages of the idea presented above are the following: (*i*) Since a perfect matching of the guided modes is achieved, no spurious reflections occur at π_1, π_2, and π_3, and it is possible to characterize the properties of the waveguide discontinuity alone. (*ii*) Complex (and not necessarily reliable) absorbing boundary conditions are avoided. (*iii*) No Fourier transformation is needed. (*iv*) The computational domain is reduced to the minimum possible size.

The procedure is now explained in detail. Figure 5.5 displays the domains and boundaries employed for the MMP simulation. $\mathcal{D}_1$ and $\mathcal{D}_2$ are the domains modeling the "interaction" region. The background is assigned to $\mathcal{D}_1$ while the cylinders are assigned to $\mathcal{D}_2$. The boundaries $\partial\mathcal{D}_{12}$ are the cylinders circumferences. There are three other domains ($\mathcal{D}_{\mathrm{in+out}_1}$, $\mathcal{D}_{\mathrm{out}_2}$, and $\mathcal{D}_{\mathrm{out}_3}$) corresponding to the input and output channels. Domains $\mathcal{D}_1$ and $\mathcal{D}_{\mathrm{in+out}_1}$, $\mathcal{D}_{\mathrm{out}_2}$, $\mathcal{D}_{\mathrm{out}_3}$ are separated by three fictitious boundaries (along the planes π_1, π_2, and π_3). The appropriate widths of the photonic crystal around the waveguides and the distances between discontinuity and in/out ports will be discussed later. The fields in the different domains are modeled in the following way. In $\mathcal{D}_1$ the field is represented by a multipole expansion at the center of each cylinder plus additional multipoles *inside* each of the in/out ports (along the three corresponding boundaries). In $\mathcal{D}_2$ the field is modeled with Bessel expansions (one at the center of each cylinder; each such Bessel expansion represents the field only inside the corresponding cylinder). In each output port ($\mathcal{D}_{\mathrm{out}_2}$ and $\mathcal{D}_{\mathrm{out}_3}$) the field is modeled

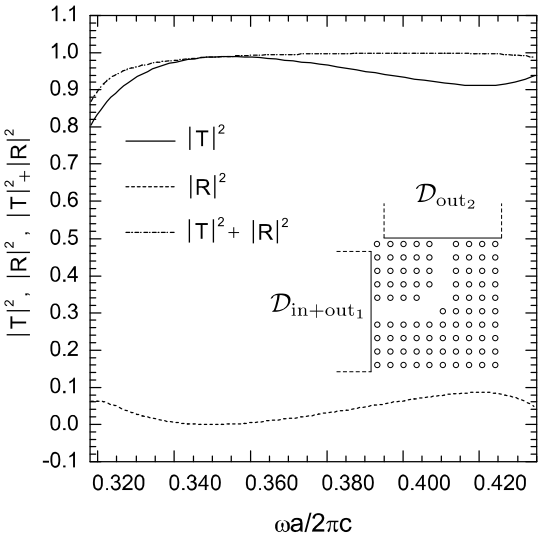

Fig. 5.8 Power transmission ($|T|^2$) and reflection ($|R|^2$) coefficients for a 90° bend with arms of approximate length of $4a$ (where a is the lattice constant, see inset). The photonic crystal considered here is the same as in Fig. 5.6. Observe that the total power is not well conserved for low and for high frequencies. For low frequencies (corresponding to long effective wavelengths) the bend arms are too short and the spatial transients reach the in/out ports. For high frequencies the mode frequency is very close to the band edge and the mode is less well confined in the defect waveguide.

with a connection (see subsection 2.2.7), which contains the mode transmitted toward that port. Finally, in domain $\mathcal{D}_{\text{in+out}_1}$ the field is modeled with two connections to represent the incident and reflected modes, respectively. In the case that some waveguides are multimoded, additional connections are employed to represent the various modes. Each modal field serving as input [$\Phi_{\text{in}}(\mathbf{r})$] or output [$\Phi_{\text{out}_1}(\mathbf{r})$, $\Phi_{\text{out}_2}(\mathbf{r})$, and $\Phi_{\text{out}_3}(\mathbf{r})$] mode, is computed as it was explained in subsection 4.4.2 and then packaged in one connection.

It is important to realize that, since in the transition from the interaction region to the ports there is no impedance mismatch, the transmitted modes exiting towards $\mathcal{D}_{\text{out}_2}$ and $\mathcal{D}_{\text{out}_3}$, and the reflected mode exiting towards $\mathcal{D}_{\text{in+out}_1}$ are not reflected at the fictitious boundaries separating the in/out ports from the interaction region. This means that when the input mode has amplitude 1, the (complex) amplitudes of each connection –representing the output modes– are precisely the transmission [$T_2(\omega)$, $T_3(\omega)$] and reflection [$R(\omega)$] coefficients of the discontinuity.

5.3.2 Computational details and assessment of the method

Several additional details need to be commented. In what concerns the definition of the domains three essential points are: (*i*) the number of photonic crystal layers around the defect waveguides and discontinuity center, (*ii*) the distances from the in/out ports fictitious boundaries to the discontinuity center, and (*iii*) the

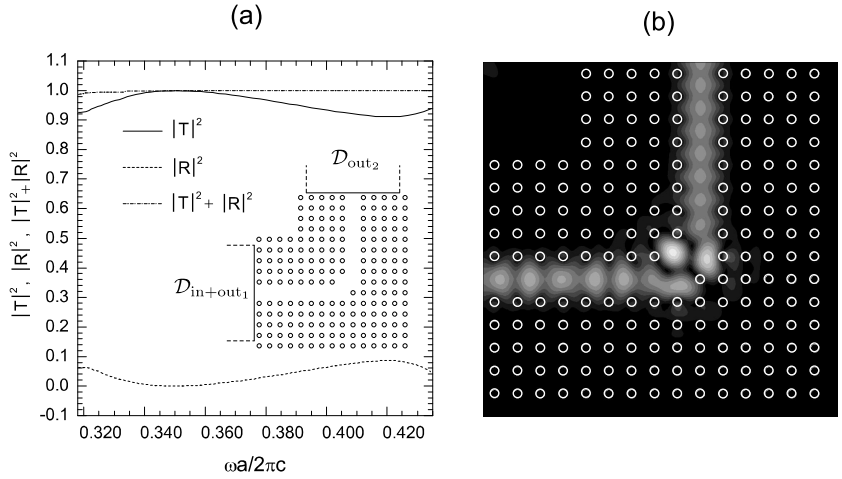

Fig. 5.9 (a) Power transmission ($|T|^2$) and reflection ($|R|^2$) coefficients for a 90° bend (the same as in Fig. 5.8) with arms of an approximate length of $7.5a$ (where a is the lattice constant, see inset). Observe that the total power is now conserved for $\omega a/(2\pi c) > 0.325$. (b) Time averaged electric field for $\omega a/(2\pi c) = 0.435$. In the horizontal branch the interference between the incoming and reflected modes can be observed, whereas in the vertical branch only a pure transmitted mode propagates.

lengths of these fictitious boundaries.

The number of layers around the waveguide mentioned in (*i*) has to guarantee a negligible leakage of the guided modes in its propagation through the discontinuity. On the other hand this number should be kept as small as possible to reduce the computational effort. In Fig. 5.5 the thickness of the photonic crystal surrounding the waveguide is equal to the length of the fictitious boundaries, but sometimes thicker photonic crystal walls are required (for instance, when high quality factor resonant cavities at the discontinuity have to be modeled). As a first assessment of the method, Fig. 5.6 displays the power transmission ($|T|^2$) and reflection ($|R|^2$) coefficients for a waveguide without discontinuity. The reflection is 0, and the transmission is 1 except for low frequencies corresponding to small wave numbers k (see Fig. 4.12). This loss of power can be diminished by adding more photonic crystal layers, as it is shown in Fig. 5.7: the addition of two more rows in the model reduces the leakage for low frequencies[1].

The distances between the ports and the discontinuity center mentioned in (*ii*) should be as short as possible to reduce the numerical effort. However, they should be long enough to guarantee that the fields arriving at the fictitious boundaries are pure guided modes and the evanescent terms have already faded away. It is worth noting that these distances depend on the effective wavelength of the guided mode and, therefore, they have to be longer for small k wave number. This is shown in Figs. 5.8 and 5.9(a), which display the power transmission and

[1]Incidentally, such a computation can be used to estimate the loss per unit length of a waveguide with walls of a given number of photonic crystal layers.

reflection coefficients due to a 90° bend in a vacancy line defect. In Fig. 5.8 the power is not conserved –for low frequencies– because the lengths of the bend arms are too short for the corresponding effective wavelengths and the evanescent transients reach the in/out ports. Note that the conservation of energy deteriorates for $\omega a/(2\pi c) < 0.370$, which corresponds to (see Fig. 4.12) $k_x \approx 0.5\pi/a$, i.e., an effective wavelength of $\lambda_{\text{eff}} = 2\pi/k_x \approx 4a$. This is approximately the length of the bend arms employed in the simulation (see Fig. 5.8, inset). Increasing the length of the arms, the frequency range for which the model works properly is extended to lower frequencies [Fig. 5.9(a)]. As a rule, the length of the waveguide arms should be at least one effective wavelength of the guided mode for the operating frequency. The same structure was computed with FDTD [16] using a simulation domain 50 times larger than the domain employed in Fig. 5.9[2]. The small inaccuracy observed in Fig. 5.8 in the energy conservation –for high frequencies– is due to the fact that those frequencies are very close to the band gap edge and the leakage is higher. This can be avoided by addition of one layer of photonic crystal [see Fig. 5.9(a)]. The inaccuracy in the power conservation becomes then smaller than 0.2% of the input power. The field in the bend is plotted in Fig. 5.9(b).

Finally, the lengths of the ports fictitious boundaries mentioned in (*iii*) should guarantee that the guided mode amplitude is negligible at both ends of the fictitious boundary. Usually this length is the same as that of the supercell employed to determine the modal guided fields. Note again (see for instance Fig. 4.14) that the modes penetrate deeper in the photonic crystal for small k, which means that larger supercells are required, and correspondingly longer fictitious boundaries.

Regarding the expansions modeling the fields, one should pay attention to the following points. (*i′*) In this chapter only circular cross section cylinders have been considered. For this case, one Bessel expansion plus one multipole expansion both located at each cylinder center are probably optimal. For other geometries more expansions may be needed. (*ii′*) The multipole expansions located inside the in/out ports and radiating towards $\mathcal{D}_1$, are positioned equidistant from each other and from the corresponding fictitious boundaries. (*iii′*) The maximum order of the expansion mentioned in the two previous points depends on the desired accuracy. As it could be expected, those expansions close to the defect waveguides and to the central cavity are more important and should usually have a higher order.

5.4 Applications

5.4.1 Coupling to radiative modes

The discontinuities considered in subsection 5.3.2 were closed, i.e., the whole structure is surrounded by photonic crystal layers (infinitely thick in the ideal

[2]It is worth comparing the results shown in Fig. 5.9 with those obtained with FDTD (Ref. [16], Fig. 2). The method presented here uses a simulation domain of 15×15 lattice constants, whereas with FDTD the domain size was 100×120 lattice constants. Here, the results deteriorate for $\omega a/(2\pi c) < 0.325$, whereas with FDTD spurious oscillations occur for $\omega a/(2\pi c) < 0.360$. Despite the large simulation domain employed there, transmission coefficients up to 1.20 for low wave numbers were displayed in Ref. [16], Fig. 2.

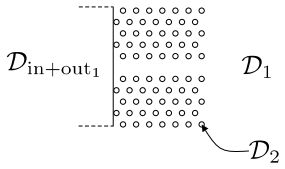

Fig. 5.10 MMP domains and boundaries employed for the simulation of the transition from waveguide to free space (the dashed lines are only a visual help, and they are not used for the modeling). $\mathcal{D}_1$ covers the whole background (inside and outside the photonic crystal), while $\mathcal{D}_2$ covers the inner part of all cylinders.

case) and therefore no energy should leak out of the system. Nevertheless, the generalization to open systems is not conceptually difficult, although it is more demanding from the modeling point of view. In this subsection the coupling from the waveguide to free space and the effects of the termination of photonic crystal waveguides at the crystal interface are considered. It has been already mentioned (Fig. 5.2) that the fine details of the waveguide termination have a crucial importance in the coupling of the guided modes to the radiation modes. However, with conventional scattering matrix computations this effect could not be quantified, because the mode arriving at the interface (from the source) and the mode reflected at the interface back towards the source are mixed.

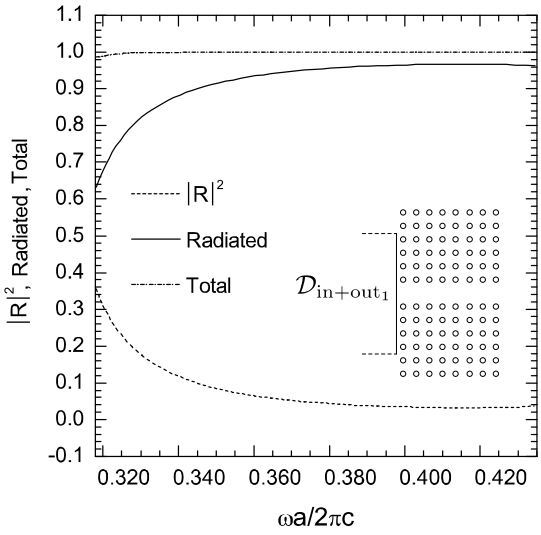

Fig. 5.11 Reflected ($|R|^2$), radiated, and total power for a transition between a defect waveguide and free space. The photonic crystal considered here is the same as in Fig. 5.6. The length of the waveguide before the discontinuity is approximately $7.5a$. That means that the model should deteriorate for $\omega a/(2\pi c) < 0.325$ (see Fig. 4.12), as it is indeed observed in the figure.

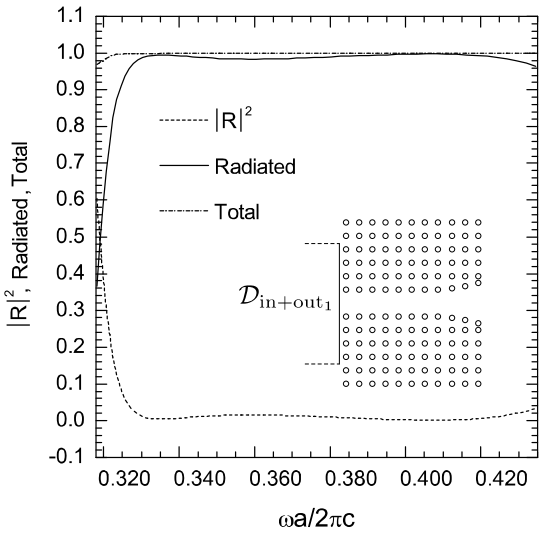

Fig. 5.12 Reflected ($|R|^2$), radiated, and total power for a transition between a defect waveguide and free space. The photonic crystal considered here is the same as in Fig. 5.6. The tapering decreases significantly the reflection coefficient. Due to the short length of the waveguide tract, the simulation results are not correct for low frequencies (as it was discussed in subsection 5.3.2).

The method described in section 5.3 can be applied to this kind of discontinuities between waveguide and free space. Here, only one port for guided modes ($\mathcal{D}_{\text{in+out}_1}$) is needed (Fig. 5.10), whereas the radiation couples out in domain $\mathcal{D}_1$. Except under especial conditions (see the end of this subsection) the elements described in section 5.3 are enough for the modeling of this type of discontinuity.

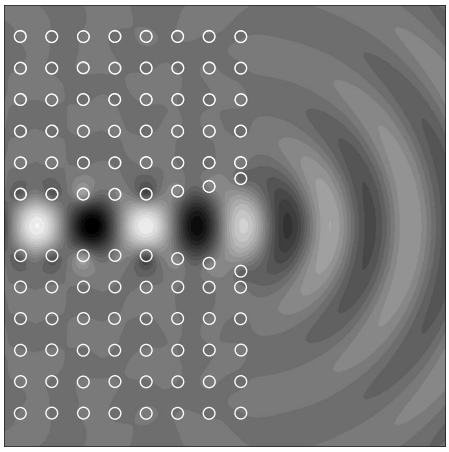

Fig. 5.13 Electric field amplitude radiated by the tapered waveguide. The normalized frequency is $\omega a/(2\pi c) = 0.395$.

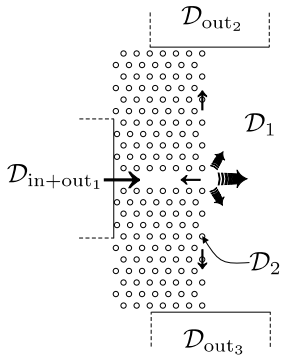

Fig. 5.14 MMP domains and boundaries required for the simulation of the transition from waveguide to free space when surface modes can be excited (the dashed lines are only a visual help, and they are not used for the modeling). $\mathcal{D}_{\text{out}_2}$ and $\mathcal{D}_{\text{out}_3}$ are output ports for the surface modes.

The number of photonic crystal layers around the waveguide has to be enough to ensure a good modal confinement, and additionally it has to be such that the outgoing field does not "feel" the finite lateral size of the crystal. It is maybe useful to mention that the field in domain $\mathcal{D}_1$ is expanded exactly in the same way as in section 5.3: one multipole expansion inside each cylinder plus a set of multipole expansions inside $\mathcal{D}_{\text{in+out}_1}$.

Figures 5.11 and 5.12 show the reflected ($|R|^2$), radiated, and total power (reflected plus radiated) for two different waveguide terminations (see insets). Observe the good energy conservation except for low frequencies (this effect has already been discussed in subsection 5.3.2): to obtain correct results for low frequencies, a longer piece of waveguide has to be simulated. It is also important noticing that the reflection coefficient has been significantly decreased in most of the frequency range by introduction of a short tapering (Fig. 5.12). The electric field in the structure is plotted in Fig. 5.13

One last comment concerns the required thickness of the photonic crystal waveguide walls. It is known that surface modes may be supported at the interface between the photonic crystal and the free space [118, 189, 190]: depending on the termination of the mentioned interface, these modes may exist for certain frequency ranges. If this is the case, the outgoing waveguide mode may excite surface modes when it arrives at the waveguide termination. When these surface modes arrive to the right upper and lower corners of the model crystal (see Fig. 5.11, inset) they will be partially reflected back towards the waveguide entrance and partially radiated, giving rise to spurious effects. In other words, the outgoing field will feel the finite lateral size of the crystal independently of the thickness of the waveguide walls. It has been reported [117] that the excitation of surface modes can significantly change the pattern of the radiation emitted by the waveguide. The existence of surface modes may be taken into account by introduction of two additional ports for these modes, as it is depicted in Fig. 5.14 (although this was not necessary in the applications considered above).

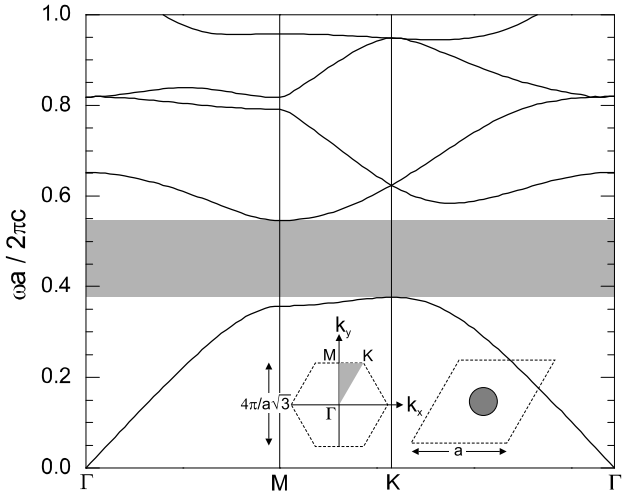

Fig. 5.15 Band structure of a triangular lattice of dielectric ($\varepsilon_r = 8.41$) circular cross section cylinders in vacuum. The radius of the cylinders is $r = 0.15a$, where a is the lattice constant (E polarization). The insets show the first Brillouin zone (left) and the primitive cell (right).

5.4.2 Filtering T-junction

In this subsection a complex T-junction discontinuity is analyzed. The underlying photonic crystal used here is a triangular lattice of dielectric cylinders in air[3], and it has the band structure shown in Fig. 5.15. The diagram shows a wide band gap between the first and second bands.

Many different line defects can be defined in this crystal. Some of them (with the corresponding dispersion relations) are displayed in Fig. 5.16. Usually, line defects preserving the symmetry of the crystal [such as (a) and (b) in Fig. 5.16] are preferred [116], and most studies in the literature focus on this type of waveguides. The reason is that, since the underlying global lattice is not disrupted, the design of complex photonic circuits is –in principle– easier. However, other kind of waveguides which disrupt the underlying lattice have been studied [153], e.g., stacking faults. Two examples of such defects are shown in Fig. 5.16 [(c) and (d)]. The modes labeled (a) and (c) present a very similar behavior except close to the Brillouin zone edge: the (c) mode is degenerated whereas (a) is not (this effect was also found in Ref. [153]). Here, it will be shown that stacking faults can be used to design devices with interesting functionalities.

The discontinuity considered in this subsection is shown in Fig. 5.17. The figure caption describes in detail how the T-junction is constructed: two waveguides are created by sliding a piece of the photonic crystal, whereas the third one is built by removing a row of cylinders. As a by-product of this construction,

[3]It is known that the inverse structure (air cylinders in a dielectric background) may support a complete band gap for both polarizations. Here only the E polarization is considered, and therefore the employed crystal is appropriate.

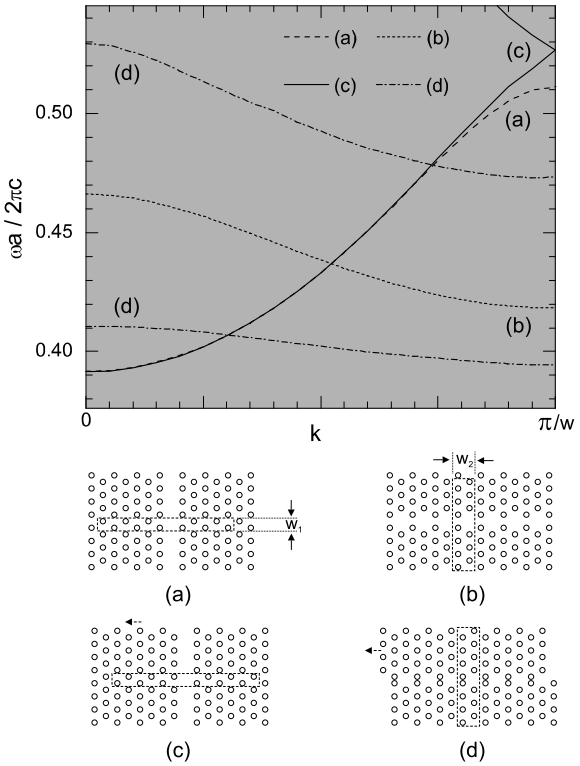

Fig. 5.16 Dispersion relation for several defect waveguides in the crystal described in Fig. 5.15 (note that the horizontal axis is normalized using the width w of the supercell, which is not the same for all waveguides). (a) and (b) are vacancy line defects obtained by removing one column and one row of cylinders, respectively [in fact, (b) behaves like a coupled-cavity waveguide]. (c) and (d) are obtained by sliding two parts of the crystal with respect to each other a distance $a\sqrt{3}/2$. In (c) a channel waveguide with dispersion similar to (a) is obtained whereas in (d) a coupled-cavity waveguide (2-moded in the whole k range, see also Fig. 5.18) results.

a double cavity appears at the T-junction center. From the figure, it is intuitive that the right and left waveguides will behave as coupled-cavity waveguides. This kind of waveguides presents flattened bands, and therefore its bandwidth is small. The bandwidth depends on the coupling between the cavities, becoming smaller for weak coupling [159, 168]. Since the cavities constituting the right waveguide (b) are larger than those of the left waveguide (d), the defect band of the right one will have lower frequencies than that of the left one. In addition, the vertical channel (c) will support modes for a larger range of frequencies. If the frequency range of (c) overlaps with those of (b) and (d), the structure could be used to implement a T-junction, which additionally filters one low frequency towards the right and one high frequency towards the left. In fact, in Fig. 5.16,

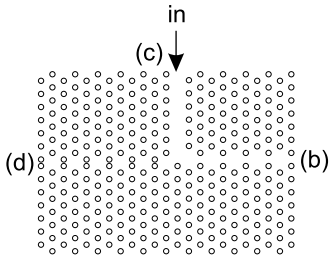

Fig. 5.17 T-junction with filtering behavior. The structure is based on the perfect crystal described in Fig. 5.15. Two waveguides [of types (c) and (d), see Fig. 5.16] are obtained by sliding the upper left block of the crystal a distance $a\sqrt{3}/2$. The third waveguide [of type (b)] is a coupled-cavity waveguide obtained by removing a row of adjacent cylinders. At the intersection a cavity is formed, which consists of two smaller subcavities (of similar sizes as those at the left and right of the junction).

precisely this kind of desired overlapping band behavior is observed[4]. From the analysis of the dispersion curves in Fig. 5.16 it is clear that for the frequency $\omega a/(2\pi c) \approx 0.437$ [resp. $\omega a/(2\pi c) \approx 0.478$] transmission from the top to the right (resp. left) waveguide should be possible. In the intermediate frequency range [for $\omega a/(2\pi c) \approx 0.470$] none of the horizontal waveguides supports a mode and therefore total reflection is expected.

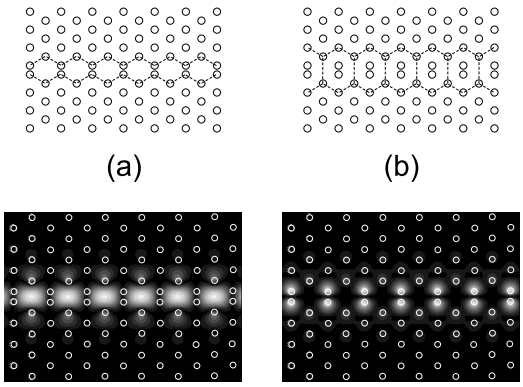

Fig. 5.18 Coupled-cavity modes of the waveguide shown in Fig. 5.16(d). The dashed lines show the cavities involved for each mode. At the bottom the time averaged electric field is plotted for each mode. (a) is the high frequency mode [for $\omega a/(2\pi c) = 0.478$] and (b) the low frequency one [for $\omega a/(2\pi c) = 0.406$]. In (b) the system behaves like a chain of cavities loaded with a dielectric. Observe that the overlap of the field in contiguous cavities is smaller in (b) than in (a). This implies a weaker coupling and therefore a smaller bandwidth (as it is indeed observed in Fig. 5.16).

[4]Surprisingly, it turned out that waveguide (d) supports two modes. The inspection of the modal fields demonstrate that they correspond to two different cavity modes (Fig. 5.18).

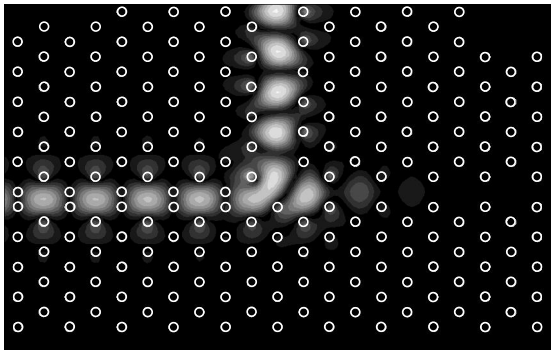

$\omega a/(2\pi c) = 0.478$

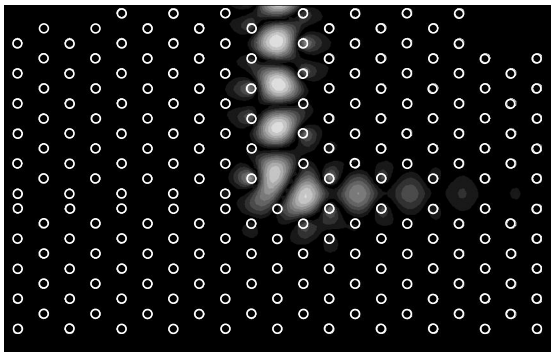

$\omega a/(2\pi c) = 0.470$

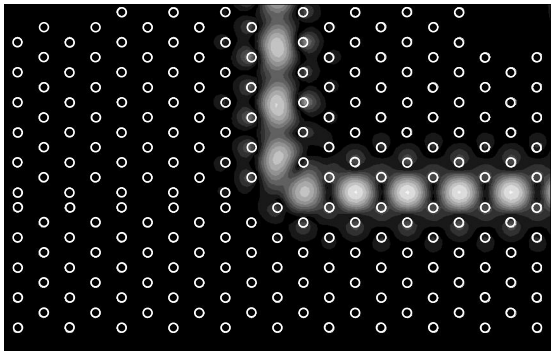

$\omega a/(2\pi c) = 0.437$

Fig. 5.19 Filtering behavior of the T-junction structure shown in Fig. 5.17. The plotted field is the time averaged electric field.

For the simulation of this device, the ideas explained in section 5.3 were followed. There are only a few new ingredients to consider: (*i*) Each of the waveguides joining at the T-junction central cavity supports a different mode and, therefore, the corresponding different fields have to be matched at each in/out port. (*ii*) Since the slope of the dispersion relation is negative for the coupled-cavity modes, the group velocity is negative. The sign of the wave number k has to be chosen appropriately in order to obtain the correct direction for the energy propagation. (*iii*) The vertical waveguide supports a guided mode for all considered frequencies, but this is not the case for the horizontal waveguides. This means that for certain frequencies, no propagating mode is available to match the field at the right or at the left port. For those frequencies which do not support a mode either to the right or to the left, the corresponding branch of the T-junction is left "open", i.e., no output port is attached at the end of the waveguide (taking care that the arm is long enough so that no power leaks out).

As the previous considerations predicted, Fig. 5.19 shows the filtering behavior of the T-junction. The power transmitted to the corresponding branches for the considered frequencies is 35% (towards the left, for the high frequency) and 87% (towards the right for the low one). To achieve a higher transmission for both frequencies, the central cavity has to be redesigned, in such a way that it possesses two modes, and the coupling coefficients of those modes with the adjacent waveguides are appropriate [164, 177, 191–193]. The idea is to find a cavity with the following properties: (*i*) The right (resp. left) subcavity has the same resonant frequency as the right (resp. left) waveguide. (*ii*) The coupling factor of the right (resp. left) subcavity to the left (resp. right) waveguide is negligible. (*iii*) The decay rates of the mode sustained by the right (resp. left) subcavity to the upper and to the right (resp. left) waveguides are the same. Points (*i*) and (*ii*) enforce the filtering behavior, whereas (*iii*) minimizes the reflections back towards the input waveguide (for the chosen resonant frequencies). The optimization of the cavity in order to satisfy the previous requirements will not be presented here. Nevertheless, to make it plausible, the following example is

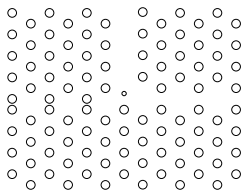

Fig. 5.20 Improved T-junction with filtering behavior. The structure is the same as described in Fig. 5.17 with addition of one further rod at the junction. The radius of this rod is $r' = r/2$ (where r is the radius of the other rods), and it is positioned at a distance $3a/4$ from the rod immediately below. By choosing the position and radius of this rod, the modes of the central cavity can be appropriately manipulated. The domain employed for the simulations has a size of 10 lattice constants in the vertical direction. In the horizontal direction the domain contains the central $\infty-$shaped cavity plus 4 cavities at each side of it.

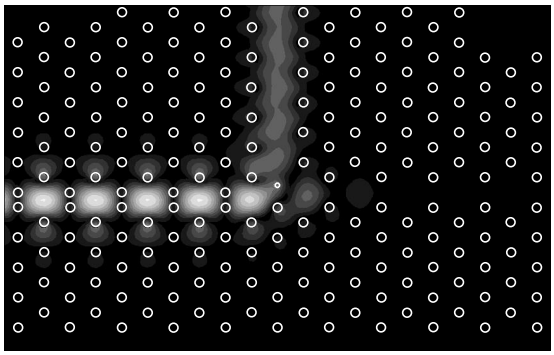

$\omega a/(2\pi c) = 0.478$

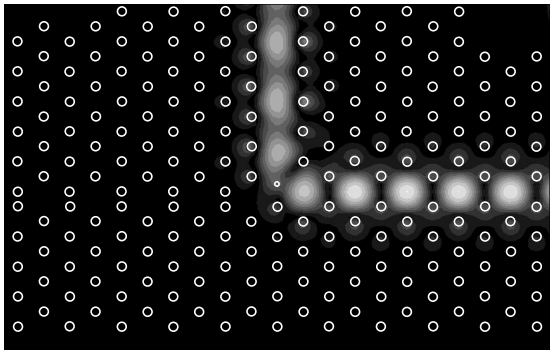

$\omega a/(2\pi c) = 0.437$

Fig. 5.21 Filtering behavior of the T-junction structure with the additional rod in the central cavity (Fig. 5.20). The plotted field is the time averaged electric field. The absence of standing waves in the input waveguide indicates very small reflection coefficients.

considered. In the central cavity one additional rod is included (Fig. 5.20). Adjusting the radius r' and position of this column by trial and error, the power transmitted towards the left is 98.8% for the high frequency, and 93.3% towards the right for the low frequency (the inaccuracy in the energy conservation was smaller than 1%). The time averaged electric field corresponding to this configuration is plotted in Fig. 5.21. Observe that the standing waves in the input waveguide have almost disappeared (especially for the high frequency), which means that the reflection coefficients are very small.

To conclude, let us add a last comment about stacking faults. There exists the common belief that waveguides based on this defect type make more difficult the design of photonic crystal circuits. To create a stacking fault, two crystal pieces are slid with respect to each other. Thus, a waveguide crossing the whole crystal appears, which is not very convenient to design a circuit. However, one further

sliding of another crystal piece can compensate the previous sliding, creating in this way a finite length defect. Besides the example shown above, Fig. 5.22 shows another structure where only stacking faults and vacancy line defects were employed. This configuration could be used to implement a coupler.

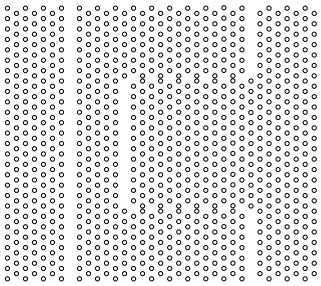

Fig. 5.22 Example of the use of stacking fault waveguides to implement a coupler.

6

Modeling and optimization of non-periodic gratings

6.1 Introduction

In chapter 5, several types of discontinuities in various photonic crystal waveguides were analyzed. Here, a complex discontinuity –a non-periodic grating in a dielectric slab waveguide– is modeled and optimized. Conventional devices are usually based on elements with a continuous or discrete translational invariance. Only recently, non-periodic structures with feature sizes in the order of a wavelength have been employed in the design of optical devices. This is not due to an intrinsic superiority of the conventional elements, but rather to technological and computational difficulties in the design of the non-periodic ones. In fact, non-periodic light coupling structures which are more efficient [194], compact [195], or multifunctional [196] have been demonstrated. However, developing non-periodic devices poses the additional problem of lacking a guiding heuristic to help in the design optimization. In this framework two important issues have to be faced. First, fast computational methods enabling the calculation of a large number of non-periodic configurations in a reasonable time are needed. Second, optimization algorithms that search efficiently the space of configurations have to be employed. For these reasons, it is important to investigate simultaneously computational and optimization techniques.

In this chapter the focus is on the design of non-periodic grating output couplers in dielectric slabs. Several techniques have been proposed for the computation of finite and/or non-periodic gratings, such as for example FDTD [197], the Green's tensor method [198], the pseudospectral method [199], the method of lines [200], the boundary integral method [201], the boundary variation method [202], the mode matching method [203], and the field stitching method [204]. Here, a new approximate method based on the MMP technique is developed, where the main goal is to achieve a fast computation of the diffracted far field. As it will be explained later, the approximation is accurate when consecutive grating lines are not extremely close to each other. Although the method cannot be applied to every conceivable grating structure, it is very well suited for the optimization of certain structures where thousands of computations must be performed, which would require prohibitively long calculation times with the mentioned rigorous techniques. The idea of the method is partially related to

the stitching technique. It consists of three steps: (*i*) the non-periodic grating is separated in its individual grating grooves, and the near field scattering problem of every single groove is computed with MMP, (*ii*) a near-to-far field transformation is performed, and (*iii*) the scattered far fields are assembled together to compute the total scattered far field diffracted by the non-periodic grating.

The developed method has been especially conceived for optimization purposes, which, in the context of non-periodic structures, become very difficult. These difficulties arise due to the huge size of the space of possible configurations and to the existence of multiple local optima where conventional optimization algorithms may be trapped. Therefore, evolutionary optimization algorithms are considered most appropriate for these complex searches [205–209]. Evolutionary algorithms can efficiently search large regions of the configuration space and thus the lack of a guiding heuristic for the device optimization becomes less critical. For this motive the computational method has been designed in such a way that it can be advantageously combined with an evolutionary strategy.

Joining the fast computational technique based on the MMP method together with an evolutionary search algorithm, a non-periodic grating output coupler has been optimized that suppresses an unwanted second diffracted order.

The approximate method for the fast computation of the far fields diffracted by non-periodic gratings is presented in section 6.2. Then, in section 6.3 the method is combined with an evolutionary algorithm in order to optimize a grating coupler.

6.2 Modeling of non-periodic gratings

As mentioned above, three steps are required for the computation of the far fields diffracted by a non-periodic grating. They are described in subsections 6.2.1, 6.2.2, and 6.2.3, respectively.

6.2.1 Near field scattered by one single waveguide perturbation

The problem considered in this subsection is depicted in Fig. 6.1: an incident mode guided by a dielectric slab is scattered by a perturbation. The slab waveguide is asymmetric. It consists of substrate, guiding film, and cladding with refractive indices given by n_{s}, n_{f}, and n_{c}, respectively. Only slab perturbations which are translationally invariant along the Z axis (orthogonal to the figure plane) are considered. In the XY cross section the perturbation can be represented as a protrusion, a notch or the inclusion of a domain with a different refractive index n_{p}. To situate the presented problem in the context of the whole optimization, it can be said that this subsection is devoted to the scattering by only one groove of the overall non-periodic grating.

For the computation of the diffraction by the whole grating (see subsection 6.2.3) the following data of the single-groove problem have to be determined: transmission T and reflection R coefficients for the amplitude of the mode guided by the slab, and scattered *near* field $S^{\mathrm{near}}(r, \theta)$ toward substrate and cladding[1].

[1]The angle θ is measured counterclockwise from the right side of a horizontal axis; for $0 < \theta < \pi$ this reference axis is the film-cladding interface whereas for $\pi < \theta < 2\pi$ it is the film-substrate interface (see Fig. 6.1).

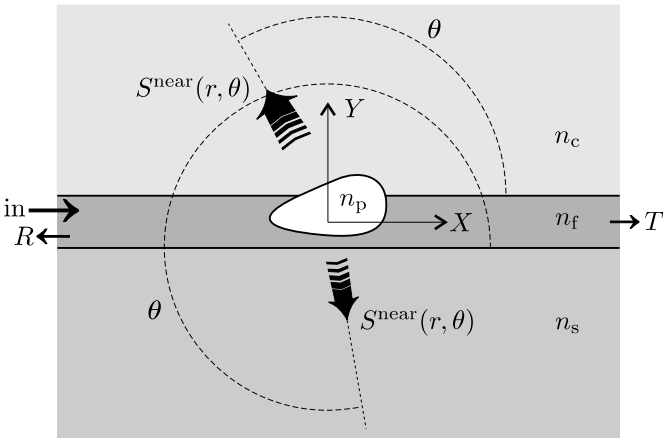

Fig. 6.1 Diagram of a slab waveguide with a perturbation. The incident mode (in) comes from the left. T, R and $S^{\text{near}}(r, \theta)$ represent transmission, reflection, and scattering, respectively. The refractive indices n_s, n_f, n_c, and n_p are also shown.

$S^{\text{near}}(r, \theta)$ denotes generically the fields needed for the computation of the scattered near field [for instance, in H polarization $H_z(\mathbf{r})$ suffices to compute the radiation pattern]. For simplicity, only the case of a single-moded waveguide is treated here, but the extension to the multimode case would simply require the consideration of all possible scattering channels to the various guided modes.

For the later steps in the optimization scheme it is relatively unimportant which numerical technique is used for the computation of T, R and $S^{\text{near}}(r, \theta)$. The MMP method was employed because it allows a very accurate determination of the fields and it gives an estimation of the numerical errors. As it will be explained in subsection 6.2.2, the very nature of the MMP method also permits a direct near-to-far field transformation, which is another reason to rely on the MMP technique.

The definition of the MMP boundaries for conventional waveguide discontinuities has been already discussed in Refs. [186–188]. Here a slightly different definition is used motivated by the following two considerations: (*i*) In order to allow an easy extraction of T and R, the fields at the output (right) and input (left) –far from the perturbation, i.e. several wavelengths away– are written as a superposition of the guided modes plus some basis functions representing the fields scattered towards substrate and cladding. Therefore the left and right sides of the system have to be separated by fictitious boundaries (see subsection 2.2.7). (*ii*) To simplify the imposition of the correct asymptotic behavior for $S^{\text{near}}(r, \theta)$, the scattered field (far from the perturbation) is represented by a multipole expansion radiating from the perturbation. On the other hand, close to the perturbation (in the "interaction" region), the fields are expanded as a superposition of many multipole expansions to account for the complexity of the field (and eventually –when the perturbation is weak– a transmitted guided mode). For this reason, fictitious boundaries separating the interaction region

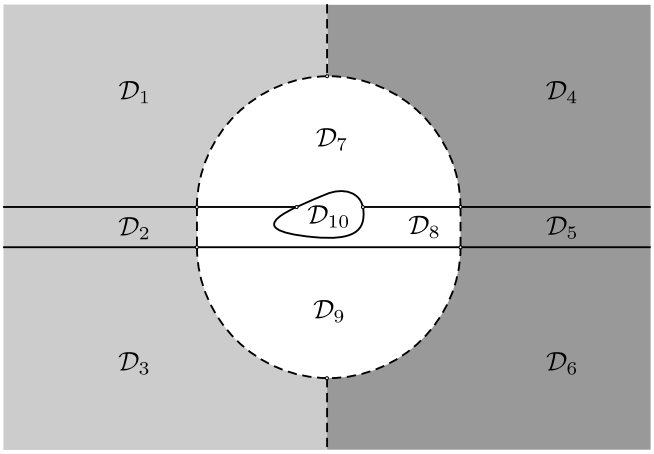

Fig. 6.2 Diagram of the domains and boundaries employed for the solution of the near field scattering problem. The fictitious boundaries are the dashed lines. $\mathcal{D}_1$, $\mathcal{D}_2$, $\mathcal{D}_3$ (resp. $\mathcal{D}_4$, $\mathcal{D}_5$, $\mathcal{D}_6$) constitute the input (resp. output) "section" whereas $\mathcal{D}_7$, $\mathcal{D}_8$, $\mathcal{D}_9$, $\mathcal{D}_{10}$ constitute the "interaction" region.

and the far field are needed. The fictitious boundaries $\partial\mathcal{D}_{ij}$ are thus chosen in such a way that they define input and output "sections" and one interaction region (Fig. 6.2).

In the input section, the field is expanded as incoming and reflected modes[2] (each of them given by a connection, see subsection 2.2.7) plus two multipoles (located at the film interfaces, at $x = 0$) radiating towards the input section cladding $\mathcal{D}_1$ and input section substrate $\mathcal{D}_3$, respectively. In the output section, the field is expanded as a transmitted mode (again a connection) plus two multipoles (located in the same way as above) radiating towards the output section cladding $\mathcal{D}_4$ and output section substrate $\mathcal{D}_6$, respectively. To avoid any radiation toward $\theta = 0, \pi$ in the input and output sections, the order and angular dependence of the multipoles radiating towards domains $\mathcal{D}_1$, $\mathcal{D}_3$, $\mathcal{D}_4$, and $\mathcal{D}_6$ are chosen appropriately. Near the perturbation, the multipoles that represent the field in the interaction region are positioned with the Automatic Multipole Setting technique described in chapter 3. Figure 6.3 depicts an example of such an automatically generated multipole distribution near a perturbation.

To illustrate the procedure explained above, the following example with a very weak perturbation (see Fig. 6.3) is given. The refractive indices of the structure are $n_\mathrm{s} = 1.57$, $n_\mathrm{f} = 2.35$, and $n_\mathrm{c} = 1.33$. The film thickness is $t = 150$ nm and the perturbation consists of a rectangular notch inside the film at the film-cladding interface (depth $d_\mathrm{c} = 10$ nm and width $w_\mathrm{c} = 60$ nm) and a rectangular protrusion outside the film at the film-substrate interface (depth $d_\mathrm{s} = 10$ nm and

[2]For a slab waveguide the expression for the guided modes is known analytically, and for other kinds of input and output waveguides it can be computed as in section 4.5.

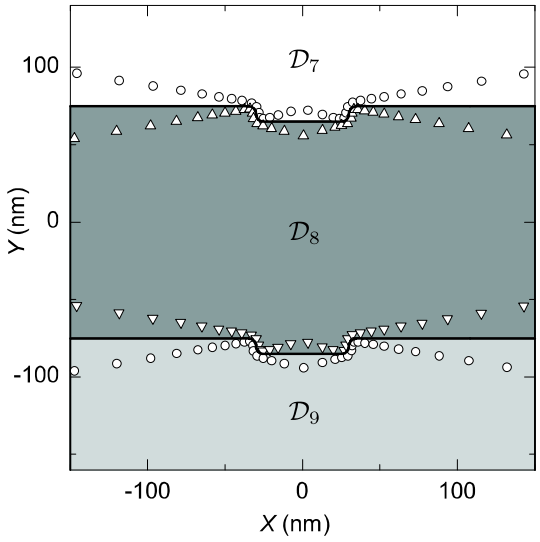

Fig. 6.3 Distribution of multipole expansions around a waveguide perturbation, generated with the Automatic Multipole Setting technique described in chapter 3. The $\triangle$'s, $\triangledown$'s, and $\circ$'s represent the positions of multipoles expanding the fields in cladding, substrate, and film, respectively.

width $w_s = 60$ nm)[3]. The notch and protrusion centers are vertically aligned. The slab supports one guided mode with effective refractive index $n_{\text{eff}} = 1.7235$ (H polarization) at the operating wavelength (in vacuum) $\lambda_0 = 785$ nm. The simulation shows the following redistribution of power due to the scattering process (all values are normalized to the incident power): transmitted $|T|^2 = 0.999602$, reflected $|R|^2 = 0.000082$ and radiated 0.000310. The inaccuracy in the power conservation is 0.000006 (i.e., 1.9% of the radiated power). It is worth mentioning that the accurate computation of the fields radiated by such a weak perturbation still represents a challenge for many computational methods.

Figure 6.4 shows the time-averaged Poynting vector field. From this field distribution it is clear that most of the radiated power propagates backwards. The ripples parallel to the film interfaces are due to the interference between guided modes and the field scattered in directions close to the grazing angles. Observe the different ripples periods on the right side (co-propagation of guided mode and radiation) and the left side (counter-propagation of guided mode and radiation). This effect has been observed with other computational methods [210].

The numerical details are summarized as follows: 458 multipole expansions are employed to simulate the fields in the interaction region (most of them have 4-th order and a few have 7-th order); the four multipoles representing the radiation in the input and output sections are of 12-th order; the total number of unknowns is 4859. The radii of the circular fictitious boundaries ($\partial\mathcal{D}_{17}$, $\partial\mathcal{D}_{39}$, etc.) are 4 μm

[3]The corners of notch and protrusion are rounded with a radius $r_c = 5$ nm.

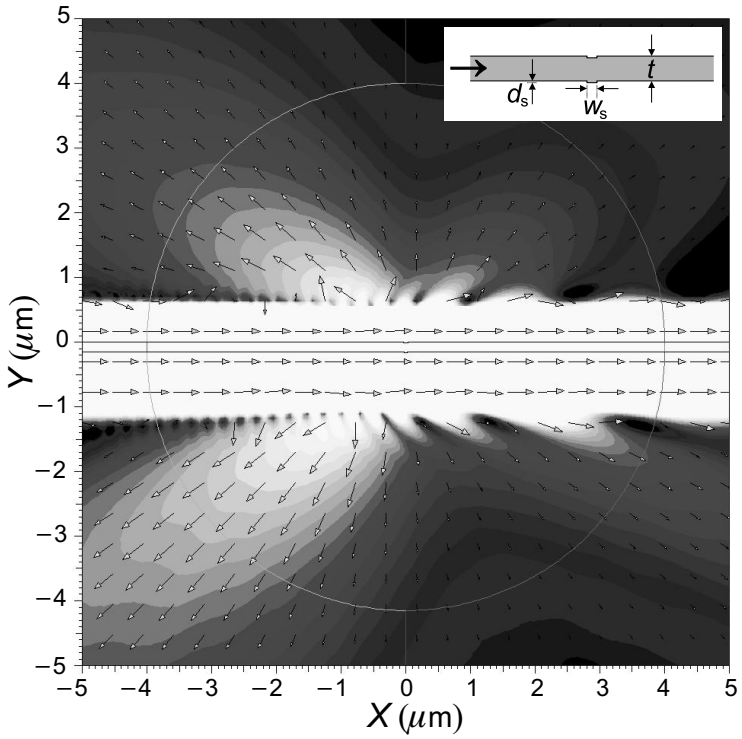

Fig. 6.4 Time-averaged Poynting vector field for a slab waveguide with the perturbation shown in the inset (see also Fig. 6.3).

and the lengths of the boundaries $\partial\mathcal{D}_{14}$, $\partial\mathcal{D}_{36}$, $\partial\mathcal{D}_{12}$, $\partial\mathcal{D}_{23}$, $\partial\mathcal{D}_{45}$ and $\partial\mathcal{D}_{56}$ are 4 μm as well. The maximum relative error along the boundaries is 1.4% (in fact the average relative error is 0.02% and the previous value of 1.4% is reached only where the field is negligible). The computation time is about 5 hours (all computations in this chapter were performed on a computer with a Pentium III, 665 MHz processor).

6.2.2 Near-to-far field transformation

For the design of a grating coupler intended for free space coupling, an efficient way to compute the scattered radiated *far* field is needed. The solution presented in subsection 6.2.1 is very accurate in the *near* field but it shows some divergencies in the far field. The reason is that, when separating the input section, output section and interaction region, fictitious boundaries were introduced [for instance boundary $\partial\mathcal{D}_{17}$ or boundary $\partial\mathcal{D}_{14}$ (Fig. 6.5)]. Boundary $\partial\mathcal{D}_{17}$ poses no problems but boundary $\partial\mathcal{D}_{14}$ should be infinitely long and has to be truncated at a certain distance from the perturbation. When the computed solution is examined along the Y axis in the far field (for values of $|y|$ larger than about 20 wavelengths), a distinct field mismatch is observed which renders the solution useless for the far field computation. To avoid this effect a near-to-far field transformation is

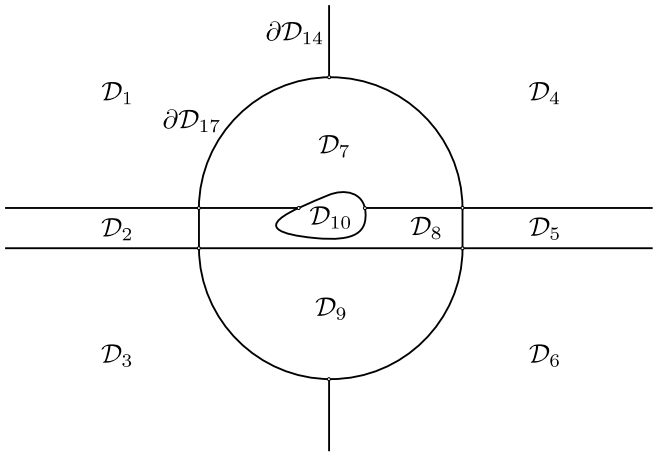

Fig. 6.5 Domains and boundaries employed for the solution of the near field scattering problem. Note that some boundaries should be infinite and are truncated, e.g., $\partial\mathcal{D}_{14}$.

introduced.

The near-to-far field transformation can be very easily computed in the framework of the MMP method. The reason is that scattered far fields are often represented as a sum of multipolar functions, which are the natural basis functions within the MMP method. The MMP near-to-far field transformation has been already described for other configurations [187]. In the case of a slab waveguide

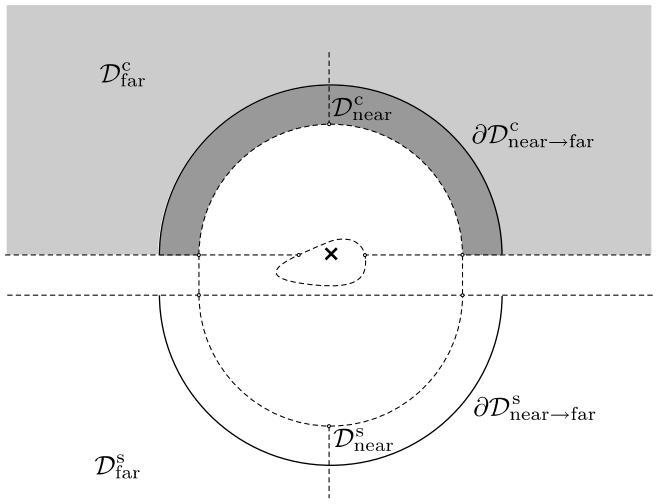

Fig. 6.6 Domains and boundaries employed for the near-to-far field transformation. The superscripts 'c' and 's' denote cladding and substrate, respectively. The domains relevant for the transformation of the cladding fields are shaded. The $\times$ is the location of the multipole expansion representing the field in $\mathcal{D}^{\mathrm{c}}_{\mathrm{far}}$.

with a perturbation, the film divides the space in two half-spaces and it is therefore advantageous to use one multipole expansion to represent the scattered field towards the cladding and another multipole expansion for the scattered field in the substrate.

The transformation works as follows (it is explained for the radiation towards the cladding and the same procedure is valid for the substrate): (*i*) The near field scattering problem is solved as in subsection 6.2.1. Note that the pure scattered radiated field (i.e., without incident, transmitted and reflected guided modes) can be unambiguously computed in the input ($\mathcal{D}_1$) and output ($\mathcal{D}_4$) cladding regions but not in the interaction ($\mathcal{D}_7$) cladding region. The reason is that only in $\mathcal{D}_1$ and $\mathcal{D}_4$ is the field a superposition of guided modes (with unambiguously defined amplitudes) plus radiation. (*ii*) A new MMP problem is defined (see Fig. 6.6). It consists of two domains $\mathcal{D}^{\mathrm{c}}_{\mathrm{near}}$ and $\mathcal{D}^{\mathrm{c}}_{\mathrm{far}}$ separated by a fictitious boundary $\partial\mathcal{D}^{\mathrm{c}}_{\mathrm{near}\to\mathrm{far}}$. In $\mathcal{D}^{\mathrm{c}}_{\mathrm{near}}$ the field is represented by a connection which contains the near field scattered *radiation* computed in (*i*). If one takes into account the comment in (*i*), it is clear that $\partial\mathcal{D}^{\mathrm{c}}_{\mathrm{near}\to\mathrm{far}}$ has to be outside $\mathcal{D}_7$. In domain $\mathcal{D}^{\mathrm{c}}_{\mathrm{far}}$ the field is represented by one single multipole expansion. This expansion is located near the center of the perturbation (at the film-cladding interface). The number of orders of this multipole depends on the desired accuracy, but only those orders and angular dependences that do not radiate towards $\theta = 0, \pi$ are chosen. The coefficients of this expansion are yet to be determined and they are found by solving a standard MMP problem where the excitation $\Phi^{\mathcal{D}^{\mathrm{c}}_{\mathrm{near}}}_{\mathrm{exc}}(\mathbf{r})$ is the connection containing the near field radiation. The multipole expansion represents the *far* radiated field diffracted towards the cladding. The amplitude of this computed scattered radiated far field is denoted by $S^{\mathrm{far}}(\theta)$ (the r variable

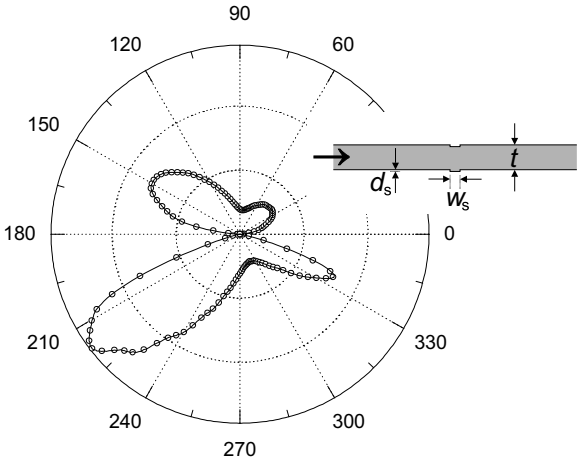

Fig. 6.7 Comparison of the radiation pattern computed directly with the MMP method (solid line) and with the equivalent multipoles determined with the near-to-far field transformation (circles). The waveguide perturbation is shown in the inset (see also Fig. 6.3).

is dropped because the radial dependence is trivial in the far field). For instance, in H polarization $S^{\text{far}}(\theta) = H_z^{\text{far}}(\theta)$.

To illustrate the near-to-far field transformation, the scattered Poynting vector field has been computed in two different ways: (*i*) directly with the standard MMP method, and (*ii*) with the two "equivalent" multipoles found with the standard MMP method plus additional near-to-far field transformation. Figure 6.7 shows the radial component of the field plotted along $\partial\mathcal{D}^{\text{c}}_{\text{near}\to\text{far}}$ and $\partial\mathcal{D}^{\text{s}}_{\text{near}\to\text{far}}$. As it can be seen, the correspondence between both is very good. The waveguide perturbation considered here is the same as described in subsection 6.2.1.

The numerical details for the cladding near-to-far field transformation are summarized here (similar data for the substrate): 1 multipole (order 25) is employed to simulate the far field. The radius of $\partial\mathcal{D}^{\text{c}}_{\text{near}\to\text{far}}$ is 6 μm. The maximum relative error along $\partial\mathcal{D}^{\text{c}}_{\text{near}\to\text{far}}$ is 4.8% (in fact the average relative error is 0.5% and the previous value 4.8% is only reached where the field is negligible). The computation time is about 9 seconds. Note that once the equivalent multipoles have been determined, computing the radiated far field requires a negligible time.

6.2.3 Far field scattered by a non-periodic grating

One of the elements needed for the successful optimization of grating structures is a fast and reliable algorithm to evaluate the quality of every potential solution. Determining the fitness of a grating requires a technique for the computation of the diffracted fields (i.e., a *forward solver*). For a non-periodic structure, the impossibility of defining a primitive unit cell with Bloch boundary conditions makes the rigorous computation of the scattered fields extremely time and memory consuming. In particular, the standard MMP method would require long

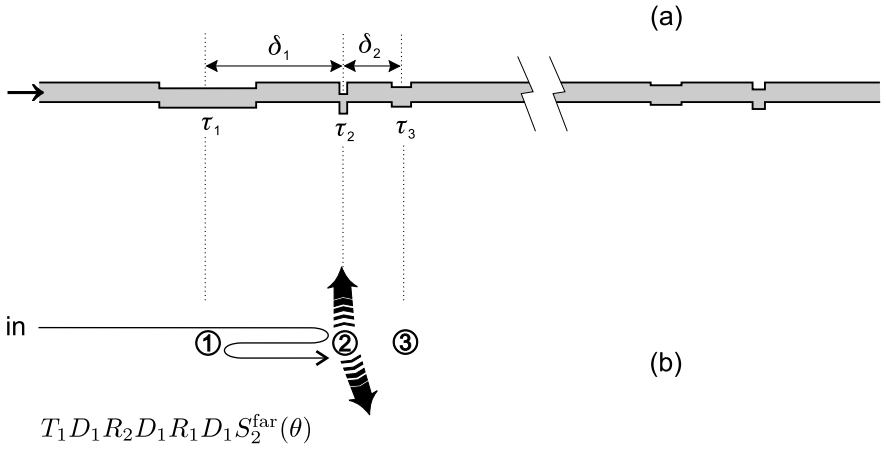

Fig. 6.8 (a) Non-periodic grating, (b) Multiple scattering of the incident mode by the non-periodic grating. A possible path –followed by a mode– linking the input and the radiation output channel is shown. ①, ②, ③ represent the equivalent multipoles corresponding to the grooves shown in (a). The remaining symbols are explained in the text.

times for the accurate calculation of the fields diffracted by non-periodic gratings with more than three or four grating grooves. This is a critical issue because the space of different non-periodic grating configurations is huge. For this motive a method has been elaborated that enables a fast approximate computation of the far field diffracted by non-periodic gratings. The procedure is described in the next paragraphs.

The non-periodic grating can be contemplated as a concatenation of (possibly) different grooves [Fig. 6.8(a)]. For every different groove type τ_m in the structure a new scattering problem is defined: the scattering of a guided mode by the groove τ_m. For this single-groove diffraction problem the transmission T_m, reflection R_m and scattered near field $S_m^{\text{near}}(r, \theta)$ can be rigorously determined as already shown in subsection 6.2.1. Then, a near-to-far field transformation is performed for every different groove (as it was demonstrated in subsection 6.2.2). In this way, the two equivalent multipoles radiating the same far field $S_m^{\text{far}}(\theta)$ as the corresponding grating groove τ_m are found. The computation of the equivalent multipoles for every groove type is time consuming (due to the near field computation), but usually fabrication constraints limit the number of potential groove profiles within a structure. In such a case only a few single-groove scattering problems have to be solved. Moreover, this computation has to be done only once for each different type of groove: once the equivalent multipoles are found they are stored in a "library of equivalent sources" which can be used to construct the far field radiated by a grating composed of the corresponding grooves.

The diffraction by the whole non-periodic structure is represented by a multiple scattering process as follows [Fig. 6.8(b)]. The input mode hits the first perturbation and it is partially transmitted (T_1), reflected (R_1) and scattered

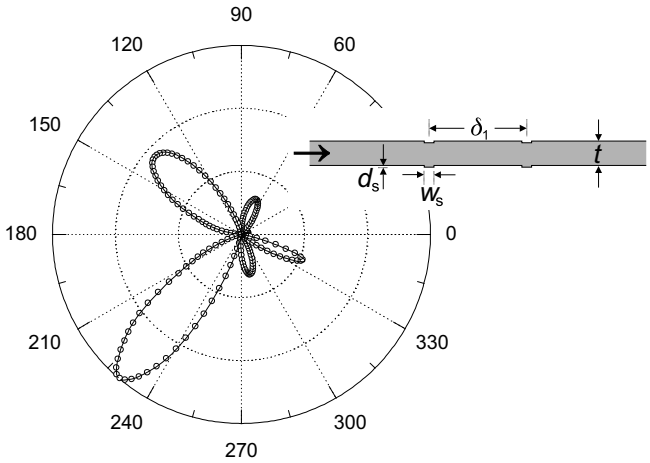

Fig. 6.9 Comparison of the radiation pattern computed directly with the MMP method (solid line) and with the multiple scattering procedure (circles) (computed along two half-circumferences of radii 6 μm). The perturbation in the waveguide is shown in the inset.

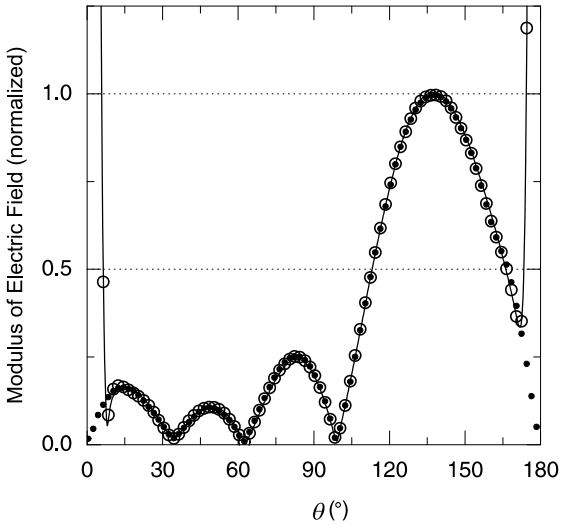

Fig. 6.10 Modulus of the electric field computed with the Green's tensor technique (solid line), the standard MMP method (circles) and with the multiple scattering procedure (dots). The field is computed along a half-circumference of radius 6 μm. The perturbation in the waveguide is the same as shown in the inset of Fig. 6.9. Note that with both rigorous methods the plotted field is the total electric field (i.e., including the guided mode whose evanescent tails are present for $\theta = 0°, 180°$) whereas with the multiple scattering procedure the guided mode is not included. The phase of the incident guided mode is $-115°$.

$[S_1^{\text{far}}(\theta)]$. The subsequent transmitted mode (T_1) accumulates a phase in the travel between the first and second perturbation and becomes $T_1 D_1$ [D_1 represents the phase factor accumulated between the first and second corrugation, $D_1 = \exp(i2\pi\delta_1/\lambda_{\text{eff}})$, where δ_1 stands for the distance between the first and second corrugations and λ_{eff} is the effective wavelength of the guided mode]. At the second perturbation, the mode $T_1 D_1$ is transmitted ($T_1 D_1 T_2$), reflected ($T_1 D_1 R_2$) and scattered $[T_1 D_1 S_2^{\text{far}}(\theta)]$ again. This process is iteratively cascaded. For example the reflected mode $T_1 D_1 R_2$ is propagated backwards and it scatters at the first perturbation producing the contributions $T_1 D_1 R_2 D_1 T_1$ (guided backwards), $T_1 D_1 R_2 D_1 R_1$ (guided forward) and $T_1 D_1 R_2 D_1 S_1^{\text{far}}(\theta)$ (radiated backwards). The amplitude T_{grating} of the transmitted mode at the right side of the grating is calculated as an infinite sum of terms. Each term consists of a product of factors T_j, R_k, D_l, and represents a possible path –followed by the mode– connecting the input and the output at the right side (each term contains an even number of reflection factors R_k). A similar consideration can be used to compute the amplitude R_{grating} of the reflected mode at the left side of the grating, but this time using paths starting at the input and returning back to it (this is the second output channel). In this case each term contains an odd number of reflection factors R_k. The scattered far field is computed in a similar way: it is a sum of terms containing several factors T_j, R_k, D_l, and one factor $S_m^{\text{far}}(\theta)$. Every

such a term represents a path linking the input and a third output channel: the radiation field.

The described back and forth scattering process should include an infinite number of contributions. However, when the reflection coefficients are small enough the series converges rapidly. In this case only those contributions with a number of reflection factors R_m less than a given value must be considered. It is also important noticing that the approximation is valid if consecutive grooves are far enough from each other, since otherwise the following two important effects would arise. First, the field hitting a groove (coming from the previous one) would not be a pure propagating guided mode, but it would include a complex contribution of evanescent modes that are not easy to evaluate within the proposed scheme. Second, the field radiated by one groove could couple with the next groove being re-radiated or coupled back into the waveguide.

As illustration of the procedure and to verify its accuracy, the scattering by a grating composed by two equal grooves is presented. The grooves in the slab are those described in subsection 6.2.1 and the distance δ_1 from center to center of the grooves is $\delta_1 = 600$ nm. All other parameters remain the same as in subsection 6.2.1. Figure 6.9 plots the normalized radiation pattern obtained both with the rigorous MMP method and with the multiple scattering procedure presented here. A further comparison is shown in Fig. 6.10, where the electric field is plotted as computed with two rigorous methods (the standard MMP and the Green's tensor technique [198]) and the approximate technique presented here. Observe the nearly perfect agreement between the rigorous calculations and the approximate one in both figures. The observed differences between the rigorous techniques and the approximate one (for $\theta = 0°, 180°$ in Fig. 6.10) are not real discrepancies. They are simply due to the following fact: with the approximate technique the radiated field (and not the guided modes) is computed, while the rigorous techniques compute the total field including the guided modes, whose evanescent tails completely mask the radiation toward directions close to $\theta = 0°, 180°$.

Another example with larger and closer perturbations is shown in Fig. 6.11. The multiple scattering computation works correctly even though the perturbations are only 500 nm apart from each other. Note that this distance is only 0.85 wavelengths in the cladding, 1.0 wavelengths in the substrate and 1.5 wavelengths of the guided mode. For smaller δ_1 the procedure becomes less accurate. The minimal distance $\delta_{\min}$ for which the procedure is still accurate depends on the shape of the grooves. The value of $\delta_{\min}$ is carefully evaluated by comparing the far field obtained with a rigorous MMP computation to that obtained with the proposed multiple scattering method (at the fictitious boundaries given by the near-to-far field transformation) for an appropriate set of decreasing distances. Due to the continuous nature of potentially emerging evanescent field interactions at small distances, a proper definition of $\delta_{\min}$ is always possible because the interrelated mismatch between both far fields is well behaved. In the context of the application presented in the next section a value of $\delta_{\min} = 500$ nm was found. Figure 6.11 shows that for this minimal distance the agreement between approximate and rigorous computations is still excellent apart from some

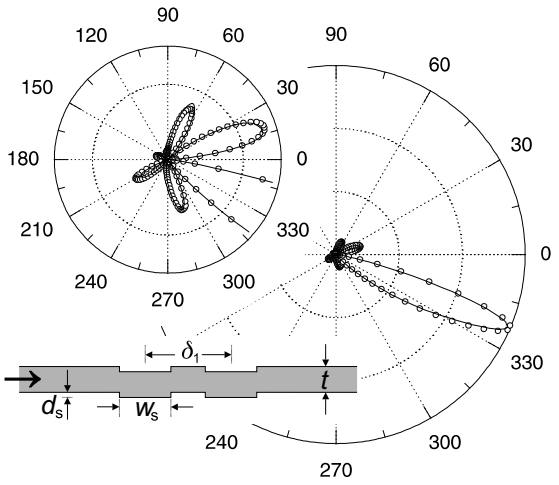

Fig. 6.11 Comparison of the radiation pattern computed directly with the MMP method (solid line) and with the multiple scattering procedure (circles) (computed along two half-circumferences of radii 6 μm). The upper inset shows a magnified view. The perturbation is shown in the lower inset ($d_s = 30$ nm, $w_s = 300$ nm, $\delta_1 = 500$ nm).

marginal deviations in the minor side lobes of the radiation pattern.

The computing time required for the rigorous MMP calculation of the structure with two grooves is about 5 hours. Provided the library of equivalent sources is already known, the time needed with the multiple scattering procedure is 3 seconds (only those contribution with less than three reflection R_k coefficients were taken into account). For the non-periodic gratings with 40 grooves computed in the next section, the simulation time is about 30 seconds.

6.3 Evolutionary optimization of non-periodic gratings

Non-periodic structures offer the promise of a higher degree of freedom as compared with periodic ones. This freedom can be used to design devices which incorporate several functionalities at once. A means to circumvent the problems of large computation times and large memory requirement for the calculation of diffraction by non-periodic gratings has been explored in the section 6.2. This technique permits evaluating the quality of a large number of potentially interesting configurations in a reasonable time. But searching the enormous space of possible non-periodic configurations requires not only a fast forward solver but also a powerful global search algorithm.

Due to the size of the search space and given the combinatorial character of the non-periodic gratings considered here, search schemes based on evolutionary algorithms appear to be most promising for the optimization of these coupling structures [206, 211, 212]. For this reason, the forward solver presented in subsection 6.2.3 has been conceived in such a way that it can be easily and advantageously combined with an evolutionary algorithm. To pursue this point in more detail, let us consider that the scattering by a non-periodic grating has

already been computed. If the positions of two grating grooves are interchanged or the distance between two consecutive grooves is altered, a normal forward solver would require starting the computation of a new scattering problem from scratch. With the proposed forward solver this does not require any new lengthy field calculation.

The optimizations performed here can be described by specification of the following elements: (*i*) the evaluation of the quality (fitness) of a non-periodic grating structure, (*ii*) the encoding of a structure as a chromosome-like object that can be handled by an evolutionary search strategy, and (*iii*) the description of the evolutionary search strategy itself.

In connection with (*i*), for the non-periodic grating couplers designed here, a certain *far field intensity pattern* has to be achieved. Thus, using the forward solver previously presented, the fitness of a given structure (which depends on its far field intensity pattern) can be determined. An example of a fitness function for an specific optimization goal is shown later.

Regarding (*ii*), the number of grooves of the grating is fixed to a given number N_{grooves}. The structure is described by specification of a sequence of groove types τ_m, (selected from a total number N_{types} of different groove types) and a sequence of distances δ_m between these perturbations [Fig. 6.8(a)]. The distances between grooves have to be larger than a certain minimum distance $\delta_{\min}$ to avoid too strong coupling between consecutive grooves[4] and they are bounded by a maximum distance $\delta_{\max}$ to keep the coupler as short as possible. In short, a given allowed structure is specified by a chromosome including N_{grooves} integer parameters (the groove types, $1 \leq \tau_m \leq N_{\text{types}}$) and $N_{\text{grooves}} - 1$ real parameters (the distances, $\delta_{\min} < \delta_m < \delta_{\max}$):

$$(\tau_1, \tau_2, \ldots, \tau_{N_{\text{grooves}}} | \delta_1, \delta_2, \ldots, \delta_{N_{\text{grooves}}-1}). \tag{6.1}$$

With respect to point (*iii*), a standard Evolutionary Strategy has been employed [213]. In the algorithm, several parameters (like population size, recombination type, mutation rates, etc.) have to be chosen. For each different problem these parameters can be tuned for optimal performance. These parameters were tuned for other relevant optimization examples and then the same set of parameters was used for the present search.

To illustrate the described ideas the following coupler optimization is presented. The chosen parameters are relevant in the context of sensor applications [214]. The operating wavelength (in vacuum) is $\lambda_0 = 785$ nm and the polarization is H. The guiding film is 150 nm thick and the refractive indices of substrate, film, and cladding are $n_{\text{s}} = 1.57$, $n_{\text{f}} = 2.35$, and $n_{\text{c}} = 1.33$, respectively. For this design the goal is restricting the light out-coupled towards the substrate in the following way: the coupler should radiate near the angle $\theta_{\text{out}} \simeq 285°$ with an angular width of the beam not larger than a few degrees (for the definition of θ, see Fig. 6.1). The radiation towards other angles in the

[4] As explained before, this minimum distance $\delta_{\min}$ between two grooves is obtained by comparison of the multiple scattering computation and the MMP rigorous computation for decreasing distances.

substrate has to be suppressed but there are no restrictions towards the cladding. This radiation pattern is needed to reduce crosstalk and background noise. To facilitate the manufacturing process, the groove geometry has been chosen to be a notch-protrusion pair such as that described in subsection 6.2.1 [i.e. the dimensions of the protrusion have to be equal to those of the notch, $w_c = w_s \equiv w$, $d_c = d_s \equiv d$ and both with the same x coordinate (Fig. 6.3)][5].

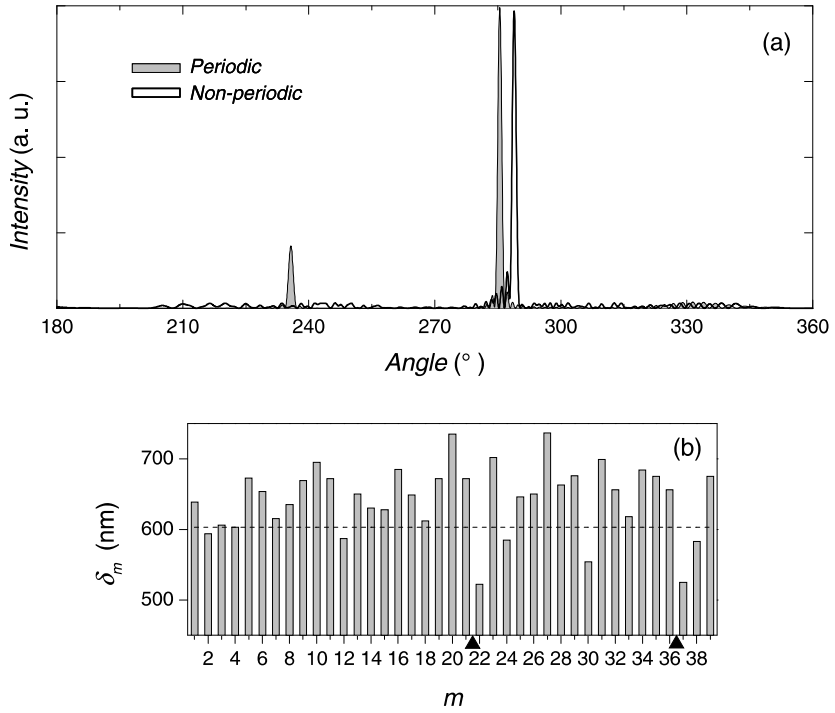

Fig. 6.12 (a) Intensity out-coupled by two different grating structures towards the substrate as a function of the angle θ (for the definition of θ, see Fig. 6.1). *Periodic* coupler (shaded) and *non-periodic* optimized coupler (thick line). Note the suppression of the unwanted second diffracted order, (b) Distances δ_m in the non-periodic optimized grating. The dashed line shows the period ($\Delta = 603$ nm) of the periodic configuration. The ▲'s represent the location of the grooves of the second type τ_2.

The optimal parameters for a *periodic* design would be: period $\delta_m = \Delta = 603$ nm for all m, groove width $w = 300$ nm and groove depth $d = 30$ nm[6]. As it can be seen in Fig. 6.12(a), such a periodic grating (with 40 grooves) couples out a beam towards the desired direction, but an additional (unwanted) second diffracted order towards the substrate is present as well.

[5]In this section all notch and protrusion corners are rounded with a radius $r_c = 10$ nm.

[6]For this period Δ and groove width w, the maximum groove depth d is limited. Above a certain threshold the coupling between consecutive grooves is too strong and the forward solver is not accurate.

In the optimization of the *non-periodic* grating the number of grating grooves is again fixed at $N_{\text{grooves}} = 40$ (for ease of comparison with the periodic case). Two different types of groove are allowed ($N_{\text{types}} = 2$): for the first type (τ_1), $w = 300$ nm and $d = 30$ nm (i.e., the same as in the periodic case), whereas for the second type (τ_2), $w = 60$ nm and $d = 70$ nm. The shape of the second groove type has been chosen in such a way that its radiation pattern is quite different from the radiation pattern of the first groove type. The minimum and maximum distances between grooves are fixed at $\delta_{\min} = 500$ nm, $\delta_{\max} = 2000$ nm. The fitness function of a structure is defined as follows:

$$\frac{\min_{\theta \in \Theta_{\text{allowed}}} [I(\theta)]}{\max_{\theta \in \Theta_{\text{not allowed}}} [I(\theta)]}, \tag{6.2}$$

where $I(\theta)$ is the intensity radiated (in the far field) as a function of the angle and the angular domains Θ_{allowed}, $\Theta_{\text{not allowed}}$ are defined as $\Theta_{\text{allowed}} = (280^\circ,\ 290^\circ)$, $\Theta_{\text{not allowed}} = (180^\circ,\ 280^\circ) \cup (290^\circ,\ 360^\circ)$.

Regarding the optimized non-periodic structure found by the evolutionary algorithm several remarks are important. First, the intensity pattern of Fig. 6.12(a) clearly demonstrates the suppression of the unwanted second diffracted order towards the substrate. Second, in the initial (random) population of structures both groove types have the same probability of being present inside a structure. Along the evolution process the grooves of the second type (τ_2) are eliminated. The solution found has only two grooves of the second type [Fig. 6.12(b)] and they would have been probably eliminated if the optimization would have run for a longer time. The reason is likely the fact that this second type of groove radiates predominantly in the backward (unwanted) direction whereas the first type radiates predominantly in the forward direction. Notice that the *selection* of the substructures which are appropriate for the optimization goal has been performed automatically by the algorithm, allowing us to gather knowledge about the underlying physics. Third, the optimized distances δ_m are scattered slightly above the period of the periodic structure ($\Delta = 603$ nm) but do not show any clear regularity [Fig. 6.12(b)]. A fourth last comment is that the desired beam in the optimized non-periodic configuration is shifted towards the upper bound of Θ_{allowed} [Fig. 6.12(a)]. We believe this to be due to the fact that the radiating pattern of a single groove of the first type has its maximum for an angle larger than $\theta_{\text{out}} = 285^\circ$. Therefore a higher fitness is obtained if the beam shifts towards the upper bound of the angular interval Θ_{allowed}.

7

Summary, conclusions, and outlook

In the following sections a recapitulation of the main results obtained in this dissertation is presented, conclusions are drawn, and a perspective of open problems and further work is sketched.

7.1 Automatic Multipole Setting and surface plasmons computations

In chapter 3, a procedure for the automatic positioning of the multipole expansions used in MMP and valid for cylindrical structures has been developed. The technique extracts the appropriate sources locations from the geometry of the boundary that defines the simulation domain, taking into account its global shape. This AMS method has been employed for the simulation of several systems including surface plasmons, band structures of photonic crystals, metallic waveguides, and perturbations in dielectric slab waveguides.

The AMS technique is interesting in connection with two main aspects: First, since the choice of appropriate locations for the multipole expansions is the most difficult part in the MMP method, the AMS considerably simplifies the MMP modeling. Second, it is an indispensable tool when electrodynamic systems with varying shape are analyzed (see, for instance, section 4.5). The multipole expansions distributions generated with this AMS technique are suitable for the modeling of systems supporting surface plasmons (this kind of systems presents a complex field dynamic, which only a few numerical methods can analyze accurately). Two applications have been considered: plasmon-assisted resonant tunneling of light through metallic gratings, and large electromagnetic field enhancement in cylindrical metallic particles.

In its present state, the implemented technique can be applied to fairly general geometries. However, it is not absolutely robust, which is a necessary feature if one desires combining the AMS technique with an optimization algorithm. Two other areas which deserve further study are the design of practical AMS procedures for the 3D MMP method, and adaptive multipole setting. This last topic consists in using the information about a computed approximate solution (such as MMP errors, field distribution, etc.) to generate a multipole distribution which allows one the calculation of a more accurate approximation.

7.2 Computation of eigenvalue problems and photonic crystal band structures

A method for the computation of non-linear eigenvalue problems has been presented in chapter 4. It is based on the excitation of the investigated system with a multipolar source, while changing the value of the magnitude (λ) for which an eigenvalue is searched. When λ approaches the eigenvalue, the system resonates, increasing the field amplitude enormously. In this way, the eigenvalues can be found by looking for these resonances as a function of λ. With the help of this method, band structures of metallic perfect photonic crystals with various geometries have been computed, point and line defects in photonic crystals have been characterized, and the modal fields and propagation constants of waveguides have been determined.

The method presented here is one of the few available techniques to compute the band structure of photonic crystals containing dispersive materials with arbitrary $\varepsilon(\omega)$ and complex geometry. On the one hand, it can be stressed that high accuracies can be achieved with this method. It has to be said, however, that –for non-dispersive materials– it is very likely slower than other methods specifically designed for this kind of systems.

In connection with the subject presented in this section, there are some interesting topics which could be investigated in the future: a more thorough study of the possible cost functions to be employed for the determination of the eigenvalues, the utilization of symmetry considerations to reduce the numerical effort, the MMP computation of the band structure of 3D photonic crystals, and the 2D case but with off-plane propagation.

7.3 Photonic crystal waveguide discontinuities

The modeling of discontinuities in photonic crystal waveguides has been addressed in chapter 5. The method explained there is a generalization of known techniques to the case of systems with discrete translational invariance. The proposal is the following: the input and output channels are cut at a certain distance from the discontinuity, and the field is matched at those ports to the modal fields of the corresponding infinitely long waveguides. Several applications of this concept have been shown, such as photonic crystal waveguide bends, T-junctions, and antennas.

Due to the perfect impedance matching of the outgoing fields at the in/out ports, no spurious reflections are produced. This is a very interesting feature as compared with the standard computational methods. Up to now, the known methods suffer from one of the two following problems: either they require a huge computational domain, or they cannot separate the transmitted fields and the fields reflected at the waveguide terminations. By contrast, the technique presented here employs the minimum possible computational domain, and characterizes accurately the analyzed waveguide discontinuities.

In chapter 5 no result was presented regarding the coupling of photonic crystal and conventional waveguides. Here one figure is shown (Fig. 7.1) displaying preliminary results concerning this topic. Another possible direction of research

is the study of evanescent modes in photonic crystal waveguides: For discontinuities in conventional metallic waveguides, the interaction region can be reduced to less than one wavelength if additional evanescent modes in the input and output ports are considered. This possibility could be explored for photonic crystal waveguides as well, to reduce even more the size of the simulation domain.

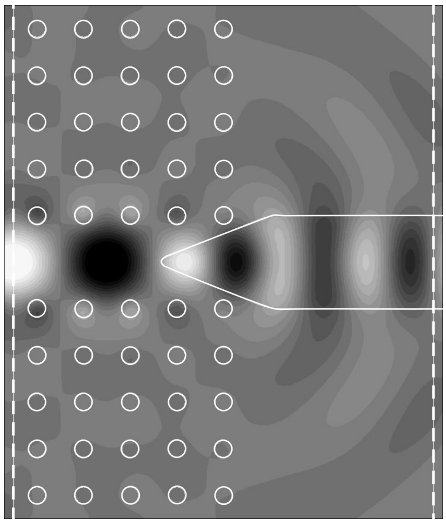

Fig. 7.1 Transition between a photonic crystal waveguide and a conventional dielectric slab waveguide. The system has been modeled using the same principles as in chapter 5.

7.4 Modeling and optimization of non-periodic gratings

The last topic studied in this dissertation is the modeling and optimization of non-periodic grating couplers (chapter 6). An approximate method for the computation of the far field diffracted by a non-periodic grating has been proposed. It is based on the substitution of the field diffracted by a grating groove with the field radiated by one equivalent multipole (computed with the help of a near-to-far field transformation). The fields diffracted by the whole array of grating grooves are assembled together to compute the total diffracted far field. Thanks to the speed of the method, it is suitable for optimization purposes, where many computations are required. It has been combined with an evolutionary algorithm in order to optimize a non-periodic coupler.

Although several other methods are available for the simulation of non-periodic gratings, they are useless in the optimization context. The reason is that, being rigorous techniques, they are also slow. The method developed here is only approximate, not valid for every kind of grating, and does compute only the far diffracted field. Nevertheless in its domain of applicability it is extremely fast, which is the required feature for optimization purposes.

Evolutionary algorithms have been barely employed in this dissertation. However, there are many interesting problems in the context of this work where they could be used. Let us cite only two of them: combined with the methods presented in section 4.5 it would be possible to optimize the waveguide cross section in order to tailor the modal fields or dispersion relation, and combined with the ideas of chapter 5 they could be used to design photonic crystal antennas, or filters with improved features.

Bibliography

[1] R. F. Service, "Can Chip Devices Keep Shrinking?", Science **274**(5294), 1834–1836 (Dec. 1996).

[2] T. Ito and S. Okazaki, "Pushing the limits of lithography", Nature (London) **406**(6799), 1027–1031 (Aug. 2000).

[3] D. A. Muller, T. Sorsch, S. Moccio, F. H. Baumann, K. Evans-Lutterodt, and G. Timp, "The electronic structure at the atomic scale of ultrathin gate oxides", Nature (London) **399**(6738), 758–761 (June 1999).

[4] T. F. Krauss and R. M. De La Rue, "Photonic crystals in the optical regime – past, present and future", Progress Quantum Electron. **23**(2), 51–96 (Mar. 1999).

[5] C. Manolatou, S. G. Johnson, S. Fan, P. R. Villeneuve, H. A. Haus, and J. D. Joannopoulos, "High-Density Integrated Optics", J. Lightwave Technol. **17**(9), 1682–1692 (Sept. 1999).

[6] H. Kosaka, T. Kawashima, A. Tomita, M. Notomi, T. Tamamura, T. Sato, and S. Kawakami, "Photonic crystals for micro lightwave circuits using wavelength-dependent angular beam steering", Appl. Phys. Lett. **74**(10), 1370–1372 (Mar. 1999).

[7] E. Yablonovitch, "Inhibited Spontaneous Emission in Solid-State Physics and Electronics", Phys. Rev. Lett. **58**(20), 2059–2062 (May 1987).

[8] S. John, "Strong Localization of Photons in Certain Disordered Dielectric Superlattices", Phys. Rev. Lett. **58**(23), 2486–2489 (June 1987).

[9] G. Parker and M. Charlton, "Photonic crystals", Phys. World **13**(8), 23–34 (Aug. 2000).

[10] O. Painter, K. Srinivasan, J. D. O'Brien, A. Scherer, and P. D. Dapkus, "Tailoring of the resonant mode properties of optical nanocavities in two-dimensional photonic crystal slab waveguides", J. Opt. A: Pure Appl. Opt. **3**(6), S161–S170 (Nov. 2001).

[11] J. K. Hwang, H. Y. Ryu, D. S. Song, I. Y. Han, H. K. Park, D. H. Jang, and Y. H. Lee, "Continuous Room-Temperature Operation of Optically Pumped Two-Dimensional Photonic Crystal Lasers at 1.6 μm", IEEE Photon. Technol. Lett. **12**(10), 1295–1297 (Oct. 2000).

[12] M. Tokushima and H. Yamada, "Photonic crystal line defect waveguide directional coupler", Electron. Lett. **37**(24), 1454–1455 (Nov. 2001).

[13] S. John and M. Florescu, "Photonic bandgap materials: towards an all-optical micro-transistor", J. Opt. A: Pure Appl. Opt. **3**(6), S103–S120 (Nov. 2001).

[14] S.-Y. Lin, E. Chow, V. Hietala, P. R. Villeneuve, and J. D. Joannopoulos, "Experimental Demonstration of Guiding and Bending of Electromagnetic Waves in a Photonic Crystal", Science **282**(5387), 274–276 (Oct. 1998).

[15] K. M. Ho, C. T. Chan, and C. M. Soukoulis, "Existence of a Photonic Gap in Periodic Dielectric Structures", Phys. Rev. Lett. **65**(25), 3152–3155 (Dec. 1990).

[16] A. Mekis, J. C. Chen, I. Kurland, S. Fan, P. R. Villeneuve, and J. D. Joannopoulos, "High Transmission through Sharp Bends in Photonic Crystal Waveguides", Phys. Rev. Lett. **77**(18), 3787–3790 (Oct. 1996).

[17] C. Hafner, *Post-modern Electromagnetics. Using Intelligent MaXwell Solvers*, John Wiley and Sons, Chichester, 1999.

[18] C. Hafner, *Beiträge zur Berechnung der Ausbreitung elektromagnetischer Wellen in zylindrischen Strukturen mit Hilfe des "Point-Matching"-Verfahrens*, Diss. ETH Nr. 6683, Eidgenössische Technische Hochschule Zürich, 1980.

[19] T. Wriedt, editor, *Generalized Multipole Techniques for Electromagnetic and Light Scattering*, Elsevier, Amsterdam, 1999.

[20] Ref. [17], chapter 6, page 189.

[21] C. Hafner, *Numerische Berechnung elektromagnetischer Felder: Grundlagen, Methoden, Anwendungen*, Springer, Berlin, 1987.

[22] C. Hafner, *The Generalized Multipole Technique for Computational Electromagnetics*, Artech House, Boston, 1990.

[23] M. G. Imhof and M. N. Toksöz, "Multiple Multipole Expansions for Acousto-Elastic Multiple Scattering", in *Electromagnetic and Light Scattering - Theory and Applications III*, edited by T. Wriedt and Y. Eremin, pages 117–124, Universität Bremen, Bremen, 1998.

[24] Ref. [17], chapter 9, pages 277–294.

[25] L. Novotny and C. Hafner, "Light propagation in a cylindrical waveguide with a complex, metallic, dielectric function", Phys. Rev. E **50**(5), 4094–4106 (Nov. 1994).

[26] C. Hafner, "Multiple multipole program computation of periodic structures", J. Opt. Soc. Am. A **12**(5), 1057–1067 (May 1995).

[27] L. Novotny, D. W. Pohl, and P. Regli, "Light propagation through nanometer-sized structures: the two-dimensional-aperture scanning near-field optical microscope", J. Opt. Soc. Am. A **11**(6), 1768–1779 (June 1994).

[28] N. B. Piller and O. J. F. Martin, "Scattering by anisotropic bodies with the generalized multipole technique", in *Electromagnetic and Light Scattering - Theory and Applications III*, edited by T. Wriedt and Y. Eremin, pages 249–256, Universität Bremen, Bremen, 1998.

[29] F. G. Bogdanov, D. D. Karkashadze, and R. S. Zaridze, *The Method of Auxiliary Sources in Electromagnetic Scattering Problems*, in Ref. [19], chapter 7, pages 143–172.

[30] J. D. Jackson, *Classical Electrodynamics*, chapter 8.2, page 341, John Wiley and Sons, New York, 2nd edition, 1975.

[31] I. N. Vekua, *New methods for solving elliptic equations*, North-Holland, Amsterdam, 1967.

[32] R. E. Collin, *Field Theory of Guided Waves*, chapter 1.4, page 19, IEEE Press, New York, 2nd edition, 1991.

[33] J. A. Stratton, *Electromagnetic theory*, chapter 9.1, pages 485–486, McGraw-Hill, New York, 1941.

[34] G. H. Golub and C. F. Van Loan, *Matrix Computations*, John Hopkins University Press, Baltimore, 1996.

[35] Ref. [17], chapter 8, pages 254–256.

[36] Ref. [22], chapter 7.3, page 193.

[37] Ref. [17], chapter 8, pages 275–276.

[38] Ref. [22], chapter 7.2, pages 159–174.

[39] F. G. Bogdanov, D. D. Karkashadze, and R. S. Zaridze, *The Method of Auxiliary Sources in Electromagnetic Scattering Problems*, in Ref. [19], chapters 7.2–7.4, pages 145–154.

[40] Y. Leviatan and A. Boag, "Analysis of Electromagnetic Scattering from Dielectric Cylinders Using a Multifilament Current Model", IEEE Trans. Antennas Propag. **35**(10), 1119–1127 (Oct. 1987).

[41] S. Eisler and Y. Leviatan, "Analysis of electromagnetic scattering from metallic and penetrable cylinders with edges using a multifilament current model", IEE Proc. H **136**(6), 431–438 (Dec. 1989).

[42] K. I. Beshir and J. E. Richie, "On the Location and Number of Expansion Centers for the Generalized Multipole Technique", IEEE Trans. Electromagn. Compat. **38**(2), 177–180 (May 1996).

[43] P. B. Leuchtmann, "Automatic Computation of Optimum Origins of the Poles in the Multiple Multipole Method (MMP-Method)", IEEE Trans. Magn. **19**(6), 2371–2374 (Nov. 1983).

[44] P. B. Leuchtmann, *Automatisierung der Funktionenwahl bei der MMP-Methode*, Diss. ETH Nr. 8301, Eidgenössische Technische Hochschule Zürich, 1987.

[45] P. Regli, *Automatische Wahl der sphärischen Entwicklungsfunktionen für die 3D-MMP Methode*, Diss. ETH Nr. 9946, Eidgenössische Technische Hochschule Zürich, 1992.

[46] C. Tudziers, *Verbesserung der Anwendbarkeit der Multipolmethode durch automatisches Setzen der Entwicklungsparameter und Parallelisierung*, Ph.D. dissertation, Technischen Universität Hamburg-Harburg, 1996.

[47] Ref. [22], chapter 7.4.3, pages 209–212.

[48] Ref. [22], chapter 7.2, pages 167–169.

[49] A. G. Kyurkchan, A. I. Sukov, and A. I. Kleev, *Singularities of Wave Fields and Numerical Methods of Solving the Boundary-Value Problems for Helmholtz Equation*, in Ref. [19], chapters 5.2–5.4, pages 82–102.

[50] R. Zaridze, G. Bit-Babik, K. Tavzarashvili, N. Uzunoglu, and D. Economou, "Some Recent Developments in Method of Auxiliary Sources for Inverse and Scattering Problems on Large and Complex Structure", in *Electromagnetic and Light Scattering - Theory and Applications III*, edited by T. Wriedt and Y. Eremin, pages 287–294, Universität Bremen, Bremen, 1998.

[51] Ref. [22], chapter 7.2, pages 169–170.

[52] Ref. [44], chapters 4.1.1.1–4.1.1.2, pages 32–37.

[53] F. G. Bogdanov, D. D. Karkashadze, and R. S. Zaridze, *The Method of Auxiliary Sources in Electromagnetic Scattering Problems*, in Ref. [19], chapter 7.4.1, pages 149–151.

[54] J. P. Kottmann, O. J. F. Martin, D. R. Smith, and S. Schultz, "Field polarization and polarization charge distributions in plasmon resonant nanoparticles", New J. Phys. **2**(27), 1–9 (Nov. 2000).

[55] Ref. [45], chapter 3.4.5, pages 43–45.

[56] Ref. [45], chapter 2.5, pages 29–31.

[57] Ref. [22], chapter 7.2, page 166.

[58] C. Hafner, *MaX-1. A Visual Electromagnetics Platform*, John Wiley and Sons, Chichester, 1998.

[59] C. F. Bohren and D. R. Huffman, *Absorption and Scattering of Light by Small Particles*, John Wiley and Sons, New York, 1983.

[60] U. Kreibig and M. Vollmer, *Optical Properties of Metal Clusters*, Springer, Berlin, 1995.

[61] H. Raether, *Surface Plasmons on Smooth and Rough Surfaces and on Gratings*, Springer, Berlin, 1988.

[62] F. Meriaudeau, T. R. Downey, A. Passian, A. Wig, and T. L. Ferrel, "Environment effects on surface-plasmon spectra in gold-island films potential for sensing applications", Appl. Opt. (OT) **37**(34), 8030–8037 (Dec. 1998).

[63] T. Okamoto, I. Yamaguchi, and T. Kobayashi, "Local plasmon sensor with gold colloid monolayers deposited upon glass substrates", Opt. Lett. **25**(6), 372–374 (Mar. 2000).

[64] S. Nie and S. R. Emory, "Probing Single Molecules and Single Nanoparticles by Surface-Enhanced Raman Scattering", Science **275**(5303), 1102–1106 (Feb. 1997).

[65] M. Quinten, A. Leitner, J. R. Krenn, and F. R. Aussenegg, "Electromagnetic energy transport via linear chains of silver nanoparticles", Opt. Lett. **23**(17), 1331–1333 (Sept. 1998).

[66] S. A. Maier, M. L. Brongersma, and H. A. Atwater, "Electromagnetic energy transport along arrays of closely spaced metal rods as an analogue to plasmonic devices", Appl. Phys. Lett. **78**(1), 16–18 (Jan. 2001).

[67] M. L. Brongersma, J. W. Hartman, and H. A. Atwater, "Electromagnetic energy transfer and switching in nanoparticle chain arrays below the diffraction limit", Phys. Rev. B **62**(24), 16356–16359 (Dec. 2000).

[68] J. Weeber, A. Dereux, C. Girard, G. Colas des Francs, J. R. Krenn, and J.-P. Goudonnet, "Optical addressing at the subwavelength scale", Phys. Rev. E **62**(5), 7381–7388 (Nov. 2000).

[69] S. J. Oldenburg, G. D. Hale, J. B. Jackson, and N. J. Halas, "Light scattering from dipole and quadrupole nanoshell antennas", Appl. Phys. Lett. **75**(8), 1063–1065 (Aug. 1999).

[70] J. R. Krenn, G. Schider, W. Rechberger, B. Lamprecht, A. Leitner, F. R. Aussenegg, and J. C. Weeber, "Design of multipolar plasmon excitations in silver nanoparticles", Appl. Phys. Lett. **77**(21), 3379–3381 (Nov. 2000).

[71] J. Takahara, S. Yamagishi, H. Taki, A. Morimoto, and T. Kobayashi, "Guiding of a one-dimensional optical beam with nanometer diameter", Opt. Lett. **22**(7), 475–477 (Apr. 1997).

[72] P. Berini, "Plasmon-polariton modes guided by a metal film of finite width bounded by different dielectrics", Opt. Express **7**(10), 329–335 (Nov. 2000).

[73] R. M. Dickson and L. A. Lyon, "Unidirectional Plasmon Propagation in Metallic Nanowires", J. Phys. Chem. B **104**(26), 6095–6098 (July 2000).

[74] J.-C. Weeber, A. Dereux, C. Girard, J. R. Krenn, and J.-P. Goudonnet, "Plasmon polaritons of metallic nanowires for controlling submicron propagation of light", Phys. Rev. B **60**(12), 9061–9068 (Sept. 1999).

[75] T. Klar, M. Perner, S. Grosse, G. von Plessen, W. Spirkl, and J. Feldmann, "Surface-Plasmon Resonances in Single Metallic Nanoparticles", Phys. Rev. Lett. **80**(19), 4249–4252 (May 1998).

[76] J.-C. Weeber, C. Girard, J. R. Krenn, A. Dereux, and J.-P. Goudonnet, "Near-field optical properties of localized plasmons around lithographically designed nanostructures", J. Appl. Phys. **86**(5), 2576–2583 (Sept. 1999).

[77] N. Richard, "Polarization and spectroscopy analysis of the scattering by nanoscopic objects in the near-field optics", J. Appl. Phys. **88**(5), 2318–2325 (Sept. 2000).

[78] C. Sönnichsen, S. Geier, N. E. Hecker, G. von Plessen, J. Feldmann, H. Ditlbacher, B. Lamprecht, J. R. Krenn, F. R. Aussenegg, V. Z.-H. Chan, J. P. Spatz, and M. Möller, "Spectroscopy of single metallic nanoparticles using total internal reflection microscopy", Appl. Phys. Lett. **77**(19), 2949–2951 (Nov. 2000).

[79] T. W. Ebbesen, H. J. Lezec, H. F. Ghaemi, T. Thio, and P. A. Wolff, "Extraordinary optical transmission through sub-wavelength hole arrays", Nature (London) **391**(6668), 667–669 (Feb. 1998).

[80] J. A. Porto, F. J. García-Vidal, and J. B. Pendry, "Transmission Resonances on Metallic Gratings with Very Narrow Slits", Phys. Rev. Lett. **83**(14), 2845–2848 (Oct. 1999).

[81] H. Kano and W. Knoll, "A scanning microscope employing localized surface-plasmon-polaritons as a sensing probe", Opt. Commun. **182**(1–3), 11–15 (Aug. 2000).

[82] M. G. Somekh, S. Liu, T. S. Velinov, and C. W. See, "High-resolution

scanning surface-plasmon microscopy", Appl. Opt. (OT) **39**(34), 6279–6287 (Dec. 2000).

[83] W.-C. Tan, J. R. Sambles, and T. W. Preist, "Double-period zero-order metal gratings as effective selective absorbers", Phys. Rev. B **61**(19), 13177–13182 (May 2000).

[84] W.-C. Tan, T. W. Preist, and R. J. Sambles, "Resonant tunneling of light through thin metal films via strongly localized surface plasmons", Phys. Rev. B **62**(16), 11134–11138 (Oct. 2000).

[85] Ref. [59], chapters 5.2–5.4, pages 136–150.

[86] C. Girard and A. Dereux, "Near-field optics theories", Rep. Prog. Phys. **59**(5), 657–699 (May 1996).

[87] T. Wriedt, "A Review of Elastic Light Scattering Theories", Part. Part. Syst. Charact. **15**(2), 67–74 (Apr. 1998).

[88] N. Félidj, J. Aubard, and G. Lévi, "Discrete dipole approximation for ultraviolet-visible extinction spectra simulation of silver and gold colloids", J. Chem. Phys. **111**(3), 1195–1208 (July 1999).

[89] M. Quinten, A. Pack, and R. Wannenmacher, "Scattering and extinction of evanescent waves by small particles", Appl. Phys. B **68**(1), 87–92 (Jan. 1999).

[90] N. Richard, "Light Scattering by Supported Metallic Nanostructres: Polarization and Spectroscopy in the Near-Field Zone", Phys. Status Solidi B **220**(2), 1009–1024 (Aug. 2000).

[91] J. R. Krenn, A. Dereux, J. C. Weeber, E. Bourillot, Y. Lacroute, J. P. Goudonnet, G. Schider, W. Gotschy, A. Leitner, F. R. Aussenegg, and C. Girard, "Squeezing the Optical Near-Field Zone by Plasmon Coupling of Metallic Nanoparticles", Phys. Rev. Lett. **82**(12), 2590–2593 (Mar. 1999).

[92] J. P. Kottmann, O. J. F. Martin, D. R. Smith, and S. Schultz, "Spectral response of plasmon resonant nanoparticles with a non-regular shape", Opt. Express **6**(11), 213–219 (May 2000).

[93] W.-C. Tan, T. W. Preist, J. R. Sambles, and N. P. Wanstall, "Flat surface-plasmon-polariton bands and resonant optical absorption on short-pitch metal gratings", Phys. Rev. B **59**(19), 12661–12666 (May 1999).

[94] J. P. Kottmann and O. J. F. Martin, "Accurate Solution of the Volume Integral Equation for High-Permittivity Scatterers", IEEE Trans. Antennas Propag. **48**(11), 1719–1726 (Nov. 2000).

[95] U. Kreibig and C. v. Fragstein, "The Limitation of Electron Mean Free Path in Small Silver Particles", Zeit. Phys. **224**(4), 307–323 (1969).

[96] D. Dalacu and L. Martinu, "Optical properties of discontinuous gold films: finite-size effects", J. Opt. Soc. Am. B **18**(1), 85–92 (Jan. 2001).

[97] J. Lermé, "Introduction of quantum finite-size effects in the Mie's theory for a multilayered metal sphere in the dipolar approximation: Application to free and matrix-embedded noble metal clusters", Eur. Phys. J. D **10**(2), 265–277 (May 2000).

[98] J. P. Kottmann and O. J. F. Martin, "Plasmon resonant coupling in metallic nanowires", Opt. Express **8**(12), 655–663 (June 2001).

[99] L. Martín-Moreno, F. J. García-Vidal, H. J. Lezec, K. M. Pellerin, T. Thio, J. B. Pendry, and T. W. Ebbesen, "Theory of Extraordinary Optical Transmission through Subwavelength Hole Arrays", Phys. Rev. Lett. **86**(6), 1114–1117 (Feb. 2001).

[100] R. S. Popovidi-Zaridze, D. D. Karkashadze, G. Z. Akhvlediani, and D. S. Khatiashvili, "Investigation of the possibilities of the method of auxiliary sources for solving two-dimensional electrodynamics problems", Radiotekhnika i Elektronika **26**(2), 254–262 (Feb. 1981) [Radio Engineering and Electronic Physics **26**(2), 36–43 (Feb. 1981)].

[101] K. Sakoda, N. Kawai, T. Ito, A. Chutinan, S. Noda, T. Mitsuyu, and K. Hirao, "Photonic bands of metallic systems. I. Principle of calculation and accuracy", Phys. Rev. B **64**(4), 045116/1–8 (July 2001).

[102] S. Fan, P. R. Villeneuve, and J. D. Joannopoulos, "Large omnidirectional band gaps in metallodielectric photonic crystals", Phys. Rev. B **54**(16), 11245–11251 (Oct. 1996).

[103] M. Qiu and S. He, "A nonorthogonal finite-difference time-domain method for computing the band structure of a two-dimensional photonic crystal with dielectric and metallic inclusions", J. Appl. Phys. **87**(12), 8268–8275 (June 2000).

[104] R. Dautray and J.-L. Lions, editors, *Mathematical Analysis and Numerical Methods for Science and Technology. Spectral Theory and Applications*, Springer, Berlin, 1990.

[105] I. Stakgold, *Green's functions and boundary value problems*, John Wiley and Sons, New York, 1979.

[106] A. Galindo and P. Pascual, *Quantum Mechanics I*, Springer, Berlin, 1990.

[107] J. B. Nielsen, T. Sondergaard, S. E. Barkou, A. Bjarklev, J. Broeng, and M. B. Nielsen, "Two-dimensional Kagomé structure, fundamental hexagonal photonic crystal configuration", Electron. Lett. **35**(20), 1736–1737 (Sept. 1999).

[108] C. M. Anderson and K. P. Giapis, "Larger Two-Dimensional Photonic Band Gaps", Phys. Rev. Lett. **77**(14), 2949–2952 (Sept. 1996).

[109] C. M. Anderson and K. P. Giapis, "Symmetry reduction in group 4mm photonic crystals", Phys. Rev. B **56**(12), 7313–7320 (Sept. 1997).

[110] D. Cassagne, C. Jouanin, and D. Bertho, "Hexagonal photonic-band-gap structures", Phys. Rev. B **53**(11), 7134–7142 (Mar. 1996).

[111] P. R. Villeneuve, S. Fan, and J. D. Joannopoulos, "Microcavities in photonic crystals: Mode symmetry, tunability, and coupling efficiency", Phys. Rev. B **54**(11), 7837–7842 (Sept. 1996).

[112] V. Kuzmiak and A. A. Maradudin, "Symmetry analysis of the localized modes associated with substitutional and interstitial defects in a two-dimensional triangular photonic crystal", Phys. Rev. B **61**(16), 10750–10761 (Apr. 2000).

[113] A. Adibi, R. K. Lee, Y. Xu, A. Yariv, and A. Scherer, "Design of photonic crystal optical waveguides with singlemode propagation in the photonic bandgap", Electron. Lett. **36**(16), 1376–1378 (Aug. 2000).

[114] T. Sondergaard and K. H. Dridi, "Energy flow in photonic crystal waveguides", Phys. Rev. B **61**(23), 15688–15696 (June 2000).

[115] J. B. Nielsen, T. Sondergaard, S. E. Barkou, A. Bjarklev, and J. Broeng, "Two-Dimensional Kagomé Photonic Bandgap Waveguide", IEEE Photon. Technol. Lett. **12**(6), 630–632 (June 2000).

[116] M. Loncar, J. Vuckovic, and A. Scherer, "Methods for controlling positions of guided modes of photonic-crystal waveguides", J. Opt. Soc. Am. B **18**(9), 1362–1368 (Sept. 2001).

[117] M. Qiu and S. He, "Surface modes in two-dimensional dielectric and metallic photonic band gap structures: a FDTD study", Phys. Lett. A **282**(1-2), 85–91 (Apr. 2001).

[118] X. Zhang, L.-M. Li, Z.-Q. Zhang, and C. T. Chan, "Surface states in two-dimensional metallodielectric photonic crystals studied by a multiple-scattering method", Phys. Rev. B **63**(12), 125114/1–7 (Mar. 2001).

[119] X. Zhang, Z.-Q. Zhang, L.-M. Li, C. Jin, D. Zhang, B. Man, and B. Cheng, "Enlarging a photonic band gap by using insertion", Phys. Rev. B **61**(3), 1892–1897 (Jan. 2000).

[120] A. Moroz, "Three-Dimensional Complete Photonic-Band-gap Structures in the Visible", Phys. Rev. Lett. **83**(25), 5274–5277 (Dec. 1999).

[121] K. Sakoda and K. Ohtaka, "Optical response of three-dimensional photonic lattices: Solutions of inhomogeneous Maxwell's equations and their applications", Phys. Rev. B **54**(8), 5732–5741 (Aug. 1996).

[122] D. Sievenpiper, L. Zhang, R. F. Jimenez Broas, N. G. Alexópolous, and E. Yablonovitch, "High-Impedance Electromagnetic Surfaces with a Forbidden Frequency Band", IEEE Trans. Microwave Theory Tech. **47**(11), 2059–2074 (Nov. 1999).

[123] H. S. Sözüer, J. W. Haus, and R. Inguva, "Photonic bands: Convergence problems with the plane-wave method", Phys. Rev. B **45**(24), 13962–13972 (June 1992).

[124] D. Hermann, M. Frank, K. Busch, and P. Wölfle, "Photonic band structure computations", Opt. Express **8**(3), 167–172 (Jan. 2001).

[125] P. A. Knipp and T. L. Reinecke, "Boundary-element calculations of electromagnetic band-structure of photonic crystals", Physica E **2**(1-4), 920–924 (July 1998).

[126] A. Figotin and Y. A. Godin, "The Computation of Spectra of Some 2D Photonic Crystals", J. Comput. Phys. **136**(2), 585–598 (Sept. 1997).

[127] K. Ohtaka, T. Ueta, and K. Amemiya, "Calculation of photonic bands using vector cylindrical waves and reflectivity of light for an array of dielectric rods", Phys. Rev. B **57**(4), 2550–2568 (Jan. 1998).

[128] S. G. Johnson and J. D. Joannopoulos, "Block-iterative frequency-domain methods for Maxwell's equations in a planewave basis", Opt. Express **8**(3),

173–190 (Jan. 2001).

[129] V. Kuzmiak, A. A. Maradudin, and F. Pincemin, "Photonic band structures of two-dimensional systems containing metallic components", Phys. Rev. B **50**(23), 16835–16844 (Dec. 1994).

[130] V. Kuzmiak, A. A. Maradudin, and A. R. McGurn, "Photonic band structures of two-dimensional systems fabricated from rods of a cubic polar crystal", Phys. Rev. B **55**(7), 4298–4311 (Feb. 1997).

[131] V. Kuzmiak and A. A. Maradudin, "Distribution of electromagnetic field and group velocities in two-dimensional periodic systems with dissipative metallic components", Phys. Rev. B **58**(11), 7230–7251 (Sept. 1998).

[132] T. Ito and K. Sakoda, "Photonic bands of metallic systems. II. Features of surface plasmon polaritons", Phys. Rev. B **64**(4), 045117/1–8 (July 2001).

[133] X. Wang, X.-G. Zhang, Q. Yu, and B. N. Harmon, "Multiple-scattering theory for electromagnetic waves", Phys. Rev. B **47**(8), 4161–4167 (Feb. 1993).

[134] W. C. Sailor, F. M. Mueller, and P. R. Villeneuve, "Augmented-plane-wave method for photonic band-gap materials", Phys. Rev. B **57**(15), 8819–8822 (Apr. 1998).

[135] L. C. Botten, N. A. Nicorovici, R. C. McPhedran, C. Martijn de Sterke, and A. A. Asatryan, "Photonic band structure calculations using scattering matrices", Phys. Rev. E **64**(4), 046603/1–18 (Oct. 2001).

[136] C. T. Chan, Q. L. Yu, and K. M. Ho, "Order-N spectral method for electromagnetic waves", Phys. Rev. B **51**(23), 16635–16642 (June 1995).

[137] J. Arriaga, A. J. Ward, and J. B. Pendry, "Order-N photonic band structures for metals and other dispersive materials", Phys. Rev. B **59**(3), 1874–1877 (Jan. 1999).

[138] K. Sakoda, *Optical Properties of Photonic Crystals*, Springer, Berlin, 2001.

[139] J. B. Pendry and A. MacKinnon, "Calculation of Photon Dispersion Relations", Phys. Rev. Lett. **69**(19), 2772–2775 (Nov. 1992).

[140] W. Axmann and P. Kuchment, "An Efficient Finite Element Method for Computing Spectra of Photonic and Acoustic Band-Gap Materials - I. Scalar case", J. Comput. Phys. **150**(2), 468–481 (Apr. 1999).

[141] C. Caloz, A. K. Skrivervik, and F. E. Gardiol, "Comparison of two methods for the computation of Green's functions in photonic bandgap materials: the eigenmode-expansion method and the phased-array method", Microwave Opt. Technol. Lett. **27**(5), 323–330 (Dec. 2000).

[142] F. Wijnands, J. B. Pendry, F. J. Garcia-Vidal, P. M. Bell, P. J. Roberts, and L. Martín Moreno, "Green's functions for Maxwell's equations: application to spontaneous emission", Opt. Quantum Electron. **29**(2), 199–216 (Feb. 1997).

[143] G. Barton, *Elements of Green's Functions and Propagation: potentials, diffusion, and waves*, Clarendon Press, Oxford, 1989.

[144] T. Inui, Y. Tanabe, and Y. Onodera, *Group Theory and Its Applications in Physics*, Springer, Berlin, 1990.

[145] J. F. Cornwell, *Group Theory and Electronic Energy Bands in Solids*, North-Holland, Amsterdam, 1969.

[146] J. D. Joannopoulos, R. D. Meade, and J. N. Winn, *Photonic Crystals. Molding the Flow of Light*, Princeton University Press, Princeton, 1995.

[147] E. Yablonovitch, T. J. Gmitter, R. D. Meade, A. M. Rappe, K. D. Brommer, and J. D. Joannopoulos, "Donor and Acceptor Modes in Photonic Band Structure", Phys. Rev. Lett. **67**(24), 3380–3383 (Dec. 1991).

[148] M. Sigalas, C. M. Soukoulis, E. N. Economou, C. T. Chan, and K. M. Ho, "Photonic band gaps and defects in two dimensions: Studies of the transmission coefficient", Phys. Rev. B **48**(19), 14121–14126 (Nov. 1993).

[149] G. Tayeb and D. Maystre, "Rigorous theoretical study of finite-size two-dimensional photonic crystals doped by microcavities", J. Opt. Soc. Am. A **14**(12), 3323–3332 (Dec. 1997).

[150] E. Centeno and D. Felbacq, "Rigorous vector diffraction of electromagnetic waves by bidimensional photonic crystals", J. Opt. Soc. Am. A **17**(2), 320–327 (Feb. 2000).

[151] J.-K. Hwang, S.-B. Hyun, H.-Y. Ryu, and Y.-H. Lee, "Resonant modes of two-dimensional photonic bandgap cavities determined by the finite-element method and by use of the anisotropic perfectly matched layer boundary condition", J. Opt. Soc. Am. B **15**(8), 2316–2324 (Aug. 1998).

[152] O. Painter, J. Vuckovic, and A. Scherer, "Defect modes of a two-dimensional photonic crystal in an optically thin dielectric slab", J. Opt. Soc. Am. B **16**(2), 275–285 (Feb. 1999).

[153] H. Benisty, "Modal analysis of optical guides with two-dimensional photonic band-gap boundaries", J. Appl. Phys. **79**(10), 7483–7492 (May 1996).

[154] M. Loncar, T. Doll, J. Vuckovic, and A. Scherer, "Design and Fabrication of Silicon Photonic Crystal Optical Waveguides", J. Lightwave Technol. **18**(10), 1402–1411 (Oct. 2000).

[155] M. Notomi, A. Shinya, K. Yamada, J. Takahashi, C. Takahashi, and I. Yokohama, "Singlemode transmission within photonic bandgap of width-varied single-line-defect photonic crystal waveguides on SOI substrates", Electron. Lett. **37**(5), 293–295 (Mar. 2001).

[156] T. Baba, N. Fukaya, and A. Motegi, "Clear correspondence between theoretical and experimental light propagation characteristics in photonic crystal waveguides", Electron. Lett. **37**(12), 761–762 (June 2001).

[157] N. Stefanou and A. Modinos, "Impurity bands in photonic insulators", Phys. Rev. B **57**(19), 12127–12133 (May 1998).

[158] A. Yariv, Y. Xu, R. K. Lee, and A. Scherer, "Coupled-resonator optical waveguide: a proposal and analysis", Opt. Lett. **24**(11), 711–713 (June 1999).

[159] Y. Xu, R. K. Lee, and A. Yariv, "Propagation and second-harmonic generation of electromagnetic waves in a coupled-resonator optical waveguide", J. Opt. Soc. Am. B **17**(3), 387–400 (Mar. 2000).

[160] M. Bayindir, B. Temelkuran, and E. Ozbay, "Propagation of photons by hopping: A waveguiding mechanism through localized coupled cavities in three-dimensional photonic crystals", Phys. Rev. B **61**(18), 11855–11858 (May 2000).

[161] R. D. Meade, K. D. Brommer, A. M. Rappe, and J. D. Joannopoulos, "Photonic bound states in periodic dielectric materials", Phys. Rev. B **44**(24), 13772–13774 (Dec. 1991).

[162] A. Mekis, S. Fan, and J. D. Joannopoulos, "Bound states in photonic crystal waveguides and waveguide bends", Phys. Rev. B **58**(8), 4809–4817 (Aug. 1998).

[163] A. Chutinan and S. Noda, "Waveguides and waveguide bends in two-dimensional photonic crystal slabs", Phys. Rev. B **62**(7), 4488–4492 (Aug. 2000).

[164] S. Fan, S. G. Johnson, J. D. Joannopoulos, C. Manolatou, and H. A. Haus, "Waveguide branches in photonic crystals", J. Opt. Soc. Am. B **18**(2), 162–165 (Feb. 2001).

[165] J. Yonekura, M. Ikeda, and T. Baba, "Analysis of Finite 2-D Photonic Crystals of Columns and Lightwave Devices Using the Scattering Matrix Method", J. Lightwave Technol. **17**(8), 1500–1508 (Aug. 1999).

[166] T. Baba, N. Fukaya, and J. Yonekura, "Observation of light propagation in photonic crystal optical waveguides with bends", Electron. Lett. **35**(8), 654–655 (Apr. 1999).

[167] A. R. McGurn, "Photonic crystal circuits: A theory for two- and three-dimensional networks", Phys. Rev. B **61**(19), 13235–13249 (May 2000).

[168] A. Boag and B. Z. Steinberg, "Narrow-band microcavity waveguides in photonic crystals", J. Opt. Soc. Am. A **18**(11), 2799–2805 (Nov. 2001).

[169] S. G. Johnson, C. Manolatou, S. Fan, P. R. Villeneuve, J. D. Joannopoulos, and H. A. Haus, "Elimination of cross talk in waveguide intersections", Opt. Lett. **23**(23), 1855–1857 (Dec. 1998).

[170] E. Centeno and D. Felbacq, "Cross waveguides in biperiodic two-dimensional photonic crystals", J. Opt. A: Pure Appl. Opt. **3**(6), S154–S160 (Nov. 2001).

[171] P. R. Villeneuve, D. S. Abrams, S. Fan, and J. D. Joannopoulos, "Single-mode waveguide microcavity for fast optical switching", Opt. Lett. **21**(24), 2017–2019 (Dec. 1996).

[172] M. Agio, E. Lidorikis, and C. M. Soukoulis, "Impurity modes in a two-dimensional photonic crystal: coupling efficiency and Q factor", J. Opt. Soc. Am. B **17**(12), 2037–2042 (Dec. 2000).

[173] S. Noda, A. Chutinan, and M. Imada, "Trapping and emission of photons by a single defect in a photonic bandgap structure", Nature (London) **407**(6804), 608–610 (Oct. 2000).

[174] R. Stoffer, H. J. W. M. Hoekstra, R. M. de Ridder, E. Van Groesen, and F. P. H. Van Beckum, "Numerical studies of 2D photonic crystals: Waveguides, coupling between waveguides and filters", Opt. Quantum Electron.

32(6/8), 947–961 (Aug. 2000).

[175] E. Centeno, B. Guizal, and D. Felbacq, "Multiplexing and demultiplexing with photonic crystals", J. Opt. A: Pure Appl. Opt. **1**(5), L10–L13 (Sept. 1999).

[176] S. Fan, P. R. Villeneuve, J. D. Joannopoulos, and H. A. Haus, "Channel Drop Tunneling through Localized States", Phys. Rev. Lett. **80**(5), 960–963 (Feb. 1998).

[177] S. Fan, P. R. Villeneuve, J. D. Joannopoulos, M. J. Khan, C. Manolatou, and H. A. Haus, "Theoretical analysis of channel drop tunneling processes", Phys. Rev. B **59**(24), 15882–15892 (June 1999).

[178] A. Sharkawy, S. Shi, and D. W. Prather, "Multichannel wavelength division multiplexing with photonic crystals", Appl. Opt. (IP) **40**(14), 2247–2252 (May 2001).

[179] C. R. Simovski and S. He, "Antennas based on modified metallic photonic bandgap structures consisting of capacitively loaded wires", Microwave Opt. Technol. Lett. **31**(3), 214–221 (Nov. 2001).

[180] S. A. Magnitskii, A. V. Tarasishin, and A. M. Zheltikov, "Near-field optics with photonic crystals", Appl. Phys. B **69**(5/6), 497–500 (Nov./Dec. 1999).

[181] A. Mekis and J. D. Joannopoulos, "Tapered Couplers for Efficient Interfacing Between Dielectric and Photonic Crystal Waveguides", J. Lightwave Technol. **19**(6), 861–865 (June 2001).

[182] Y. Xu, R. K. Lee, and A. Yariv, "Adiabatic coupling between conventional dielectric waveguides and waveguides with discrete translational symmetry", Opt. Lett. **25**(10), 755–757 (May 2000).

[183] T. D. Happ, M. Kamp, and A. Forchel, "Photonic crystal tapers for ultracompact mode conversion", Opt. Lett. **26**(14), 1102–1104 (July 2001).

[184] A. Mekis, S. Fan, and J. D. Joannopoulos, "Absorbing Boundary Conditions for FDTD Simulations of Photonic Crystal Waveguides", IEEE Microwave Guided Wave Lett. **9**(12), 502–504 (Dec. 1999).

[185] M. Koshiba, Y. Tsuji, and S. Sasaki, "High-Performance Absorbing Boundary Conditions for Photonic Crystal Waveguide Simulations", IEEE Microwave Wireless Components Lett. **11**(4), 152–154 (Apr. 2001).

[186] C. Hafner, "Multiple multipole (MMP) computations of guided waves and waveguide discontinuities", Int. J. Numer. Model. **3**(?), 247–257 (1990).

[187] C. Hafner, "MMP Modeling of Discontinuities in Open Waveguides", in *4th Conference on Electromagnetic and Light Scattering by Nonspherical Particles: Theory and Applications*, edited by F. Obelleiro, J. L. Rodríguez, and T. Wriedt, pages 273–280, Universidade de Vigo, Vigo, 1999.

[188] C. Hafner, *The Multiple Multipole Program (MMP) and the Generalized Multipole Technique (GMT)*, in Ref. [19], chapter 3, pages 21–38.

[189] R. D. Meade, K. D. Brommer, A. M. Rappe, and J. D. Joannopoulos, "Electromagnetic Bloch waves at the surface of a photonic crystal", Phys. Rev. B **44**(19), 10961–10964 (Nov. 1991).

[190] F. Ramos-Mendieta and P. Halevi, "Surface electromagnetic waves in two-dimensional photonic crystals: Effect of the position of the surface plane", Phys. Rev. B **59**(23), 15112–15120 (June 1999).

[191] H. A. Haus, *Waves and fields in optoelectronics*, Prentice-Hall, Englewood Cliffs, N. J., 1984.

[192] C. Manolatou, M. J. Khan, S. Fan, P. R. Villeneuve, H. A. Haus, and J. D. Joannopoulos, "Coupling of Modes Analysis of Resonant Channel Add-Drop Filters", IEEE J. Quantum Electron. **35**(9), 1322–1331 (Sept. 1999).

[193] Y. Xu, Y. Li, R. K. Lee, and A. Yariv, "Scattering-theory analysis of waveguide-resonator coupling", Phys. Rev. E **62**(5), 7389–7404 (Nov. 2000).

[194] R. Waldhäusl, B. Schnabel, P. Dannberg, E.-B. Kley, A. Bräuer, and W. Karthe, "Efficient coupling into polymer waveguides by gratings", Appl. Opt. (LP) **36**(36), 9383–9390 (Dec. 1997).

[195] M. M. Spühler, B. J. Offrein, G.-L. Bona, R. Germann, I. Massarek, and D. Erni, "A Very Short Planar Silica Spot-Size Converter Using a Nonperiodic Segmented Waveguide", J. Lightwave Technol. **16**(9), 1680–1685 (Sept. 1998).

[196] J. Backlund, J. Bengtsson, C.-F. Carlström, and A. Larsson, "Multifunctional Grating Couplers for Bidirectional Incoupling into Planar Waveguides", IEEE Photon. Technol. Lett. **12**(3), 314–316 (Mar. 2000).

[197] K. H. Dridi and A. Bjarklev, "Optical electromagnetic vector-field modeling for the accurate analysis of finite diffractive structures of high complexity", Appl. Opt. (LP) **38**(9), 1668–1676 (Mar. 1999).

[198] M. Paulus and O. J. F. Martin, "Green's tensor technique for scattering in two-dimensional stratified media", Phys. Rev. E **63**(6), 066615/1–8 (June 2001).

[199] P. G. Dinesen, J. S. Hesthaven, J. P. Lynov, and L. Lading, "Pseudospectral method for the analysis of diffractive optical elements", J. Opt. Soc. Am. A **16**(5), 1124–1130 (May 1999).

[200] S. F. Helfert and R. Pregla, "Analysis of thin layers and discontinuities", Opt. Quantum Electron. **31**(9/10), 721–732 (Oct. 1999).

[201] D. W. Prather, M. S. Mirotznik, and J. N. Mait, "Boundary integral methods applied to the analysis of diffractive optical elements", J. Opt. Soc. Am. A **14**(1), 34–43 (Jan. 1997).

[202] P. G. Dinesen and J. S. Hesthaven, "Fast and accurate modeling of waveguide grating couplers", J. Opt. Soc. Am. A **17**(9), 1565–1572 (Sept. 2000).

[203] P.-P. Borsboom and H. J. Frankena, "Field analysis of two-dimensional focusing grating couplers", J. Opt. Soc. Am. A **12**(5), 1142–1146 (May 1995).

[204] M. Lo and P. Meyrueis, "Locally rigorous electromagnetic analysis of nonperiodic gratings with large size and small features in the non-scalar validity domain by the field stitching method", Opt. Quantum Electron.

32(6/8), 691–699 (Aug. 2000).

[205] J. Fröhlich, *Evolutionary Optimization for Computational Electromagnetics*, Diss. ETH No. 12232, Swiss Federal Institute of Technology Zurich, 1997.

[206] D. Erni, D. Wiesmann, M. Spühler, S. Hunziker, E. Moreno, B. Oswald, J. Fröhlich, and C. Hafner, "Application of Evolutionary Optimization Algorithms in Computational Optics", ACES Journal: SI on Genetic Algorithms **15**(2), 43–60 (July 2000).

[207] Y. Rahmat-Samii and E. Michielssen, *Electromagnetic Optimization by Genetic Algorithms*, John Wiley and Sons, New York, 1999.

[208] T. Bäck, *Evolutionary Algorithms in Theory and Practice: evolution strategies, evolutionary programming, genetic algorithms*, Oxford University Press, New York, 1996.

[209] M. M. Spühler and D. Erni, "Towards structural optimization of planar integrated lightwave circuits", Opt. Quantum Electron. **32**(6/8), 701–718 (Aug. 2000).

[210] M. Paulus and O. J. F. Martin, "How to tap an innocent waveguide", Opt. Express **8**(12), 644–648 (June 2001).

[211] D. Erni, M. M. Spühler, and J. Fröhlich, "Evolutionary optimization of non-periodic coupled-cavity semiconductor laser diodes", Opt. Quantum Electron. **30**(5/6), 287–303 (May 1998).

[212] M. M. Spühler, D. Erni, and J. Fröhlich, "An evolutionary optimization procedure applied to the synthesis of integrated spot-size converters", Opt. Quantum Electron. **30**(5/6), 305–321 (May 1998).

[213] Ref. [208], chapter 2.1, pages 66–91.

[214] R. E. Kunz, *Integrated Optics in Sensors: Advances Toward Miniaturized Systems for Chemical and Biochemical Sensing*, in *Integrated Optical Circuits and Components: design and applications*, edited by E. J. Murphy, chapter 10, pages 335–380, Marcel Dekker, New York, 1999.

The mountain drawings were taken from:

[215] D. Pliego, editor, *150 Excursiones Clásicas por la Sierra de Madrid*, Cuadernos del Guadarrama, Madrid, 2001.

Curriculum Vitae

I was born in 1969 in Alicante (Spain), son of María Dolores Soriano Morales and Esteban Moreno Sansón and brother of Alejandro and Susana.

After the high school years (1983-1986), I graduated in physics (specialism in theoretical physics) at the Universidad Complutense de Madrid (1987-1992), where I made some good friends with whom I had a lot of fun during our hikes on the mountains and elsewhere. During the years 1993-1994, I followed postgraduate courses in theoretical and mathematical physics at the same university. Later, I spent some years (1994-1998) teaching physics at the Physics and Mathematics Department of the Universidad Alfonso X El Sabio (Madrid). In the period 1999-2002, I have been research assistant in the Laboratory for Electromagnetic Fields and Microwave Electronics at the Swiss Federal Institute of Technology in Zurich.

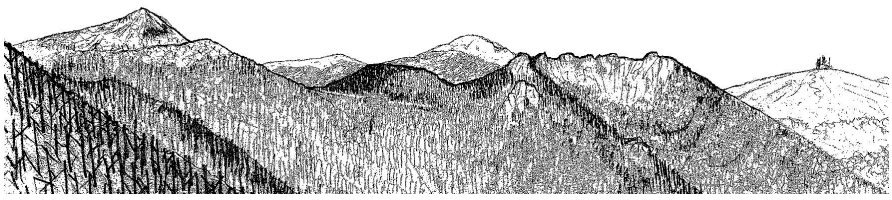

Montón de Trigo, Peñalara, Siete Picos y Bola del Mundo desde la Peñota.